

Autonomous Navigation in Libration Point Orbits

by

Keric A. Hill

B.S., Brigham Young University, 2000

M.S., University of Colorado, Boulder, 2004

A thesis submitted to the
Faculty of the Graduate School of the
University of Colorado in partial fulfillment
of the requirements for the degree of
Doctor of Philosophy
Department of Aerospace Engineering Sciences

2007

This thesis entitled:
Autonomous Navigation in Libration Point Orbits
written by Keric A. Hill
has been approved for the Department of Aerospace Engineering Sciences

George Born

Dr. Rodney Anderson

Date _____

The final copy of this thesis has been examined by the signatories, and we find that both the content and the form meet acceptable presentation standards of scholarly work in the above mentioned discipline.

Hill, Keric A. (Ph.D., Aerospace Engineering)

Autonomous Navigation in Libration Point Orbits

Thesis directed by Prof. George Born

Spacecraft in libration orbits can use scalar satellite-to-satellite tracking (SST) data, such as crosslink range, to perform autonomous orbit determination. SST between two spacecraft provides information on the size, shape, and relative orientation of two orbits. A pair of Keplerian orbits of a certain size, shape, and relative orientation can have any absolute orientation about the center of mass of the primary body. This means that SST alone is not sufficient to autonomously determine the absolute orientation of the conic orbits of spacecraft near Earth. However, in the three-body problem, the gravitational influence of the third body can indirectly provide information about the direction to that third body and with it, the absolute orientation of the orbits. In other words, a halo orbit near the Moon is influenced very strongly by both the Earth and the Moon and has a unique size and shape. Because of the strong asymmetry of the three-body force field, a halo orbit with that size and shape can only have a single orientation with respect to the Earth and Moon. This means that a spacecraft in a halo orbit can track a second spacecraft using crosslink range measurements and determine the absolute positions and velocities of both spacecraft simultaneously without any Earth-based tracking or mathematical constraints. Simulations show that this technique works well in lunar halo orbits in the Circular Restricted Three-Body Problem. More realistic simulations show similar results in the Earth-Moon system using the DE403 planetary ephemeris, solar gravity, solar radiation pressure (SRP), and the LP100K lunar gravity field in an Extended Kalman Filter. The position errors for lunar spacecraft were on the order of 10 m RSS and about 100 m RSS for halo orbiters in various locations. Range biases, spacecraft reflectance, and maneuver errors were all successfully estimated, even in the presence of SRP and gravity modeling errors. Halo stationkeeping maneuvers were performed using real-time estimates, and a combination of frequent maneuvers and precise orbit determination resulted in stationkeeping budgets of only a few m/s per year.

Dedication

The idea for this research came from Him for whom all orbits are known.

The Earth rolls upon her wings,
and the Sun giveth his light by day,
and the Moon giveth her light by night,
and the stars also give their light,
as they roll upon their wings in their glory,
in the midst of the power of God.

Doctrine and Covenants 88:45

Acknowledgements

I would like to thank Dr. George Born for his extensive help. I can't imagine having a better advisor. I am very grateful to the CCAR staff and fellow CCAR graduate students Blair Thompson, Rodney Anderson, Jeff Parker, Kathryn Hamera, and Brandon Jones for their help and assistance. Thanks also go to Martin Lo for teaching me about the three-body problem.

I would especially like to thank my wife Rebecca for her support as I went through graduate school, and for taking the trouble to listen to what must have been boring technical conversations. She offered ideas and advice for my research that were very valuable, even coming up with the name for "Liaison Navigation."

I would also like to thank anyone determined enough to read this.

This material is based upon work supported under a National Science Foundation Graduate Research Fellowship. Any opinions, findings, conclusions or recommendations expressed in this publication are those of the authors and do not necessarily reflect the views of the National Science Foundation.

Contents

Chapter

1	Libration Point Navigation and Autonomy	1
1.1	The History of Libration Point Navigation	1
1.2	Autonomy	4
1.2.1	Individual Autonomy	5
1.2.2	Constellation Autonomy	8
2	Linked, Autonomous, Interplanetary Satellite Orbit Navigation	11
2.1	Unique Trajectories	12
2.2	Symmetry in Acceleration Functions	13
2.2.1	Example 1. Two-body Problem.	13
2.2.2	Example 2: Two-body Problem with J_2	18
2.2.3	Example 3: Three-body Earth-Moon System.	19
2.2.4	Example 4: Two-body problem with Solar Radiation Pressure	20
2.2.5	Example 5: Non-uniform Central Body Gravity.	21
2.3	Strength of the Asymmetry	22
2.4	Summary	26
3	The Circular Restricted Three-body Problem	28
3.1	Lissajous orbits	31
3.2	Halo orbits	31

4	Liaison Navigation in Lunar Halo Orbits	35
4.1	Liaison Navigation Methods	35
4.2	Liaison Navigation Orbit Geometry	40
4.3	Liaison Navigation Test Methods	41
4.4	Constellation Geometry Comparisons	46
4.5	Orbit Determination Parameter Comparisons	52
4.6	Monte Carlo Analysis of the Covariance	55
5	Observability and Geometry	58
5.1	Observability	58
5.2	Observation Effectiveness	59
6	Liaison Navigation for Other Three-body Systems	67
6.1	Sun-Earth Halo Orbits	67
6.2	Sun-Earth Liaison Navigation Methods	67
6.3	Liaison Navigation Analysis of the Genesis Mission	69
6.4	Three Spacecraft Constellations in Sun-Earth Halo Orbits	71
6.5	Sun-Mars Halo Orbits	72
6.6	Conclusions for Sun-Earth and Sun-Mars Halo Orbits	75
6.7	Other Three-body Systems	76
7	Four- and n-body Models and Simulations	77
7.1	Bicircular Model	77
7.2	Multiple Shooting Differential Corrector	81
7.2.1	Level 1	82
7.2.2	Level 2	82
7.2.3	Implementation of Multiple Shooting	83
7.2.4	Ephemerides for Orbit Determination	83

7.3	Test Methods	84
7.3.1	Bicircular	85
7.3.2	Inclined Bicircular	86
7.3.3	Solar Radiation Pressure	86
7.4	Four-body Test Results	87
7.4.1	Bicircular	87
7.4.2	Inclined Bicircular	87
7.4.3	Solar Radiation Pressure	88
7.4.4	Final Four-Body Simulation	89
7.5	JPL DE405 Ephemeris	90
7.6	Conclusions from the n-body Simulations	91
8	Liaison Navigation with Maneuvers and Gravity Fields	93
8.1	Lunar Gravity Field	93
8.2	Impulsive Maneuvers	99
8.3	Simulation Results	100
8.4	Conclusion	104
9	A Lunar Navigation and Communication Mission	106
9.1	Mission Concept	107
9.1.1	Ballistic Lunar Transfers	108
9.2	LL ₂ Halo Orbit Selection (Snoopy)	109
9.2.1	Requirement 1	110
9.2.2	Requirements 2 and 3	110
9.2.3	Requirement 4	112
9.2.4	Requirement 5	113
9.2.5	Requirement 6	115
9.2.6	Requirement 7	115

9.2.7	Selected Halo Orbit	116
9.3	Low Lunar Orbit Selection (Woodstock)	121
9.4	Spacecraft Design	122
9.5	Liaison Navigation performance	124
9.6	Navigation Support	130
9.7	Conclusion	133
10	Other Lunar Navigation Simulations	135
10.1	NASA's Lunar Communications	135
10.2	TurboProp	137
10.3	Frozen Orbit Constellation	138
10.4	Hybrid L_2 /Frozen Orbit Constellation	141
10.5	L_1 /LEO Constellation	141
11	Summary and Conclusions	145
11.1	Summary of Contributions	145
11.2	Conclusions	146
11.3	Future Work	147
	Bibliography	148
	Appendix	
A	Converting from the CRTBP to ICRF	153

Tables

Table

1.1	DESIRED RESULTS OF SPACECRAFT AUTONOMY	4
1.2	PROPOSED MEASUREMENTS FOR INDIVIDUAL AUTONOMOUS ORBIT DETERMINATION	9
3.1	ABBREVIATIONS FOR LAGRANGE POINTS IN VARIOUS THREE-BODY SYSTEMS.	30
4.1	PARAMETERS OF THE LUNAR- AND EARTH-CENTERED TEST ORBITS.	43
4.2	DESCRIPTION OF BASELINE ORBITS.	53
6.1	APPROXIMATE SPEED OF CONVERGENCE FOR LIAISON NAVIGATION WITH VARIOUS CONSTELLATION TYPES.	71
6.2	THREE-BODY SYSTEMS USED FOR LIAISON NAVIGATION SIMULATIONS IN THE CRTBP.	76
7.1	COMPARISON OF ORBIT DETERMINATION ACCURACY FOR BICIRCULAR AND CRTBP HALO ORBITS.	88
7.2	COMPARISON OF ORBIT DETERMINATION ACCURACY FOR DIFFERENT INCLINATIONS OF THE MOON'S ORBIT PLANE.	88
7.3	COMPARING ORBIT DETERMINATION ACCURACY FOR VARIOUS FORCE MODELS.	91

8.1	AVERAGED SIMULATION RESULTS FOR THE LIAISON NAVIGATION STA- TIONKEEPING STUDY.	103
9.1	STATIONKEEPING BUDGETS FOR BOTH SPACECRAFT IN TERMS OF ΔV	124
9.2	ORBIT DETERMINATION ACCURACY USING SNOOPY AND WOODSTOCK AS TRACKING STATIONS	133
10.1	ORBITAL ELEMENTS FOR A THREE-SATELLITE LUNAR COMMUNICA- TIONS CONSTELLATION IN FROZEN ORBITS.	138

Figures

Figure

2.1	The vector field of accelerations in the x-y plane in Example 1 with two-body gravity.	14
2.2	Spherical triangle representing the relative orientation of two orbits projected onto a sphere.	15
2.3	The vector field of accelerations in the x-z plane for Example 2 with exaggerated J_2	19
2.4	The vector field of accelerations in the x-z plane for Example 3 with the Earth and the Moon.	21
2.5	Map of α for acceleration due to SRP in the Earth-Moon system.	24
2.6	Map of α for acceleration due to \mathbf{J}_2 in the Earth system.	24
2.7	Map of α for acceleration due to the third body in the Earth-Moon system. . . .	25
2.8	Map of α near the Moon for acceleration due to the third body in the Earth-Moon system. The positions of the lunar L_1 and L_2 Lagrange points are shown along with a halo orbit around each.	25
3.1	Diagram of the Circular Restricted Three-Body Problem with a rotating, non-dimensional coordinate frame.	29
3.2	Schematic location of the five Lagrange points in the CRTBP.	29
3.3	Third-order Lissajous trajectory in the Sun-Earth three-body problem with y and z amplitudes of 200,000 km. Figure 1 from Howell and Pernicka (1988)	32

3.4	L_1 and L_2 halo orbits in the Earth-Moon system in the rotating frame.	33
3.5	Positions of various values of the phase angle, τ , on a halo orbit in the Earth-Moon system projected onto the x-y plane.	34
4.1	Initial conditions and names of LL_1 test orbits.	42
4.2	Initial conditions and names of LL_2 test orbits.	42
4.3	Initial conditions and names of LL_3 test orbits.	43
4.4	Plot of covariance in time showing convergence using the Kalman Filter for a LL_1B Halo ₂ constellation with $\Delta\tau = 90^\circ$	44
4.5	Navigation accuracy for two spacecraft on a halo orbit with varying separation in phase angle τ	45
4.6	β_{con} separated into x, y, and z components for LL_1 Halo ₂ constellations.	47
4.7	Plot of β_{con} (m) for Halo ₂ and Halo-Halo constellations at LL_1	48
4.8	Plot of β_{con} (m) for Halo ₂ and Halo-Halo constellations at LL_2	49
4.9	Plot of β_{con} (m) for Halo ₂ and Halo-Halo constellations at LL_3	49
4.10	Plot of β_{con} (m) for Halo-Halo constellations with one spacecraft at LL_1 and one at LL_2	50
4.11	Plot of β_{con} (m) for Halo-Earth and Halo-Moon constellations at LL_1	50
4.12	Plot of β_{con} (m) for Halo-Earth and Halo-Moon constellations at LL_2	51
4.13	Plot of β_{con} (m) for Halo-Earth and Halo-Moon constellations at LL_3	51
5.1	Observation effectiveness for a Lb-Le Moon-Moon constellation.	60
5.2	Observation effectiveness for a LL_1B Halo ₂ constellation.	60
5.3	Components of observation effectiveness for Spacecraft 1 in the Lb-Le Moon-Moon constellation.	61
5.4	Components of observation effectiveness for Spacecraft 1 in the LL_1B Halo ₂ constellation.	62
5.5	Position error ellipsoid aspect ratios for a halo orbit and a Keplerian orbit. . . .	64

5.6	Relationship between the shape of the uncertainty ellipsoid and the effectiveness of an observation vector.	65
5.7	Relationship between the sensing direction-local unstable manifold angle and the observation effectiveness.	66
6.1	Initial conditions and names of Sun-Earth L_1 test orbits.	68
6.2	Initial conditions and names of Sun-Earth L_2 test orbits.	68
6.3	Initial conditions and names of Sun-Mars L_1 test orbits.	73
6.4	Initial conditions and names of Sun-Mars L_2 test orbits.	73
7.1	Geometry of the Inertial Bicircular Model.	78
7.2	Geometry of the inclined Inertial Bicircular Model.	79
7.3	Halo orbits computed in the CRTBP and the Bicircular model using LL1B with $\tau = 0$ and $MB(t_0) = 0$ and projected into the x-y plane.	84
8.1	The equatorial system in which the Libration Euler angles are defined. (The value of ϕ would be negative as shown.) Credit: Newhall and Williams (1997).	96
8.2	Simulation orbit and maneuver timeline.	102
8.3	Orbit determination accuracy from the LL1C-Moon ΔV study when using a Lunar gravity field.	105
9.1	Number of days a halo orbiter is visible above 10° elevation at $80^\circ S$ $0^\circ E$	111
9.2	Orbit Determination and Stationkeeping simulation results.	112
9.3	Gaps in tracking as a percentage of the time when Woodstock is not visible from Earth or Snoopy.	114
9.4	Tracking gaps as a percentage of the time neither of two halo orbiters is visible at the worst case surface locations.	114
9.5	Gaps in tracking as a percentage of the time when Woodstock is not visible from Earth or two halo orbiters.	115

9.6	Plot used to select the halo orbit for Snoopy. The numbers in the legend correspond to the orbit selection requirement number. The legend also shows the vertical axis units for each metric. The chosen orbit has a Jacobi constant of about 3.06.	117
9.7	Elevation of two halo orbiters (Elev1, Elev2) and the Earth at the lunar south pole. The spacecraft are in the orbit selected for Snoopy, 180° apart. Orbits were propagated using the full ephemeris and SRP.	118
9.8	Skyplot of two halo orbiters at the lunar south pole. The spacecraft are in the orbit selected for Snoopy, 180° apart. Orbits were propagated using the full ephemeris and SRP.	118
9.9	Earth/Snoopy-Woodstock tracking gaps (% of points).	119
9.10	Earth/Snoopy-Woodstock tracking coverage density (% points/% area) at the optimum value of $\delta = 220^\circ$	119
9.11	Earth/Snoopy-Woodstock tracking coverage density (% points/% area) at the worst case value of $\delta = 60^\circ$	120
9.12	Daily schedule of comm/nav support for Snoopy and Woodstock	129
9.13	Snoopy position accuracy using the EKF.	130
9.14	Snoopy velocity accuracy using the EKF.	131
9.15	Woodstock position accuracy using the EKF.	131
9.16	Woodstock velocity accuracy using the EKF.	132
10.1	Satellite 1 position accuracy using the EKF. The three satellites are in coplanar frozen orbits.	140
10.2	Satellite 1 position accuracy using the EKF. The three satellites are in frozen orbits in three different orbit planes.	140
10.3	L_2 halo orbiter EKF position accuracy using crosslink range measurements to a lunar spacecraft in a frozen orbit.	142

10.4 Lunar Pole-lingering frozen orbit EKF position accuracy using crosslink range
measurements to a halo orbiter at L₂. 143

10.5 L₁ halo orbiter EKF position accuracy using crosslink range measurements to a
spacecraft in LEO. 144

Chapter 1

Libration Point Navigation and Autonomy

Recent missions to libration points have been very useful and successful, but have not taken advantage of all the possibilities that await. The dynamics of libration point orbits offer many opportunities for flexible, low-energy trajectories. However, due to the unstable nature of most of these orbits, the stationkeeping that is required will demand frequent maneuvers and precise orbit determination. Section 1.1 will examine the navigation of the libration point missions that have flown and how autonomous navigation could benefit future missions. Section 1.2 will present a review of autonomous orbit determination techniques that have been implemented or proposed. Details on libration points and libration point orbits will be given in Chapter 3.

1.1 The History of Libration Point Navigation

Currently, there are six spacecraft that have traveled to libration points, all of which were Sun-Earth libration points. Only one has remained at the Sun-Earth L_2 point (EL_2), while the other five went to the Sun-Earth L_1 point (EL_1). Dunham and Farquhar (2002) give summaries of the missions and Beckman (2002) explains how the orbit determination was performed.

International Sun-Earth Explorer 3 (ISEE-3) was the first libration point mission. Its purpose was to observe the solar wind before it reached the vicinity of the Earth. ISEE-3 was launched on August 12, 1978 and arrived at its EL_1 quasi-halo orbit on November 20. It stayed there for four years and collected data, proving for the first time that a libration point mission was possible. At the libration point, ISEE-3 was tracked using S-band radiometric data on an

irregular basis. A batch processor was used for the orbit determination every 14 days using a fit span of 21 days, which gave a 7-day overlap. Stationkeeping maneuvers were performed every 45 days, with a halo orbit period of about six months. From overlap comparisons and covariance analysis, the accuracy of the orbit determination was about 6 km. ISEE-3 also demonstrated how a spacecraft at a libration point can “fall off” in a directed manner and arrive at another location with only a minimal change in velocity, or ΔV . ISEE-3 left the libration point, was renamed International Cometary Explorer (ICE), performed lunar flybys, and went on to encounter the comet Giacobini-Zimmer on September 11, 1985.

The Solar Heliospheric Observatory (SOHO) was the second libration point mission. It also went to EL_1 , this time to observe the Sun. It launched on 2 December 1995 and arrived on its halo orbit on 14 February 1996. Although SOHO experienced several catastrophes, flight controllers were able to regain control and SOHO is still flying and providing valuable information on solar phenomena. SOHO used a quasi-halo orbit very similar to ISEE-3 and is mainly tracked with the 26 meter Deep Space Network (DSN) antennas, with some 34 m and 70 m data as well. SOHO is usually tracked 5 hours a day, although the schedule varies to accommodate other DSN users. Similar to ISEE-3, it was found that a 21-day fit span would work well for SOHO. Stationkeeping maneuvers are performed every 8-12 weeks, and the maneuvers are not estimated. Instead, a new fit is started at the time of the maneuver, which means that some fits are shorter than 21 days. From overlaps, the orbit determination accuracy for SOHO is around 7 km.

The third libration point mission was the Advanced Composition Explorer (ACE), which also went to EL_1 to analyze solar wind and other particles. ACE launched on 25 August 1997 and reached its orbit on December 13. The science orbit for ACE was a Lissajous orbit smaller than the ISEE-3 or SOHO trajectories, and was the first Lissajous orbit flown (see Chapter 3 for information on Lissajous orbits). Because this Lissajous orbit would normally take ACE in front of the Sun when viewed from the Earth, stationkeeping maneuvers had to be performed periodically to keep this from happening and maintain constant contact with the Earth. Because

a new fit had to be started after each stationkeeping maneuver, the fit spans were between 4 and 14 days long. Three hours of 26 m DSN tracking data are acquired every day, with some additional tracking from the 34 m antennas. Although there are no overlap comparisons due to the short fit spans, the orbit determination error was estimated to be about 10 km.

WIND also qualified as the fourth libration point mission because it passed around EL_1 several times during the course of the mission. It repeatedly performs lunar swingbys to measure the bow shock region of the Earth's magnetic field.

ISEE-3 did pass by EL_2 , but the first mission designed to remain at EL_2 was the Microwave Anisotropy Probe (MAP). This spacecraft was designed to measure microwave background radiation while keeping the Earth between itself and the Sun. MAP launched on 30 June 2001 and arrived at EL_2 on October 1. MAP is tracked for at least 45 minutes every day from the 34 m or 70 m DSN antennas, which give much better observation data than for the previous libration point missions. Also, MAP has a nearly constant cross sectional area facing the Sun, which makes the modeling of solar radiation pressure more accurate. The fit spans used for orbit determination vary from 14 to 72 days, depending on the time between maneuvers. It is estimated from an overlap comparison that the orbit determination accuracy is as good as 2 km.

The Genesis spacecraft went to both EL_1 and EL_2 during the course of its mission, although it performed its science mission only at EL_1 . The probe was designed to capture solar wind particles for Earth return. It launched on 8 August 2001 and arrived at EL_1 on November 16 (Wawrzyniak et al., 2005) into an orbit similar to ISEE-3 and SOHO. After two years, and by using only a very small maneuver, Genesis left EL_1 on 1 April 2004 and traveled to EL_2 . By passing near EL_2 , it was able to return to the Earth with just the right approach geometry so that a sample return capsule could be recovered in Utah.

Dunham and Farquhar (2002) list eight future libration point missions being considered when their paper was written. If these missions fly, they will probably join an increasing number of spacecraft that need DSN tracking. Beckman (2002) suggests that an autonomous navigation

system for libration point orbits could eliminate the need for DSN contacts dedicated only to tracking. The rest of this dissertation will be dedicated to investigating that idea further.

1.2 Autonomy

As spacecraft become more autonomous, they are less dependent upon instructions and input from Earth. In general, spacecraft autonomy is only desirable if it leads to decreased cost or increased performance or reliability. These three attributes are emphasized in Table 1.1. Spacecraft autonomy can lead to decreased cost if ground control operations or hardware are reduced or eliminated. Autonomy can lead to increased performance if the spacecraft can do something better or faster than when relying on ground-based inputs, or if the spacecraft itself can be made simpler or less massive. One must be very careful that autonomy does not lead to decreased reliability by making sure there is a sufficient amount of fault detection and correction in the control algorithm. While various types of autonomy don't necessarily include all three, these attributes can be used as criteria to evaluate the benefit of any autonomous control methods.

Table 1.1: DESIRED RESULTS OF SPACECRAFT AUTONOMY

Decreased cost
Increased performance
Increased reliability

Spacecraft are dependent on ground control for many functions, but one of the largest dependencies that spacecraft have in terms of hardware and manpower is that of navigation. Navigation is generally considered to consist of two parts: estimating the current course, and course correction. For spacecraft, estimating the current course is done using orbit determination, and course correction is performed using maneuvers. While the focus of this research is on orbit determination, the autonomous computation and execution of trajectory correction maneuvers will be touched upon as well.

Orbit determination is considered autonomous when it is performed onboard an orbiting spacecraft in real time without ground support (Chory et al., 1986). Although in some cases it was desired that the autonomous spacecraft be nonradiating, that is not considered essential here. Due to these requirements, measurements used in estimating an orbit autonomously must be obtained using only hardware on the spacecraft.

Autonomous orbit determination techniques can be divided into two broad classes: “Individual Autonomy,” and “Constellation Autonomy.” Individual autonomy means that a single spacecraft has all of the necessary hardware to take measurements and estimate its own orbit state. Constellation autonomy means that multiple spacecraft track each other in some way and use the relative measurements to obtain estimates of the orbit states for the whole constellation simultaneously.

A spacecraft can obtain measurements not strictly independent of ground support. This type of navigation will be referred to as “semiautonomous,” which means that the measurements are obtained onboard the spacecraft and the orbit determination is self-contained, but dependent on Earth-based operations either directly or indirectly. This would include measurements obtained using DORIS, a ground-based broadcasting network, and GPS signals, which indirectly depend upon ground support in the form of the GPS ground segment that maintains the GPS constellation. Strictly autonomous orbit determination does not mean the spacecraft has to be completely free of any Earth-based monitoring or communication, but that no ground support is used in performing the orbit determination.

1.2.1 Individual Autonomy

Individual autonomy, when compared to constellation autonomy, has the obvious advantage that only one spacecraft is required. This means that the costs associated with designing, building, and integrating multiple spacecraft are avoided. Plus, it is usually harder to coordinate the launch of multiple spacecraft, and there is the added possibility that the loss of one spacecraft could disable the whole constellation.

The type of measurements used for orbit determination can be angles measurements or scalar measurements. Angles measurements used for individual autonomous orbit determination generally provide the direction from the spacecraft to some celestial object. Scalar measurements used for individual autonomous orbit determination generally give the distance or speed of the spacecraft with respect to an object in space.

The Air Force conducted research into several types of individual autonomy starting as early as 1963 (Chory et al., 1986). These studies investigated the use of several different sensor types. The horizon scanner was designed to sense the Earth's limb or horizon. This could be used to obtain the angles to the center of the Earth. However, sensing the exact location of the Earth's horizon is difficult, so an improvement on this method was to measure the refraction of stars seen through the Earth's atmosphere. The amount of refraction was used to estimate the altitude of the star above the horizon.

Landmark tracking is where a sensor on the spacecraft tracks the angles to a landmark on the Earth. Different methods were proposed for both known and unknown landmarks. The space sextant was an instrument whose purpose was to provide scalar measurements using the lunar limb as a reference. Many different combinations of these measurements were considered as well, including Earth, Sun, and star tracking. The accuracy for these methods was as good as 1 km (Hicks and Wiesel, 1992).

Other autonomous orbit determination techniques have been proposed using sensors that observe the orientation of the Earth's magnetic field. This can eliminate the need for extra sensors if a magnetometer is needed on the spacecraft for other reasons. The addition of star tracker or Sun sensor data from sensors already needed for the attitude determination system increase the accuracy. The best accuracy for these techniques was on the order of several kilometers (Psiaki, 1998, 1999a, 2002).

XNAV, or X-ray pulsar navigation, is an emerging concept for using x-ray pulsars with a known, fixed frequency as navigation signals (Sheikh et al., 2006). By tracking several pulsars, the measurements could be used to determine position and time. With current technology, the

position estimates with respect to the solar system barycenter should have an error of about 1 km.

A measurement type which can be used for semiautonomous orbit determination is forward link Doppler. Researchers at NASA's Goddard Space Flight Center showed that semiautonomous orbit determination could be performed in a high Earth orbit (HEO) using Earth sensors, Sun sensors, and forward link Doppler measurements (Long et al., 2000). The predicted accuracy was estimated to be 1.5 km.

The French DORIS system consists of 50 ground stations distributed evenly across the Earth. These stations transmit dual-frequency signals to be used for spacecraft navigation. The DORIS Immediate Orbit DEtermination (DIODE) software was developed to use the DORIS signals for semiautonomous navigation. DIODE has achieved accuracy on the order of a few meters for spacecraft such as Topex/Poseidon, Spot-2, Spot-3, and Spot-4. It is estimated that software upgrades to DIODE could result in accuracy on the order of 10 cm (Jayles and Costes, 2004).

Another system that can provide semiautonomous navigation support is the Global Positioning System (GPS). For satellites in low Earth orbit (LEO), GPS probably offers the cheapest and most precise measurements for semiautonomous navigation. The University of Surrey used a GPS receiver intermittently on its microsatellite PoSAT-1 to demonstrate semiautonomous navigation (Unwin and Sweeting, 1995). The German microsatellite BIRD also used a GPS receiver for semiautonomous navigation and achieved an accuracy of 5 m (Gill et al., 2000; Bri   et al., 2005). It was shown that GPS signals could even be used by spacecraft in HEO which are higher than the GPS constellation. This is possible because the spacecraft can detect GPS signals originating from around the Earth's limb on the far side of the planet. Simulation results of the determination of a geostationary orbit (GEO) gave accuracies around 15 m (Moreau et al., 2000). The EO-1 spacecraft also had a GPS receiver which enabled it to not only perform orbit determination semiautonomously, but compute formation keeping maneuvers so that it maintained an optimal separation with Landsat-7 (Folta and Hawkins, 2002).

On interplanetary trajectories, GPS signals become too weak to be practical. One fully autonomous method proposed using a Sun sensor, Earth sensor, and a Doppler measurement of the speed of the spacecraft with respect to the Sun. This resulted in an accuracy better than 3 km for a heliocentric orbit similar to the Earth's (Yim et al., 2000). The Deep Space 1 spacecraft used an optical sensor and tracked small bodies such as asteroids to perform autonomous orbit determination. The autonomous optical navigation provided an interplanetary cruise position accuracy on the order of a few thousand kilometers. In operation, the navigation system successfully guided the spacecraft to an encounter at the asteroid Braille, although problems with the optical sensor and a star tracker meant that the desired navigation accuracies could not be realized (Bhaskaran et al., 2000). An analysis of several different orbit determination methods showed that autonomous optical navigation for interplanetary cruise could result in accuracies on the order of 10,000 km (Vasile, 2002). A simulation of autonomous optical navigation for spacecraft in orbit about small solar system objects showed that accuracy on the order of a few kilometers was possible (Bhaskaran et al., 1995). The Deep Impact mission actually implemented an autonomous optical navigation technique for both the impactor and the flyby spacecraft. The impactor successfully used images of comet Tempel-1 to guide itself in the approach to impact (Kubitschek, 2003).

Table 1.2 shows a summary of the different observation types that can be used for individual autonomous orbit determination.

1.2.2 Constellation Autonomy

Since constellations have added cost and complexity when compared to individual spacecraft, there must be a compensating increase in performance or reliability in the methods used to provide constellation autonomy. Measurements used in constellation autonomy include all the observations usable for single spacecraft, plus relative observations between the other constellation spacecraft. Relative measurements could include angles to other spacecraft obtained using optical tracking, or scalar Satellite-to-Satellite Tracking (SST) measurements like crosslink

Table 1.2: PROPOSED MEASUREMENTS FOR INDIVIDUAL AUTONOMOUS ORBIT DETERMINATION

Degree of Autonomy	Sensor	Measurement
Autonomous	Horizon Scanner	angles to Earth
Autonomous	Stellar Refraction	angles to Earth
Autonomous	Landmark Tracker	angles to known/unknown landmark
Autonomous	Space Sextant	scalar to Moon
Autonomous	Sun Sensor	angles to Sun
Autonomous	Sun Doppler	scalar to Sun
Autonomous	Star Tracker	angles to star
Autonomous	Magnetometer	angles along magnetic field
Autonomous	Optical Navigation	angles to any object
Autonomous	X-ray Pulsar Navigation	scalar to pulsar
Semiautonomous	Forward Link Doppler	scalar to ground station
Semiautonomous	DIODE	scalar to ground network
Semiautonomous	GPS Receiver	spacecraft position

range or Doppler. One advantage to these relative scalar measurements is that it is generally easier to get precise and useful scalar measurements between two cooperating spacecraft than between the spacecraft and the irregular surface of a celestial body. In other words, satellite-to-satellite range measurements can be very accurately modeled since the specifications of the two spacecraft are well known, but the usefulness of radar altimetry in orbit determination is only as good as the topographical maps of the targeted celestial body.

Markley (1984) proposed using constellation crosslinks to enhance autonomous navigation using Earth and Sun sensors. His study included both crosslink range and angles and showed that the crosslink measurements significantly improved the orbit accuracy. Crosslink measurements were proposed as a method of autonomously navigating the GPS constellation, but the autonomous navigation would be accurate for a limited time (Menn, 1986). It was also found that the relative position vector between two satellites could be used for very accurate autonomous orbit determination (Psiaki, 1999b). In this method, the satellites generated crosslink range measurements as well as angles from one spacecraft to another using something like an optical tracking sensor and star trackers. These measurements can be combined to create a vector between the spacecraft. Another study by Yim et al. (2004) concluded that autonomous

orbit determination could be performed without crosslink range measurements, using only the optical trackers to obtain vector or angles measurements. However, accuracy estimates showed that crosslink range and angles measurements combined resulted in accuracies of a few meters, while results for the angles only method were a few hundred meters. This shows that the scalar crosslink range measurements can be much stronger than angles, as long as observability issues are resolved. Chapter 2 will discuss the use of scalar SST data without the angles data.

Chapter 2

Linked, Autonomous, Interplanetary Satellite Orbit Navigation

This chapter will discuss whether autonomous navigation can be performed using only scalar Satellite-to-Satellite Tracking (SST) data, such as crosslink range or Doppler. The goal is to estimate the complete satellite state vector without any supplemental ground tracking. SST only provides information on the relative motion of two or more spacecraft and is normally used in conjunction with Earth-based tracking in order to obtain information on the absolute position. For example, one spacecraft is tracked from the ground, and it tracks a second satellite. Combining the observations, one can successfully estimate the orbits of both satellites. This method is currently used to determine the orbits of spacecraft in LEO with the Tracking and Data Relay Satellite System (TDRSS). It has not been proposed to use SST alone to estimate the absolute positions of spacecraft, except for limited periods (Menn, 1986). That is because in the two-body problem, SST only provides information on the size, shape, relative orientation of the orbits, and the spacecraft positions along the orbits.

Suppose an orbit exists with a unique size, shape, and absolute orientation. SST observations could be used to correctly determine the size and shape of the orbit. Since there is only one possible orientation for that orbit, the absolute orientation of that orbit can also be determined. SST also provides information on the relative orientation of the trajectories of the other spacecraft involved, so the absolute positions of all the other participating spacecraft would be known as well. This is the basis for a new method of orbit determination called Linked, Autonomous, Interplanetary Satellite Orbit Navigation (LiAISON), hereafter referred

to as “Liaison Navigation” (Hill et al., 2005b; Hill and Born, 2007). Liaison Navigation means using SST observations to determine the orbits of two or more spacecraft when at least one of them is in an orbit with a unique size and shape.

2.1 Unique Trajectories

A trajectory is unique when there is only one set of initial conditions that will result in a trajectory of that size and shape. To define what is meant by trajectories having the same size and shape, suppose that in an inertial frame, there are two spacecraft trajectories which will be called X_1 and X_2 . The orbit state of X_i at time t would be:

$$X_i(t) = \begin{bmatrix} x_i(t) & y_i(t) & z_i(t) & \dot{x}_i(t) & \dot{y}_i(t) & \dot{z}_i(t) \end{bmatrix}. \quad (2.1)$$

The two trajectories have the same size and shape if a constant 3×3 rotation, θ , and a constant 3×1 translation, Δr , can be found such that

$$X_2(t) = \begin{bmatrix} \theta & [\emptyset]_{3 \times 3} \\ [\emptyset]_{3 \times 3} & \theta \end{bmatrix} X_1(t) + \begin{bmatrix} \Delta r \\ [\emptyset]_{3 \times 1} \end{bmatrix} \quad (2.2)$$

for all times t . For a trajectory with a unique size and shape, a rotation and translation does not exist which will make it equivalent to any other trajectory. To understand the circumstances under which a unique trajectory can exist, assume that the accelerations experienced by a spacecraft depend solely on its position and time. The equations of motion for the spacecraft in an inertial frame can be written

$$\ddot{\mathbf{r}} = \mathbf{f}(\mathbf{r}, t), \quad (2.3)$$

where $\mathbf{r} = [x \ y \ z]^T$ is the position vector of the spacecraft. The characteristics of the acceleration function $\mathbf{f}(\mathbf{r}, t)$ determine whether a unique trajectory exists. A unique trajectory cannot exist if $\mathbf{f}(\mathbf{r}, t)$ and its time derivative are symmetric. The following examples illustrate several acceleration functions and their symmetry.

2.2 Symmetry in Acceleration Functions

The characteristics of the acceleration function $\mathbf{f}(\mathbf{r}, t)$ determine whether a unique trajectory exists, and also the degree to which the absolute position of the spacecraft can be estimated using SST. A unique trajectory can exist if $\mathbf{f}(\mathbf{r}, t)$ or its time derivative have the proper asymmetry. To illustrate these concepts, the following examples investigate the symmetry in $\mathbf{f}(\mathbf{r}, t)$ for different models.

2.2.1 Example 1. Two-body Problem.

In this first example, the system consists of only the Earth, represented by a point mass, and nearby space. The origin is at the center of the Earth with the x and y axes in the equatorial plane. Suppose a spacecraft of infinitesimal mass is nearby. A vector field of the resulting acceleration function $\mathbf{f}(\mathbf{r}, t)$ is plotted in Figure 2.1. Vectors are not plotted in the region that lies beneath the Earth's surface. The function $\mathbf{f}(\mathbf{r}, t)$ is symmetric about the center of the Earth.

In this model, suppose a spacecraft is in orbit around the Earth and follows a trajectory of a certain size and shape. The initial position of the spacecraft is $\mathbf{r}_0 = [x_0 \ y_0 \ z_0]^T$. Due to the symmetry in the acceleration function, there can be an infinite number of orbits of the same size and shape. The initial positions of these similar orbits all lie on a sphere centered on the Earth with radius $\|\mathbf{r}_0\|$. If there were two spacecraft in orbit, SST observations could be taken between the two spacecraft, and these observations could be used to estimate the size, shape, and relative orientation of the two orbits. However, the absolute orientation of the trajectories could not be estimated. Any rotation about the center of Earth could be applied to both trajectories to generate a new pair of orbits that could exist using the same acceleration function. They would have the same shape, size, and relative orientation and would result in exactly the same SST observations. The three state parameters required to describe the absolute orientation of the two orbits cannot be estimated from the SST observations alone. Thus, out

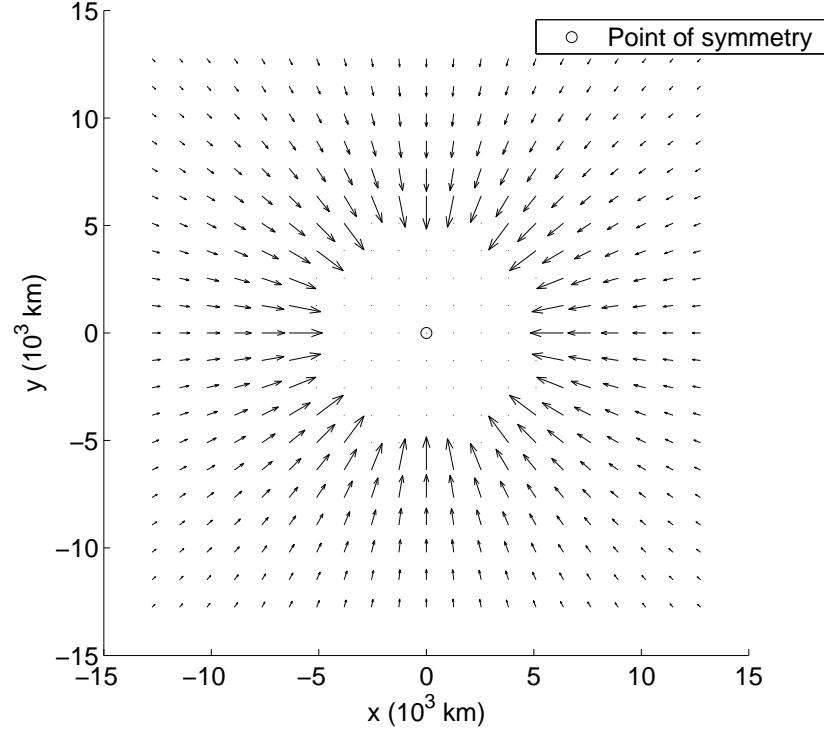


Figure 2.1: The vector field of accelerations in the x-y plane in Example 1 with two-body gravity.

of a total of twelve state parameters required to describe the absolute positions and velocities of the two spacecraft, as will be shown later, only nine can be estimated with SST.

Liu and Liu (2001) showed in a simulation that it is possible, with some exceptions, to estimate the semimajor axis, eccentricity, and true anomaly

$$\{ a_1, a_2, e_1, e_2, \nu_1, \nu_2 \}$$

of two satellites in the two-body problem using only SST between them (subscripts indicate the satellite number). These are the Keplerian orbital elements related to the size and shape of the orbits, and the position of the spacecraft along the orbits. However, difficulties arise when attempting to estimate the Keplerian elements that are related to orientation such as the inclination, the longitude of the ascending node, and the argument of perigee.

$$\{ i_1, i_2, \Omega_1, \Omega_2, \omega_1, \omega_2 \}$$

They concluded that this difficulty could be avoided by fixing the longitude of the ascending

node and the inclination for both satellites and only estimating the argument of perigee. Fixing these four state parameters resulted in an observable state in the orbit determination problem. However, if our preceding analysis is correct, it should be possible to estimate three orientation parameters instead of just two. Defining a set of these three relative orientation parameters is facilitated by projecting both orbits onto the surface of a sphere. The orbits now appear as two great circles on the sphere with two intersections. Figure 2.2 is a spherical triangle showing how the relative orientation of the periapses of the two orbits can be described with three state parameters called d , c_1 , and c_2 . d is the angle between the two orbit planes where they intersect. c_1 describes the angular distance along the first orbit from the periapsis to one of the two intersections of the orbits. This angle is positive in the direction of orbital motion. Likewise, c_2 describes the angular distance along the second orbit from the periapsis to the same intersection of the orbits. The Keplerian orientation elements can be varied with the constraint that d , c_1 , and c_2 remain constant without creating any change in the SST observations.

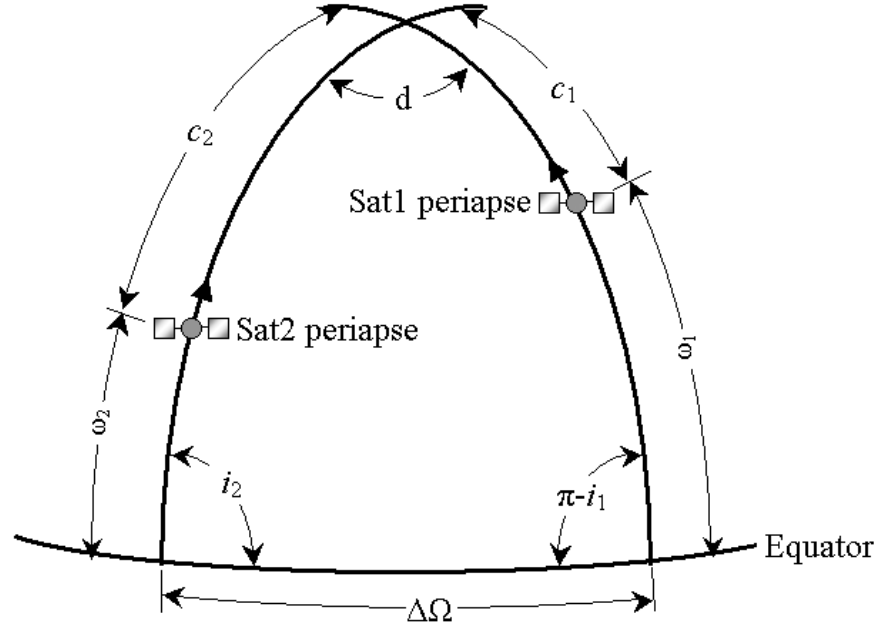


Figure 2.2: Spherical triangle representing the relative orientation of two orbits projected onto a sphere.

Figure 2.2 also shows how the parameters d , c_1 , and c_2 can be described in terms of Keplerian elements. This is done using spherical trigonometry, and the equations for all three relative orientation parameters in terms of the Keplerian orientation parameters are

$$d = \cos^{-1} [\cos(i_1) \cos(i_2) + \sin(i_1) \sin(i_2) \cos(\Delta\Omega)], \quad (2.4)$$

$$c_1 = \tan^{-1} \left[\frac{\sin(\Delta\Omega)}{\sin(i_1) \cot(i_2) - \cos(i_1) \cos(\Delta\Omega)} \right] - \omega_1, \quad (2.5)$$

$$\text{and } c_2 = \tan^{-1} \left[\frac{\sin(\Delta\Omega)}{-\sin(i_2) \cot(i_1) + \cos(i_2) \cos(\Delta\Omega)} \right] - \omega_2. \quad (2.6)$$

Because d , c_1 , and c_2 represent the relative orientation, it should be possible to estimate all three using only SST. To test this, the observability of the state vector with nine parameters was verified numerically with covariance analysis, using the criterion on pp. 237-240 of Tapley et al. (2004). This nine-parameter state vector can be written:

$$\mathbf{X} = [a_1 \quad e_1 \quad \nu_1 \quad a_2 \quad e_2 \quad \nu_2 \quad d \quad c_1 \quad c_2]^T.$$

The observations can be related to the state with the \tilde{H} matrix, which is

$$\tilde{H}_i = \left[\frac{\partial G}{\partial \mathbf{X}} \right]_i^*. \quad (2.7)$$

G is a function that computes observations, Y_i , from a state vector, \mathbf{X}_i , at time t_i in the following way:

$$\mathbf{Y}_i = G(\mathbf{X}_i, t_i) + \epsilon_i. \quad (2.8)$$

ϵ_i is the observation error. For this test, crosslink range, ρ , is the observation type. ρ can be written in terms of the semimajor axis, eccentricity, true anomaly, and the relative orientation parameters defined in Eqs. 2.4 through 2.6.

$$\rho = \sqrt{r_1^2 + r_2^2 - 2r_1r_2 [\cos(c_1 - \nu_1) \cos(c_2 - \nu_2) + \sin(c_1 - \nu_1) \sin(c_2 - \nu_2) \cos(d)]} \quad (2.9)$$

$$r_1 = \frac{a_1(1 - e_1^2)}{1 + e_1 \cos(\nu_1)} \quad r_2 = \frac{a_2(1 - e_2^2)}{1 + e_2 \cos(\nu_2)} \quad (2.10)$$

\tilde{H}_i would then be of the form:

$$\tilde{H}_i = \left[\frac{\partial \rho}{\partial a_1} \quad \frac{\partial \rho}{\partial e_1} \quad \frac{\partial \rho}{\partial \nu_1} \quad \frac{\partial \rho}{\partial a_2} \quad \frac{\partial \rho}{\partial e_2} \quad \frac{\partial \rho}{\partial \nu_2} \quad \frac{\partial \rho}{\partial d} \quad \frac{\partial \rho}{\partial c_1} \quad \frac{\partial \rho}{\partial c_2} \right]_i.$$

The \tilde{H}_i matrix at time t may be mapped back to the initial epoch, t_k , with the state transition matrix, Φ . The result is the H_i matrix:

$$H_i = \tilde{H}_i \Phi(t_i, t_k). \quad (2.11)$$

So H_i is the observation-state relationship at t_i mapped back to the initial epoch t_k . If there are ℓ observations, all of them can be combined into a vector, and all of the H_i matrices into a larger matrix so that

$$H \equiv \begin{bmatrix} H_1 \\ \vdots \\ H_\ell \end{bmatrix}. \quad (2.12)$$

If it is assumed that the observation errors can be modeled as white noise, and the standard deviation in the observation noise is denoted σ_ρ , $W = 1/\sigma_\rho^2$ can be used to weight the observations and the matrix $H^T W H$ can be accumulated one observation at a time:

$$H^T W H = \sum_{i=1}^{\ell} H_i^T W H_i. \quad (2.13)$$

$H^T W H$ is also called the information matrix, Λ . The entire state is observable only if Λ is positive definite. Numerically, the state is observable if the condition number of Λ is less than 10^{16} . The variance-covariance matrix is the inverse of the information matrix:

$$P = \Lambda^{-1}. \quad (2.14)$$

The covariance matrix can be used to compute the variances of the state parameters as well as the correlations between state parameters.

Ephemerides were simulated for two spacecraft in various low Earth orbits. These ephemerides were propagated over six-hour time periods. \tilde{H}_i and $\Phi(t_i, t_k)$ were generated every 20 seconds and σ_ρ was set to be 1 m. After accumulating the information matrix for each set of orbits, it was found that the entire nine-parameter state, including d , c_1 , and c_2 , was observable using only crosslink range.

Using the same orbits, the three relative orientation parameters in the state vector were replaced with three of the Keplerian orientation parameters in all their possible combinations.

Eqs. 2.4 through 2.6 were substituted into Eq. 2.9 to get the range in terms of the Keplerian orientation elements. None of these combinations of three Keplerian orientation elements were observable. These results lead to the conclusion that there are inherent limitations in the Keplerian orientation elements that make it impossible to estimate three simultaneously using only SST in the two-body problem.

Liu and Liu were able to create an observable state by fixing four of the unknowns, i_1 , i_2 , Ω_1 , and Ω_2 , and solving for the other two, ω_1 and ω_2 . To see if there were other combinations of two Keplerian orientation parameters that could be observed, the observability tests were repeated. This time the state vector was defined so that it only included two of the Keplerian orientation parameters in different combinations. The results of that study show that it is possible to solve for any combination of two orientation-type Keplerian elements except for Ω_1 and Ω_2 . This is because Ω_1 and Ω_2 only appear in the equations in difference form ($\Delta\Omega$), so Ω_1 and Ω_2 cannot be estimated simultaneously.

2.2.2 Example 2: Two-body Problem with J_2 .

Suppose that the gravity model for the Earth is expanded to include the J_2 term representing the equatorial bulge of the Earth. A vector field obtained from the acceleration function $\mathbf{f}(\mathbf{r}, t)$ is plotted in Figure 2.3. The J_2 term was exaggerated for this figure so that the resulting pattern would be easily visible. In this case, the function $\mathbf{f}(\mathbf{r}, t)$ is symmetric about the z axis and the equatorial plane. If the initial position of a spacecraft is $\mathbf{r}_0 = [x_0 \ y_0 \ z_0]^T$, then there can be orbits of the same size and shape beginning anywhere on two circles described by the equations

$$x^2 + y^2 = x_0^2 + y_0^2 \quad \text{and} \quad z = \pm z_0.$$

If there were two spacecraft orbiting the Earth in this model, SST observations could be used to observe ten of the twelve state parameters. The two unobservable parameters would be the absolute positions along the circles as well as the sign of the z components of the initial state. If *a priori* information on the location of the initial state were available with sufficient accuracy,

the sign of the z component of the initial position and velocity would be known, and eleven of the state parameters would be observable. The uncertainty in the *a priori* information would have to be smaller than $2z_0$ to be able to distinguish the proper sign on the z components. Thus, with *a priori* information of sufficient accuracy, the Keplerian orientation elements i_1 , i_2 , $\Delta\Omega$, ω_1 , and ω_2 could be estimated.

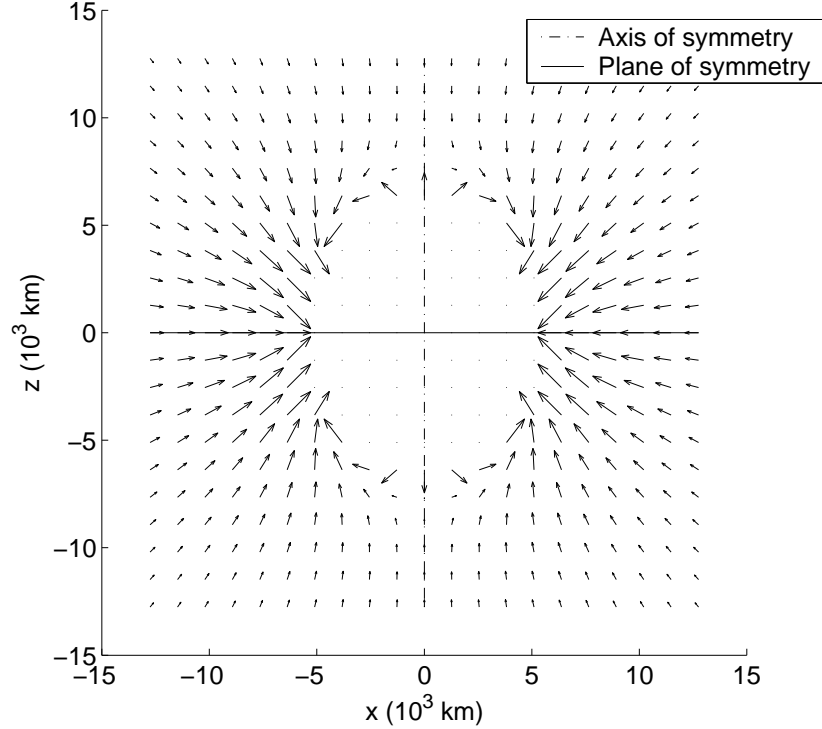


Figure 2.3: The vector field of accelerations in the x - z plane for Example 2 with exaggerated J_2 .

2.2.3 Example 3: Three-body Earth-Moon System.

The system includes the Earth as a point mass. The Moon, represented by a point mass as well, orbits the Earth. For this example, the inertial coordinate system will be centered on the Earth-Moon barycenter. At t_0 , the x axis extends through the point masses of the Earth and the Moon. The Earth and the Moon's orbits are in the x - y plane with the moon's velocity vector in the positive y direction. The z axis would be orthogonal to the x and y axes using the right hand rule. Figure 2.4 shows the structure of $\mathbf{f}(\mathbf{r}, t)$. For this figure, the mass of the

Moon was exaggerated to make the pattern more visible. The accelerations are symmetric about the x axis. However, since the Moon and the Earth are moving about the barycenter in the inertial frame, $\frac{d}{dt}\mathbf{f}(\mathbf{r}, t)$ would not be symmetric across the x-z plane. The only plane without asymmetry in either $\mathbf{f}(\mathbf{r}, t)$ or $\frac{d}{dt}\mathbf{f}(\mathbf{r}, t)$ would be the x-y plane. In this case, the possible initial positions for each satellite would consist of two points, mirrored across the x-y plane. The sign of the z components of the position and velocity could not be estimated, so only eleven of the twelve state parameters are estimable. If *a priori* knowledge of the state is available, and the two mirrored points are far enough apart, the orbit can be said to be locally unique, and all twelve of the state parameters for the two satellites could be estimated. The uncertainty in the *a priori* knowledge of the state would have to be less than the distance between the two possible solutions for this to succeed. This means that if both orbits remain very near the x-y plane, SST would only be able to estimate eleven of the twelve state parameters.

When the asymmetry is in the time derivative, $\frac{d}{dt}\mathbf{f}(\mathbf{r}, t)$, the fit span needs to be sufficiently long that changes in $\mathbf{f}(\mathbf{r}, t)$ are readily observable. In this case, since $\frac{d}{dt}\mathbf{f}(\mathbf{r}, t)$ has a period equal to that of the Moon's orbit around the Earth, the fit span would need to be a significant portion of the Moon's orbit period for all of the state parameters to be estimated.

2.2.4 Example 4: Two-body problem with Solar Radiation Pressure

This system includes Earth's gravity and the acceleration due to solar radiation pressure (SRP). The Sun's initial position is on the positive y axis, and the Sun's gravitational influence is neglected. For this example, the Sun orbits the Earth with a period of one year, and it would be assumed that accelerations due to SRP would only be a function of position relative to the Sun. In other words, the spacecraft would have the same area, mass, and reflectance properties for all attitudes. In this case, the function $\mathbf{f}(\mathbf{r}, t)$ is symmetric about the y axis. Similar to Example 3, $\frac{d}{dt}\mathbf{f}(\mathbf{r}, t)$ is asymmetric about the y-z plane due to the Sun's motion around the Earth. Two orbits would exist with the same size and shape, but if the two solutions are sufficiently far apart, they can be said to be locally unique. In that case, two satellites orbiting

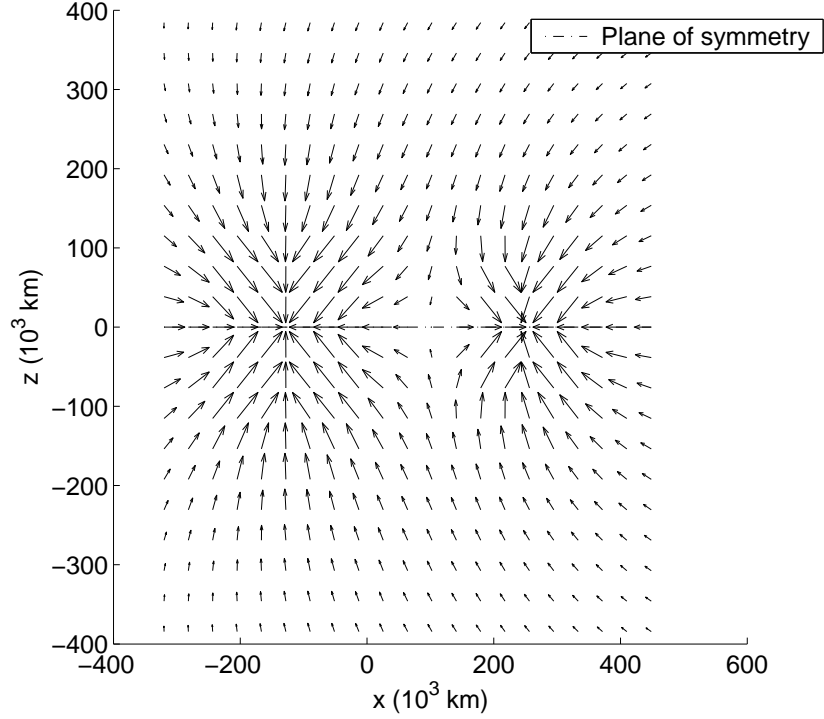


Figure 2.4: The vector field of accelerations in the x-z plane for Example 3 with the Earth and the Moon.

the Earth would be able to observe all twelve state parameters using SST with proper *a priori* information. In this case, since $\frac{d}{dt}\mathbf{f}(\mathbf{r}, t)$ has a period equal to that of the Earth's orbit around the Sun, the fit span would need to be a significant portion of the Earth's orbit period. The geometry of SRP accelerations in this model enables absolute positioning with SST. However, if the two spacecraft were in heliocentric orbits, the geometry of the SRP accelerations would be symmetric about the center of mass of the Sun, and absolute positioning would not be possible.

2.2.5 Example 5: Non-uniform Central Body Gravity.

The system is limited to Earth and nearby space, but the Earth's gravity field is non-uniform or asymmetric. With no symmetry present in the function $\mathbf{f}(\mathbf{r}, t)$, the orbit generated with each set of initial conditions would be unique. In this simplified case, it would be possible to estimate the absolute positions and velocities of two spacecraft using only SST. However, in

reality, the subtle changes in orbit shape and size due to the asymmetric gravity field might be difficult to detect in the presence of observation noise and uncertainties in the force model due to drag and other perturbations. In this case, and in all the other cases, the strength of the asymmetry will determine whether SST can actually be used for absolute positioning.

2.3 Strength of the Asymmetry

While absolute positioning with SST is theoretically possible using the asymmetry in some of these acceleration functions, observation noise and uncertainties in the spacecraft force model could obliterate the effects of these asymmetric accelerations on the resulting orbital path. For practical purposes, the effect of the asymmetric acceleration on the spacecraft trajectory must be significantly greater than the observation noise and the effects due to unmodeled accelerations. Some of the unmodeled accelerations would include uncertainties in atmospheric drag, thruster firings, the central gravity field, and parameters that affect acceleration due to SRP such as reflectance properties and spacecraft attitude. One way of evaluating the strength of these asymmetric accelerations is to look at the magnitude of the acceleration caused by the perturbations compared to the sum of the magnitudes of all of the accelerations. The parameter α will be used to quantify the relative strength of these perturbations.

$$\alpha_j(x, y, z) = \frac{|\ddot{\mathbf{r}}_j(x, y, z)|}{\sum_{i=1}^n |\ddot{\mathbf{r}}_i(x, y, z)|} \quad (2.15)$$

If there are n forces causing the spacecraft to accelerate, $\ddot{\mathbf{r}}_i(x, y, z)$ represents an acceleration due to force i at location (x, y, z) , with $i = 1 \dots n$. The larger the value of $\alpha_j(x, y, z)$ for an asymmetric acceleration, the more likely that a spacecraft at location (x, y, z) would be able to use SST for absolute positioning. Two-dimensional maps of α were created for a simplified Earth-centered system. The coordinate axes were Earth Centered Inertial with the Earth modeled as a point mass. The maps were created to depict a single instant in time. At that instant, the positive x axis extends through the Moon's point mass, and the positive y axis, which is perpendicular to the x axis, extends through the Sun's point mass. Accelerations due to drag,

J_2 , SRP, Earth's point mass, and the perturbations due to the Moon and Sun were included in the calculations and computed using equations from pp. 61-68 of Tapley et al. (2004).

$$\mathbf{a}_{\oplus} = \frac{\mu_{\oplus}}{|\mathbf{r}_{\oplus\text{sat}}|^2} \cdot \frac{\mathbf{r}_{\oplus\text{sat}}}{|\mathbf{r}_{\oplus\text{sat}}|} \quad (2.16)$$

$$|a_{J_2}| = \frac{3}{2} J_2 \mu_{\oplus} r_{\oplus}^2 \sqrt{\frac{x^4 + 4z^4}{(x^2 + z^2)^6}} \quad (2.17)$$

$$\mathbf{a}_{\zeta} = \mu_{\zeta} \left(\frac{\mathbf{r}_{\text{sat}\zeta}}{|\mathbf{r}_{\text{sat}\zeta}|^3} - \frac{\mathbf{r}_{\oplus\zeta}}{|\mathbf{r}_{\oplus\zeta}|^3} \right) \quad (2.18)$$

$$\mathbf{a}_{\odot} = \mu_{\odot} \left(\frac{\mathbf{r}_{\text{sat}\odot}}{|\mathbf{r}_{\text{sat}\odot}|^3} - \frac{\mathbf{r}_{\oplus\odot}}{|\mathbf{r}_{\oplus\odot}|^3} \right) \quad (2.19)$$

$$\mathbf{a}_{SRP} = \frac{-p_{SR} c_R A}{m} \cdot \frac{\mathbf{r}_{\text{sat}\odot}}{|\mathbf{r}_{\text{sat}\odot}|^3} \quad (2.20)$$

$$|a_{\text{drag}}| = \frac{1}{2} \frac{c_D A}{m} \rho \cdot V^2 \quad (2.21)$$

$$\rho = \rho_0 e^{\frac{r_0 - |\mathbf{r}_{\oplus\text{sat}}|}{H}} \quad (2.22)$$

$$V = \sqrt{\frac{\mu_{\oplus}}{|\mathbf{r}_{\oplus\text{sat}}|}} \quad (2.23)$$

p_{SR} is the solar radiation pressure (4.51×10^{-6} N/m²), c_R is the coefficient of reflectance (1.5), A is the cross-sectional area of the spacecraft (10 m²), m is the mass of the spacecraft (1000 kg), and ρ_0 , r_0 , and H are constants used to compute atmospheric density (3.614×10^{-13} kg/m³, 706,378.14 km, and 88,667.0 km respectively). The velocity used in the drag calculations, V , is the velocity in a circular orbit at that radius. $\mathbf{r}_{\text{sat}\odot}$ is a position vector from the satellite to the Sun, $\mathbf{r}_{\oplus\text{sat}}$ is the vector from the Earth to the satellite, $\mathbf{r}_{\text{sat}\zeta}$ is a vector from the satellite to the Moon, $\mathbf{r}_{\oplus\zeta}$ is the vector from the Earth to the Moon, and finally $\mathbf{r}_{\oplus\odot}$ is the vector from the Earth to the Sun. μ_{\oplus} is the gravitational parameter for the Earth ($398,600.4415$ km³/s²), μ_{ζ} is the gravitational parameter of the Moon (4902.799 km³/s²), and μ_{\odot} is the gravitational parameter for the Sun ($1.32712428 \times 10^{11}$ km³/s²).

Figure 2.5 shows a map of α for the SRP perturbation. The relative strength of the SRP perturbation in Figure 2.5 increases with distance from the Earth and the Moon. However,

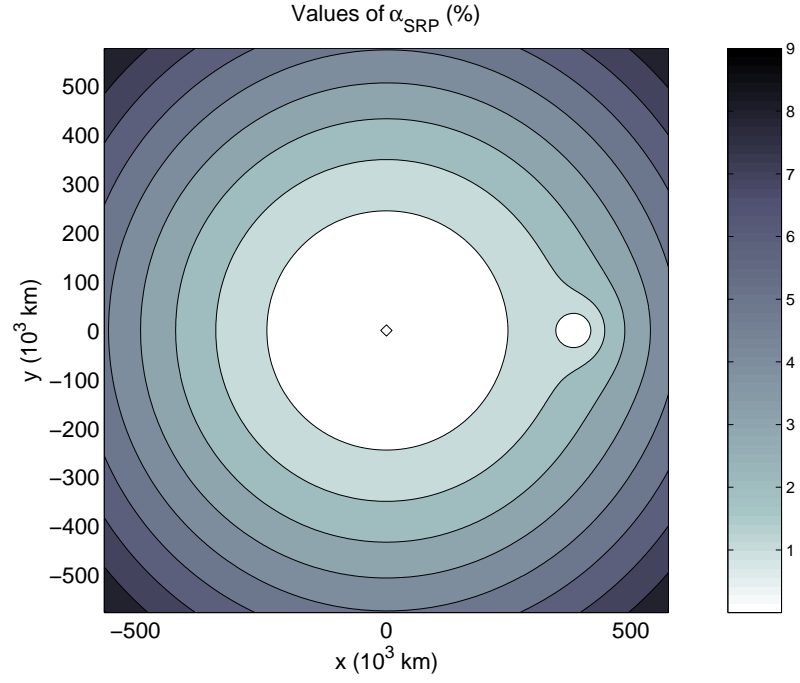


Figure 2.5: Map of α for acceleration due to SRP in the Earth-Moon system.

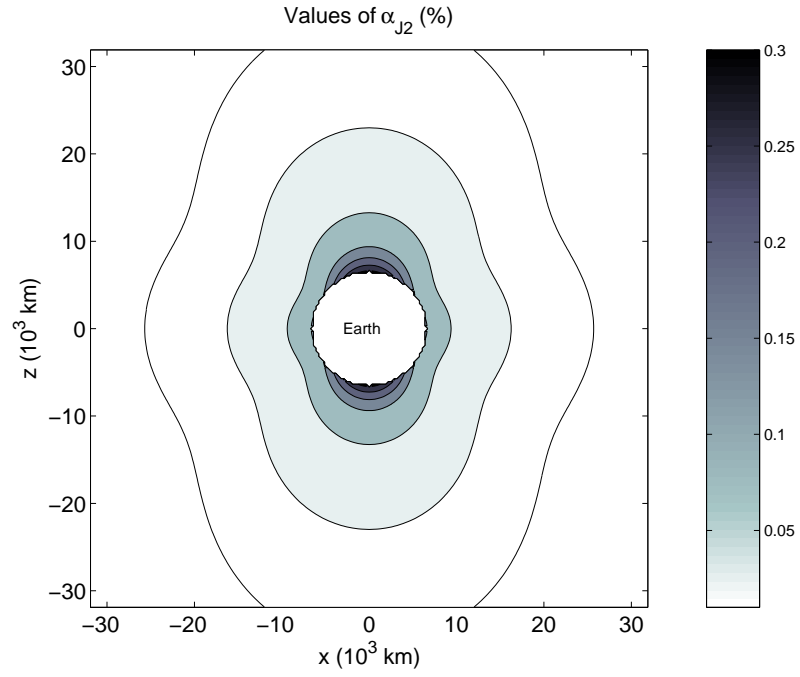


Figure 2.6: Map of α for acceleration due to \mathbf{J}_2 in the Earth system.

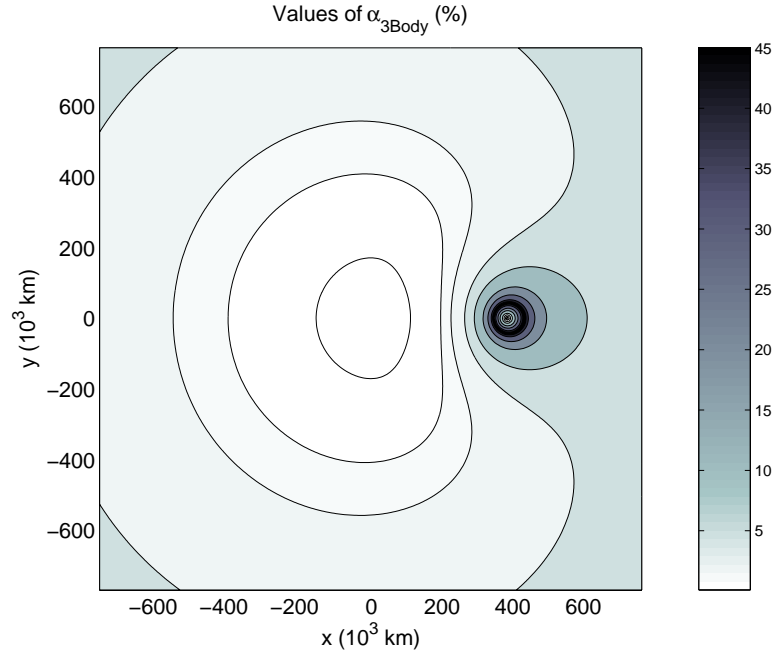


Figure 2.7: Map of α for acceleration due to the third body in the Earth-Moon system.

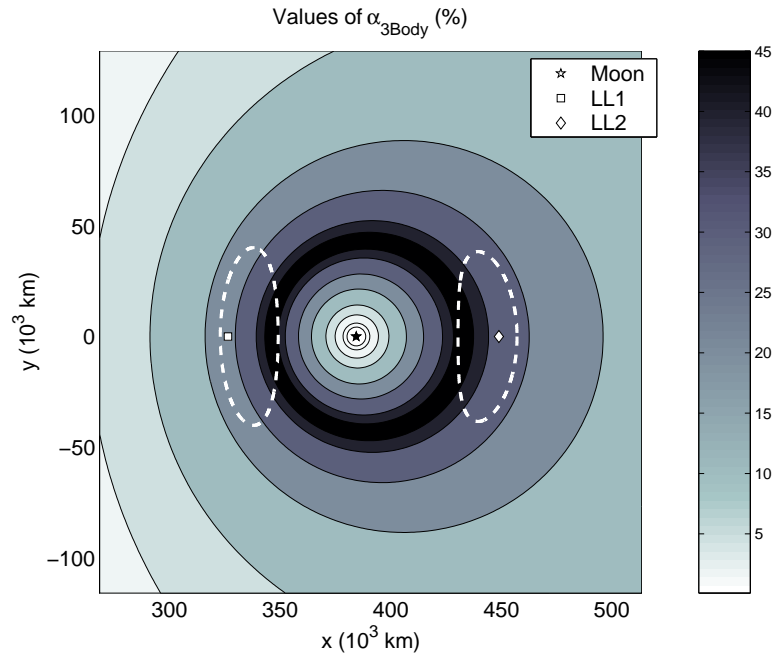


Figure 2.8: Map of α near the Moon for acceleration due to the third body in the Earth-Moon system. The positions of the lunar L_1 and L_2 Lagrange points are shown along with a halo orbit around each.

the usefulness of SRP in absolute positioning with SST is limited to non-heliocentric orbits. Most useful non-heliocentric orbits in the Earth-Moon system lie close to either the Earth or the Moon. That makes it less likely that asymmetry due to SRP will lead to practical orbit determination using only SST.

Figure 2.6 shows a map of α for the J_2 perturbation. The J_2 coefficient was not exaggerated for this figure. While the J_2 term alone does not provide sufficient asymmetry to estimate all of the satellite state parameters, it is interesting to see the relative strength of the J_2 accelerations. If the J_2 accelerations have a large relative magnitude, that could mean the asymmetry in Earth's true gravity field might be strong enough to enable orbit determination using only SST. Figure 2.6 shows that the relative strength of the J_2 accelerations is small. That seems to indicate that orbit determination with only SST using the asymmetry of the Earth's gravity field would probably be inaccurate or impossible.

Figure 2.7 shows a map of α for the third-body perturbation. Earth is at the origin in this plot. For this figure, the definition of the third body depends on location. When the spacecraft is close to the Earth and the gravitational force due to the Earth is the strongest, the Moon is defined as the third body. When the spacecraft is close enough to the Moon that the Moon's gravitational influence is stronger than the Earth's, then the Earth is considered the third body. Figure 2.7 shows that the third-body perturbation is significantly stronger than the other perturbations, especially in a nearly spherical shell around the Moon. This result indicates that three-body gravity is the most likely perturbation to enable autonomous orbit determination using SST. Figure 2.8 shows that halo orbits around the lunar Lagrange points L_1 and L_2 stay within regions of high α for their entire periods.

2.4 Summary

It has been hypothesized that asymmetry in the acceleration field can enable autonomous orbit determination using only SST. We propose a new type of navigation called the Linked Autonomous Interplanetary Satellite Orbit Navigation (LiAISON) method, hereafter referred

to as Liaison Navigation, where only SST is used to determine the orbits of multiple spacecraft when at least one is in a locally unique orbit. According to Merriam-Webster (1994), liaison means “communication for mutual understanding.” Liaison Navigation is a method of establishing and maintaining mutual understanding of the orbits of participating spacecraft through communication.

The third-body perturbation in the Earth-Moon system has the strongest asymmetric acceleration and is the most likely to enable successful application of Liaison Navigation. L_1 and L_2 halo orbits stay in regions of relatively strong asymmetry, so they are excellent candidates for running autonomous orbit determination simulations. The existence of symmetric northern and southern halo orbits, which are mirrored across the moon’s orbit plane, is in agreement with our analysis that the third-body perturbation is symmetric across the moon’s orbit plane.

Chapter 3 gives a description of the Circular Restricted Three-Body Problem (CRTBP). The results of simulations of Liaison Navigation for spacecraft in halo orbits in the Earth-Moon CRTBP are included in Chapter 4.

Chapter 3

The Circular Restricted Three-body Problem

In the Circular Restricted Three-Body Problem (CRTBP), there are two massive bodies in orbit about their mutual barycenter (Murray and Dermott, 1999), as depicted in Figure 3.1. To simplify the model, each body orbits the barycenter in the same plane in perfectly circular orbits. A spacecraft with infinitesimal mass experiences forces due to the gravitational influence of both bodies simultaneously, and the two bodies are approximated as point masses. The more massive body is labeled P_1 , and the other is P_2 . The coordinate frame has its origin at the barycenter and rotates with the two bodies so that P_1 and P_2 are always on the x axis, with the positive x direction going from P_1 to P_2 . The positive y axis is parallel to the velocity vector of P_2 . The three-body gravitational parameter is called μ and

$$\mu = \frac{m_2}{m_1 + m_2}. \quad (3.1)$$

where m_1 is the mass of P_1 , and m_2 is the mass of P_2 . The mass of the primaries is nondimensionalized so that the mass of P_2 is defined to be μ and the mass of P_1 is $1 - \mu$. One nondimensional length unit (LU) is equal to the distance between the two primaries, so the distance along the x axis from the origin to P_1 is $-\mu$ LU and from the origin to P_2 is $1 - \mu$ LU. The time unit (TU) is defined such that P_2 orbits around P_1 in 2π TU.

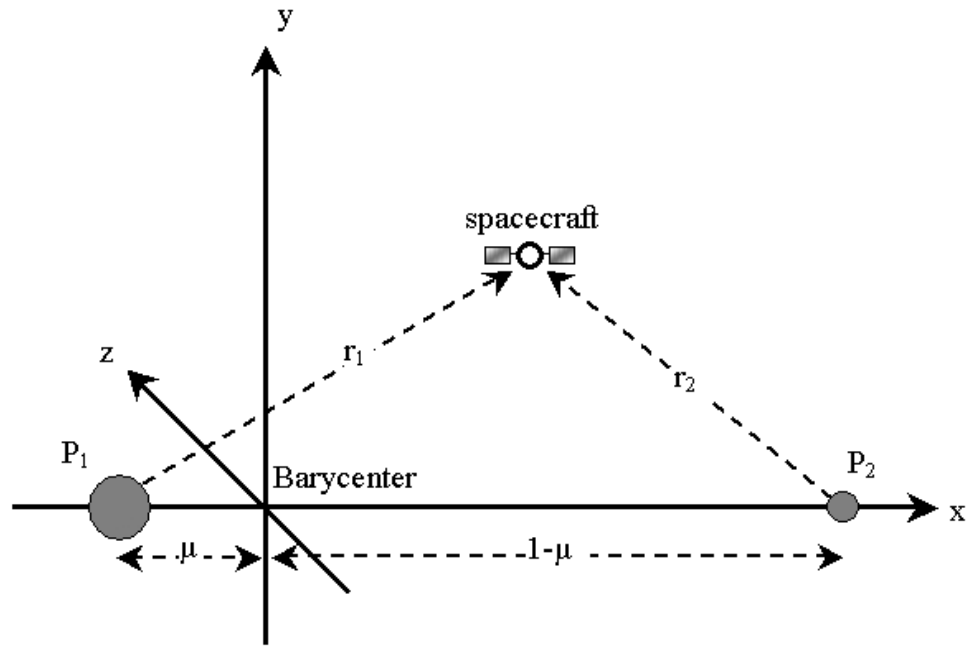


Figure 3.1: Diagram of the Circular Restricted Three-Body Problem with a rotating, nondimensional coordinate frame.

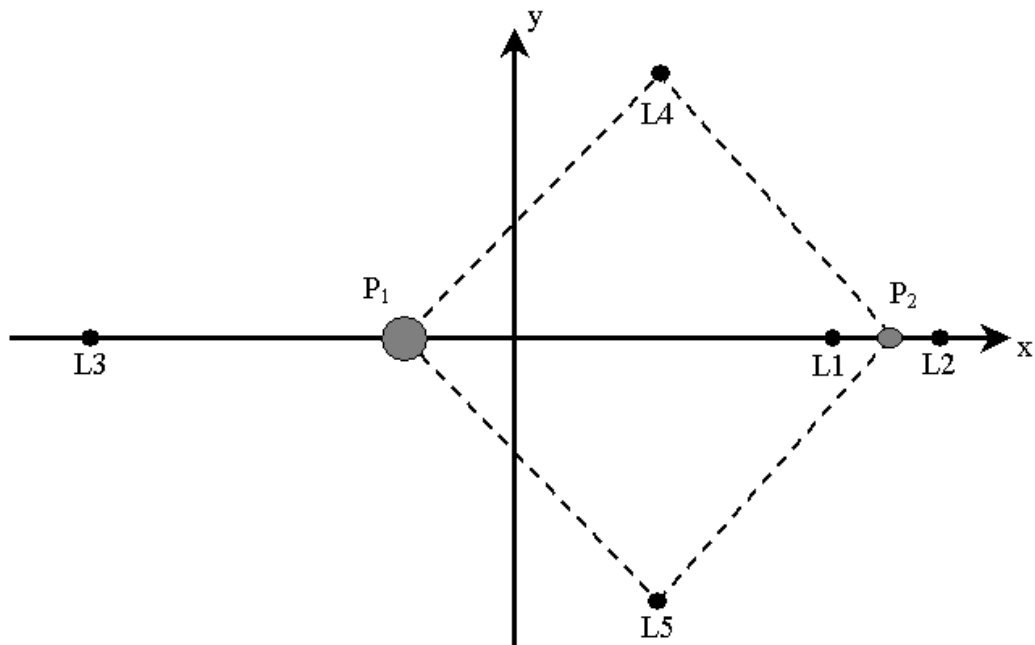


Figure 3.2: Schematic location of the five Lagrange points in the CRTBP.

The equations of motion for the CRTBP are

$$\ddot{x} - 2\dot{y} = x - (1 - \mu)\frac{x + \mu}{r_1^3} - \mu\frac{x + \mu - 1}{r_2^3}, \quad (3.2)$$

$$\ddot{y} + 2\dot{x} = \left(1 - \frac{1 - \mu}{r_1^3} - \frac{\mu}{r_2^3}\right)y, \quad (3.3)$$

$$\text{and } \ddot{z} = \left(\frac{\mu - 1}{r_1^3} - \frac{\mu}{r_2^3}\right)z. \quad (3.4)$$

$$\text{where } r_1 = \sqrt{(x + \mu)^2 + y^2 + z^2} \quad \text{and} \quad r_2 = \sqrt{(x + \mu - 1)^2 + y^2 + z^2}.$$

Five equilibrium points exist in the CRTBP when using a rotating coordinate frame. These are locations where the gravitational acceleration is balanced by centripetal acceleration. A spacecraft placed on an equilibrium point with zero velocity will remain at that equilibrium point indefinitely. These points are called Lagrange points, and they are shown schematically in Figure 3.2. Three of the equilibrium points are on the x axis. L_3 is on the far side of the larger body, L_1 lies between the two bodies, and L_2 is on the far side of the smaller body. L_4 and L_5 are in the x-y plane, and each forms an equilateral triangle with the two bodies.

The Lagrange points for various three-body systems will be abbreviated as shown in Table 3.1.

Table 3.1: ABBREVIATIONS FOR LAGRANGE POINTS IN VARIOUS THREE-BODY SYSTEMS.

Three-body System	Lagrange Point Abbreviations
Earth-Moon	LL ₁ , LL ₂ , LL ₃ , LL ₄ , LL ₅
Sun-Jupiter	JL ₁ , JL ₂ , JL ₃ , JL ₄ , JL ₅
Saturn-Titan	TL ₁ , TL ₂ , TL ₃ , TL ₄ , TL ₅
Jupiter-Io	IL ₁ , IL ₂ , IL ₃ , IL ₄ , IL ₅
Sun-Earth	EL ₁ , EL ₂ , EL ₃ , EL ₄ , EL ₅
Sun-Mars	AL ₁ , AL ₂ , AL ₃ , AL ₄ , AL ₅

The three collinear Lagrange points, L_1 , L_2 , and L_3 are unstable equilibrium points, and trajectories in their vicinity are unstable as well (Murray and Dermott, 1999). This means that stationkeeping maneuvers must be performed frequently in these areas.

3.1 Lissajous orbits

Many interesting families of three-body orbits exist (Broucke, 1968). In this research, the most useful orbits were those that remained in the vicinity of the Lagrange points, also called libration point orbits.

For an object orbiting a libration point, analytic expressions describing the trajectory show that there is periodic motion in the orbit plane of the primaries, which would be the x-y plane for the coordinate system described above. There is also periodic motion in the out-of-plane direction, or the z direction (Richardson, 1980). For various ratios of these frequencies, the libration point orbit traces out a shape similar to a Lissajous figure, leading to the name of Lissajous orbit (Howell and Pernicka, 1988). Richardson and Cary (1975) formed an analytic expression for these Lissajous orbits in the Sun-Earth three-body problem. Their analytic expansion went to fourth order, with corrections for the eccentricity of the Earth's orbit and for the gravitational perturbations of the Moon. Their expressions can easily be generalized to other three-body systems by excluding the perturbation terms due to the Moon and the eccentricity. Generally, the fourth order terms are not needed.

The technique described by Richardson and Cary (1975) works by providing the amplitude of the x-y plane oscillation and the amplitude of the out-of-plane (z component) oscillation. The position and velocity along the Lissajous orbit can then be computed. Howell and Pernicka (1988) show an example of an analytical Lissajous trajectory in the Sun-Earth three-body system with an amplitude of 200,000 km in the y direction and 200,000 km in the z direction. This is duplicated in Figure 3.3. In Chapter 7, there is a description of the technique used to find these Lissajous orbits numerically.

3.2 Halo orbits

If the amplitudes of the oscillation of a Lissajous orbit are large enough, nonlinear effects become important and the frequencies of the two oscillations can be the same. When the two

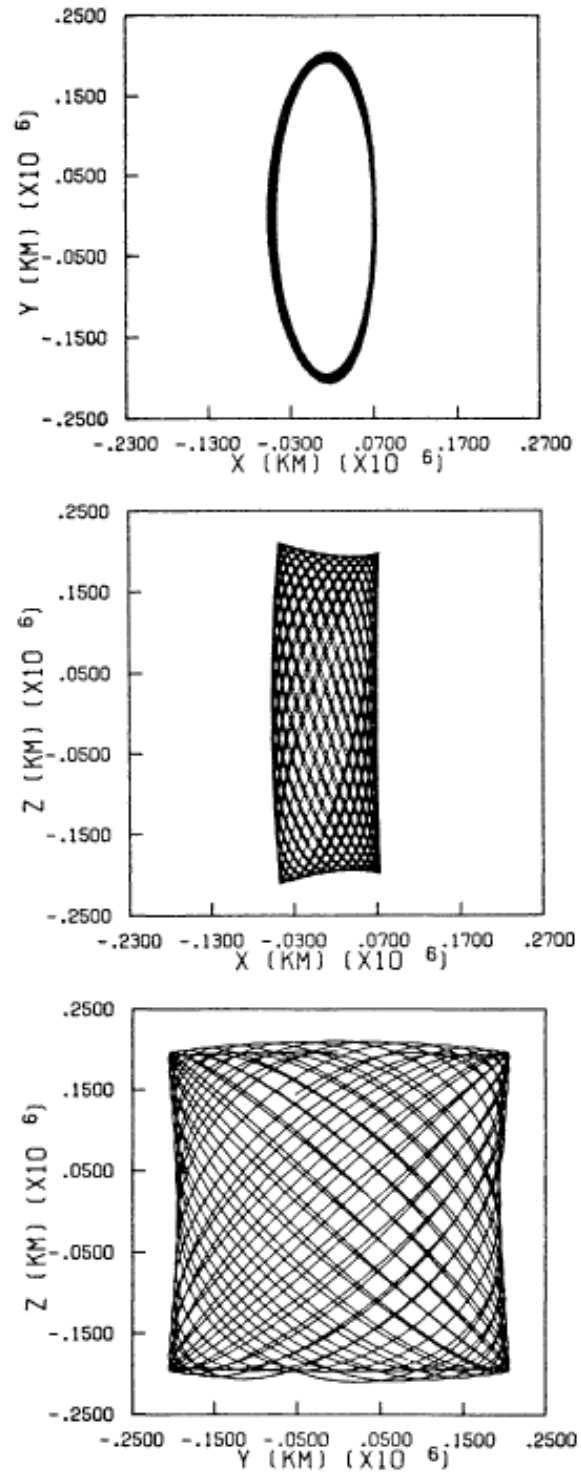


Figure 3.3: Third-order Lissajous trajectory in the Sun-Earth three-body problem with y and z amplitudes of 200,000 km. Figure 1 from Howell and Pernicka (1988)

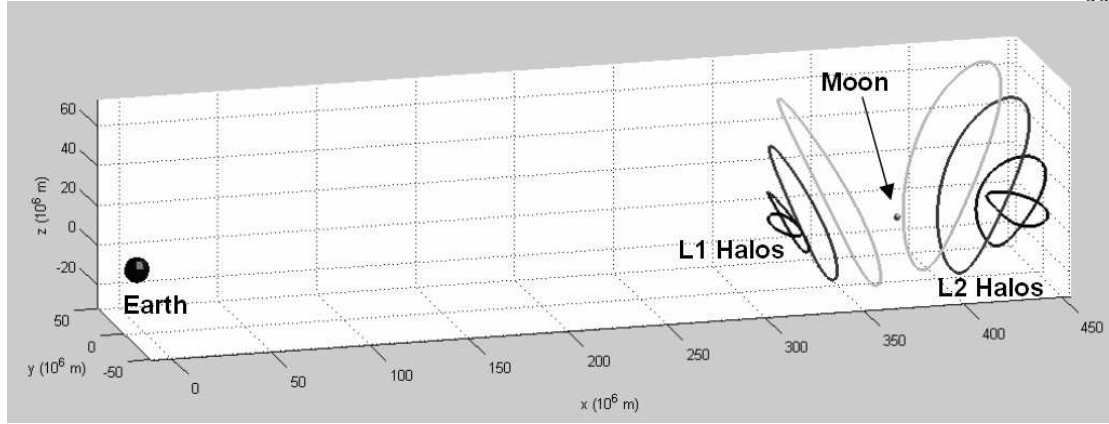


Figure 3.4: L_1 and L_2 halo orbits in the Earth-Moon system in the rotating frame.

frequencies are equal, a periodic orbit is the result. Farquhar (1970) created the name ‘halo’ for these orbits and proposed using a halo orbit at LL_2 to provide continuous communications for the far side of the Moon. Farquhar and Kamel (1973) created an analytical solution for halo orbits at LL_2 including perturbations. The third order analytical solution published by Richardson (1980) is applicable to any three-body system and is a good way of obtaining an initial state which can be differentially corrected using numerical methods.

To determine halo orbits numerically, a guess at the initial state is obtained at the x - z plane with velocity only in the y direction. Then an orbit is propagated using the CRTBP equations of motion. When the orbit crosses the x - z plane again, the state transition matrix is used in a differential corrector to adjust the initial conditions so that the velocity at the second x - z plane crossing is perpendicular to the x - z plane. This is done in an iterative manner until the velocity at the second crossing of the x - z plane is perpendicular to within a certain tolerance. Figure 3.4 shows some members of the LL_1 and LL_2 halo orbit families to scale. Chapter 6 has more information on halo orbits in six representative three-body systems.

When placing the spacecraft in halo orbits, it became convenient to define a phase angle, τ . τ is a non-geometric angle describing the positions of the spacecraft in the halos in a manner similar to mean anomaly in that the phase angle has a constant time derivative. A phase angle

of zero occurs when the spacecraft is on the halo orbit where it intersects the x-z plane traveling in the positive y direction. The phase angle increases in the direction of the orbital motion and is defined as

$$\tau_i = \frac{(t_i - t_0)}{p} 2\pi, \quad (3.5)$$

where $(t_i - t_0)$ is the time past the x-z plane crossing (at $\tau = 0$) and p is the halo orbit period. Figure 3.5 shows some values of τ on a halo orbit which has been projected onto the x-y plane. The phase angles are not evenly spaced because the velocity of the spacecraft varies along the halo orbit.

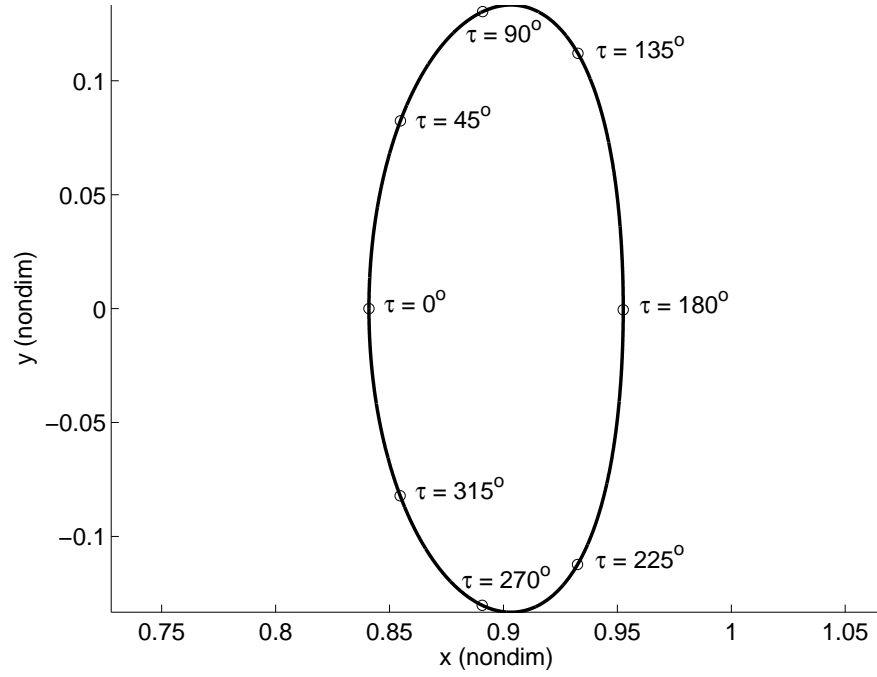


Figure 3.5: Positions of various values of the phase angle, τ , on a halo orbit in the Earth-Moon system projected onto the x-y plane.

Chapter 4

Liaison Navigation in Lunar Halo Orbits

Liaison Navigation is the use of SST alone to determine the orbits of two or more participating spacecraft when one of them is in an orbit of a locally unique size and shape. It was shown in Chapter 2 that the third-body perturbation of the Moon provides enough asymmetry in the acceleration field that locally unique orbits exist as long as they are not restricted to the plane of the Moon's orbit. Liaison Navigation for two spacecraft in close proximity was shown to be more likely to succeed in the regions where the gravitational forces of the Earth and the Moon were similar in magnitude. Orbits around the Lunar L_1 and L_2 libration points are ideal for testing Liaison Navigation since those orbits are locally unique and always remain in regions where the asymmetry of the third-body perturbation is very strong. In this chapter, orbit determination simulations will be used to show that Liaison Navigation is feasible in lunar halo orbits in the CRTBP (Hill et al., 2005a).

4.1 Liaison Navigation Methods

Orbit determination is an attempt to estimate the initial conditions of the nonlinear system of differential equations describing spacecraft motion using measurements that are nonlinear with respect to the state. This is done by linearizing about a reference orbit that is close to the actual orbit. Instead of estimating the initial state with the measurements, the error in the initial state is estimated using the observation residuals, which are the observed measurements minus those computed from the reference solution. Liaison Navigation can be conducted using

any type of orbit determination method. However, in this chapter the two different techniques used were the batch processor and the Kalman filter. A summary of these techniques comes from Tapley et al. (2004) and uses their notation. For illustrative purposes, the equations are shown for two spacecraft, although the number of spacecraft participating can be larger.

The spacecraft state consists of three position and velocity components for each spacecraft. For two spacecraft, it would be

$$\mathbf{X} = [x_1 \ y_1 \ z_1 \ \dot{x}_1 \ \dot{y}_1 \ \dot{z}_1 \ x_2 \ y_2 \ z_2 \ \dot{x}_2 \ \dot{y}_2 \ \dot{z}_2]^T,$$

where the subscripts denote the spacecraft number. The equations of motion are written

$$\dot{\mathbf{X}} = F(\mathbf{X}, t), \quad (4.1)$$

where $\mathbf{X}_i \equiv \mathbf{X}(t_i)$. An observation at time t_i is denoted by \mathbf{Y}_i , and $\mathbf{x}(t)$, the state deviation, and $\mathbf{y}(t)$, observation residuals, are written

$$\mathbf{x}(t) = \mathbf{X}(t) - \mathbf{X}^*(t) \quad (4.2)$$

$$\text{and } \mathbf{y}(t) = \mathbf{Y}(t) - \mathbf{Y}^*(t), \quad (4.3)$$

where \mathbf{X}^* is the reference solution, or the “best guess” orbit, and \mathbf{Y}^* is an observation computed using the reference solution. The observations can be related to the state with the \tilde{H} matrix, which is

$$\tilde{H}_i = \left[\frac{\partial G}{\partial \mathbf{X}} \right]_i^*. \quad (4.4)$$

G is a function that computes observations from a state vector in the following way:

$$\mathbf{Y}_i = G(\mathbf{X}_i, t_i) + \epsilon_i. \quad (4.5)$$

ϵ_i is the observation error. If crosslink range, ρ , and crosslink range rate, $\dot{\rho}$, are the observations types then \tilde{H}_i is of the form:

$$\tilde{H}_i = \begin{bmatrix} \frac{\partial \rho}{\partial x_1} & \frac{\partial \rho}{\partial y_1} & \frac{\partial \rho}{\partial z_1} & \frac{\partial \rho}{\partial \dot{x}_1} & \frac{\partial \rho}{\partial \dot{y}_1} & \frac{\partial \rho}{\partial \dot{z}_1} & \frac{\partial \rho}{\partial x_2} & \frac{\partial \rho}{\partial y_2} & \frac{\partial \rho}{\partial z_2} & \frac{\partial \rho}{\partial \dot{x}_2} & \frac{\partial \rho}{\partial \dot{y}_2} & \frac{\partial \rho}{\partial \dot{z}_2} \\ \frac{\partial \dot{\rho}}{\partial x_1} & \frac{\partial \dot{\rho}}{\partial y_1} & \frac{\partial \dot{\rho}}{\partial z_1} & \frac{\partial \dot{\rho}}{\partial \dot{x}_1} & \frac{\partial \dot{\rho}}{\partial \dot{y}_1} & \frac{\partial \dot{\rho}}{\partial \dot{z}_1} & \frac{\partial \dot{\rho}}{\partial x_2} & \frac{\partial \dot{\rho}}{\partial y_2} & \frac{\partial \dot{\rho}}{\partial z_2} & \frac{\partial \dot{\rho}}{\partial \dot{x}_2} & \frac{\partial \dot{\rho}}{\partial \dot{y}_2} & \frac{\partial \dot{\rho}}{\partial \dot{z}_2} \end{bmatrix}_i.$$

State deviations at time t may be mapped back to the initial epoch, t_k , with the state transition matrix Φ in the following way:

$$\mathbf{x}(t) = \Phi(t, t_k) \mathbf{x}_k. \quad (4.6)$$

The state transition matrix is integrated along with the state using the following relations:

$$\dot{\Phi}(t, t_k) = A(t) \Phi(t, t_k) \quad (4.7)$$

$$\text{and } A(t) = \frac{\partial F(\mathbf{X}^*, t)}{\partial \mathbf{X}(t)}. \quad (4.8)$$

A is of the form:

$$A = \begin{bmatrix} \frac{\partial \dot{x}_1}{\partial x_1} & \frac{\partial \dot{x}_1}{\partial y_1} & \frac{\partial \dot{x}_1}{\partial z_1} & \cdots & \frac{\partial \dot{x}_1}{\partial \dot{z}_2} \\ \frac{\partial \dot{y}_1}{\partial x_1} & \frac{\partial \dot{y}_1}{\partial y_1} & \frac{\partial \dot{y}_1}{\partial z_1} & & \\ \frac{\partial \dot{z}_1}{\partial x_1} & \frac{\partial \dot{z}_1}{\partial y_1} & \frac{\partial \dot{z}_1}{\partial z_1} & & \vdots \\ \vdots & & & \ddots & \\ \frac{\partial \ddot{z}_2}{\partial x_1} & & \cdots & & \frac{\partial \ddot{z}_2}{\partial \dot{z}_2} \end{bmatrix}^*.$$

Relating an observation at time t_i back to the state initial epoch t_k is done with the H_i matrix:

$$H_i = \tilde{H}_i \Phi(t_i, t_k). \quad (4.9)$$

So, H_i is the observation-state relationship at t_i mapped back to the initial epoch t_k . If there are ℓ observations, all of them can be combined into a vector, and all of the H_i matrices into a larger matrix so that

$$\mathbf{y} = H \mathbf{x}(t_k) + \epsilon \quad (4.10)$$

where

$$\mathbf{y} \equiv \begin{bmatrix} y_1 \\ \vdots \\ y_\ell \end{bmatrix}, \quad H \equiv \begin{bmatrix} H_1 \\ \vdots \\ H_\ell \end{bmatrix}, \quad \text{and} \quad \epsilon \equiv \begin{bmatrix} \epsilon_1 \\ \vdots \\ \epsilon_\ell \end{bmatrix}.$$

A least squares solution for $\mathbf{x}(t_k)$ is computed with the equation

$$\hat{\mathbf{x}} = (H^T H)^{-1} H^T \mathbf{y}. \quad (4.11)$$

If it is assumed that the observation errors are independent and can be modeled as white noise, and the standard deviation in the observation noise for observation type i is denoted σ_i , a weighting matrix W can be used to weight the observations such that

$$\hat{\mathbf{x}} = (H^T W H)^{-1} H^T W \mathbf{y}. \quad (4.12)$$

$$\text{where } W = \begin{bmatrix} \sigma_1^2 & & \\ & \ddots & \\ & & \sigma_n^2 \end{bmatrix}^{-1} \quad \text{and } n \text{ is the number of observation types.} \quad (4.13)$$

The matrices $H^T W H$ and $H^T W \mathbf{y}$ can be accumulated one observation at a time.

$$H^T W H = \sum_{i=1}^{\ell} H_i^T W H_i \quad (4.14)$$

$$H^T W \mathbf{y} = \sum_{i=1}^{\ell} H_i^T W y_i \quad (4.15)$$

$H^T W H$ is also called the information matrix, Λ . The variance-covariance matrix is the inverse of the information matrix:

$$P = \Lambda^{-1}. \quad (4.16)$$

The covariance matrix can be used to compute the variances of the state parameters as well as the correlations between state parameters. The 3×3 position portions of the covariance matrix can also be used to plot a 3D error ellipsoid for each satellite. The eigenvalues of the 3×3 position portions of the covariance matrix correspond to the lengths of the axes of the ellipsoid, and the matrix of eigenvectors is a rotation from the coordinate frame in use to the principle axes coordinate frame. As long as several assumptions are correct, there is a 97% statistical probability that the true initial state lies within the 3D, 3σ error ellipsoid.

If a covariance matrix for the *a priori* estimate of the state, P_0 , is known, it can be included in the computations using the equation

$$\Lambda = P_0^{-1} + \sum_{i=1}^{\ell} H_i^T W H_i. \quad (4.17)$$

When using SST without any Earth-based tracking for orbits in the two-body problem, the initial state is not entirely observable. The entire state is observable only if Λ is positive

definite. Numerically, Λ can be considered non-positive definite if its condition number is greater than 10^{16} . To test whether Liaison Navigation is feasible, one of the most important steps is verifying that Λ is positive definite without Earth-based tracking. To check for true observability, the *a priori* covariance should not be used in the equation for computing Λ , since P_0 may artificially make the state observable when it should not be. When accumulating Λ during Liaison Navigation, the differences in the state transition matrices of the spacecraft, when one is in a unique orbit, make Λ positive definite. The \tilde{H}_i matrix would tend to make the rows of Λ dependent, since many of the partials used to create \tilde{H}_i are equal in magnitude and opposite in sign, like the partials $\frac{\partial \rho}{\partial x_1} = -\frac{\partial \rho}{\partial x_2}$.

The batch processor is very useful at determining observability, but is awkward at giving an estimate of how the covariance would change when processing observations in real time. By modifying the batch processor so that the observations can be processed sequentially, the resulting filter can be used to show the number of observations and how long it takes for the processor to converge on an orbit solution. The sequential filter used for these tests was the conventional Kalman filter. The Kalman filter requires an *a priori* covariance, P_0 , so it cannot be used to verify total observability, but can show how the covariance changes in real time. Verifying the observability in real time using a sequential processor could be performed using an information filter, but the Kalman filter is used here for simplicity. The Kalman filter works by propagating the state deviation and the covariance at time $k-1$ to the next observation epoch, k , using the “time update” equations

$$\bar{\mathbf{x}}_k = \Phi(t_k, t_{k-1})\hat{\mathbf{x}}_{k-1}, \quad (4.18)$$

$$\text{and } \bar{P}_k = \Phi(t_k, t_{k-1})P_{k-1}\Phi^T(t_k, t_{k-1}). \quad (4.19)$$

The state deviation and covariance are updated with the observations at time k using the

“measurement update” equations

$$K_k = \bar{P}_k \tilde{H}_k^T \left[\tilde{H}_k \bar{P}_k \tilde{H}_k^T + W^{-1} \right]^{-1}, \quad (4.20)$$

$$\hat{\mathbf{x}}_k = \bar{\mathbf{x}}_k + K_k \left[\mathbf{y}_k - \tilde{H}_k \bar{\mathbf{x}}_k \right], \quad (4.21)$$

$$\text{and } P_k = \left[I - K_k \tilde{H}_k \right] \bar{P}_k. \quad (4.22)$$

After creating estimates of the state vector, it is very useful to be able to compare the accuracy of the orbit estimates. In this study, the method used to compare the accuracy of orbit estimates is to propagate the batch covariance matrix over the entire fit span with the relation

$$P_i = \Phi(t_i, t_k) P_k \Phi^T(t_i, t_k). \quad (4.23)$$

Then compute the length of the largest axis of the 3D, 3σ error ellipsoid for the spacecraft, which will be called β_i at time t_i :

$$\beta_i = 3 \max \left(\sqrt{\lambda_j} \right), \quad (4.24)$$

where λ_j for $j = 1, \dots, 3$ are the eigenvalues of $[P_i]_{3 \times 3}$. The average value of β_i over the entire fit span will be called $\bar{\beta}$:

$$\bar{\beta} = \frac{\sum_{i=1}^n \beta_i}{n}, \quad (4.25)$$

where there are n values of β_i in the fit span. If there are multiple satellites, the values of $\bar{\beta}$ for all of the satellites can be averaged to produce a metric called β_{ave} that gives an indication of the overall navigation accuracy for the constellation for those particular conditions.

4.2 Liaison Navigation Orbit Geometry

To evaluate the effectiveness of Liaison Navigation, a group of test orbits was created. These test orbits were designed so that matching various test orbits with each other could simulate a wide range of two-orbit combinations (constellations). At least the first of the orbits in any constellation would have to be a halo orbit, and it will be called “Orbit 1,” while the second orbit could be of any type and will be named “Orbit 2.” The computation of the halo

orbits was performed using the technique explained by Howell (1984) and summarized in Chapter 3.

Families of halo orbits were generated around all three of the collinear Lagrange points in the Earth-Moon system (LL_1 , LL_2 and LL_3). For each family of halo orbits, a certain number were selected as test orbits and ephemeris files were generated for each one. Figures 4.1, 4.2, and 4.3 show the distribution of the initial conditions of the test halo orbits. The halo ephemerides were integrated using a fixed-step, fourth-order Runge-Kutta method with a time step of 2×10^{-4} time units, or about 75 seconds. A set of lunar orbits and Earth orbits were generated for testing as well. Table 4.1 lists each of the test orbits and their characteristics. The orbit elements in the table are defined for the two-body problem, so they were only used to generate the initial conditions for the orbits. The orbits themselves were propagated using the equations of motion for the three-body problem in the same reference frame as the halo orbits. The lunar and Earth ephemerides were integrated using a time step of 5×10^{-5} time units (about 19 seconds). The Earth orbits were meant to be similar to an orbit in the GPS constellation and a geostationary orbit.

The two spacecraft could be placed in the different test orbits in several different ways. When both spacecraft are in the same halo orbit, the constellation is called “Halo₂.” When the spacecraft are in different halo orbits, the constellation is called “Halo-Halo,” and finally, if the spacecraft are in a halo and a lunar or Earth-centered orbit, the constellation is called “Halo-Moon” or “Halo-Earth.”

4.3 Liaison Navigation Test Methods

The first Liaison Navigation tests were conducted using two spacecraft that tracked each other continuously, unless the Earth or the Moon blocked the line of sight vector. Range observations were generated from the ephemeris files every 0.001 time units (≈ 375 seconds).

These observations were used to generate the \tilde{H}_i matrices. The state transition matrices were obtained from the ephemeris files for each orbit. The information matrix, $H^T W H$, was computed

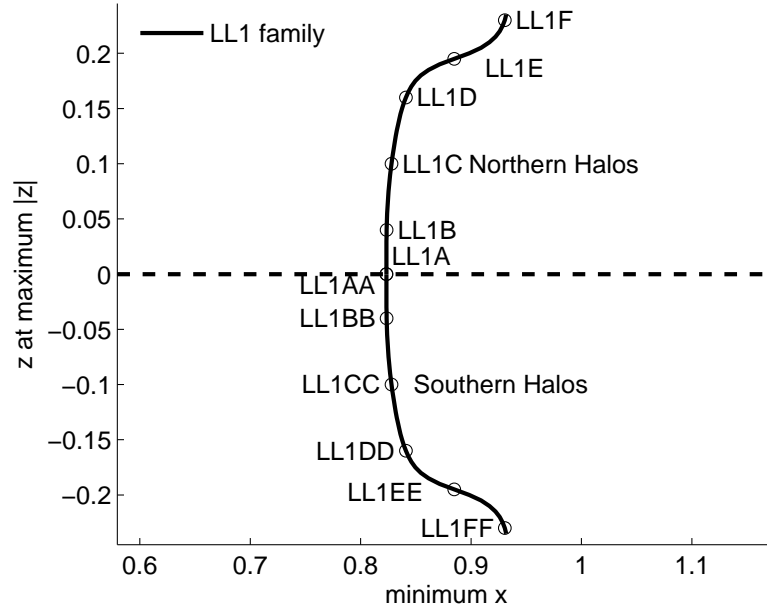


Figure 4.1: Initial conditions and names of LL₁ test orbits.

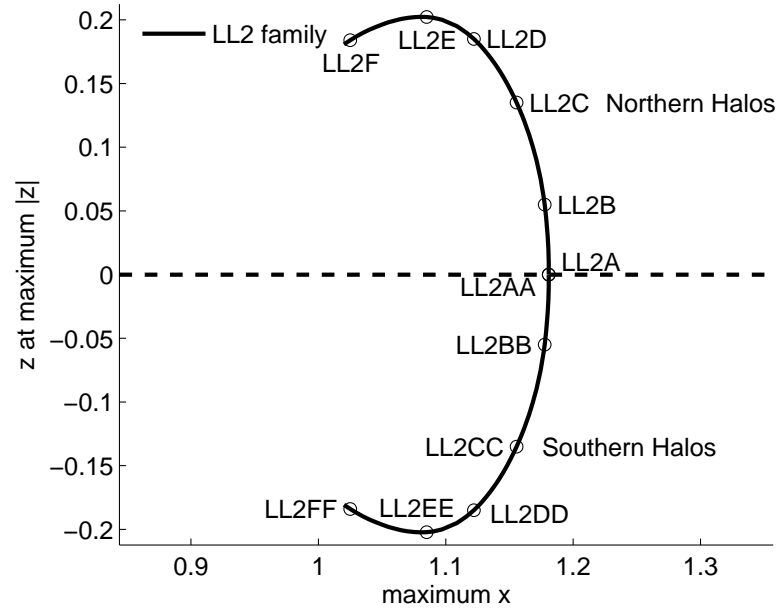


Figure 4.2: Initial conditions and names of LL₂ test orbits.

without computing $H^T W \mathbf{y}$, and the covariance was used to compute navigation error metrics.

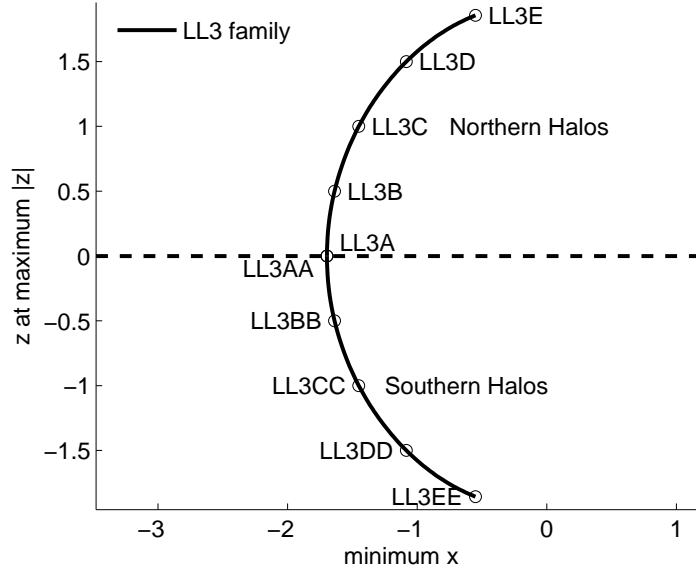
Figure 4.3: Initial conditions and names of LL_3 test orbits.

Table 4.1: PARAMETERS OF THE LUNAR- AND EARTH-CENTERED TEST ORBITS.

Orbit Name	i (deg)	h_p (km)	h_a (km)	Ω (deg)	period (days)
Lunar Orbits					
La	90	100	100	270	0.082
Laa	90	100	100	180	0.082
Lb	90	8262	8262	270	1.039
Lbb	90	8262	8262	180	1.039
Lc	90	100	8262	270	0.473
Lcc	90	100	8262	180	0.473
Lccc	90	100	8262	0	0.473
Ld	0	100	100	0	0.082
Le	0	8262	8262	0	1.039
Lf	0	300	8262	270	0.485
Lff	0	300	8262	180	0.485
Lfff	0	300	8262	0	0.485
Earth Orbits					
Ea	55	circular		0	0.499
Eb	0	circular		0	0.997

Note: For all of the orbits, the true anomaly and argument of perigee were 0 degrees.

The range observations had an added white noise component with a standard deviation of 1 m.

With Halo₂ constellations and various initial phase angles, the Kalman filter was used to

investigate how long it took to converge on a good solution. Figure 4.4 shows a graph of how the covariance decreased over time for one example.

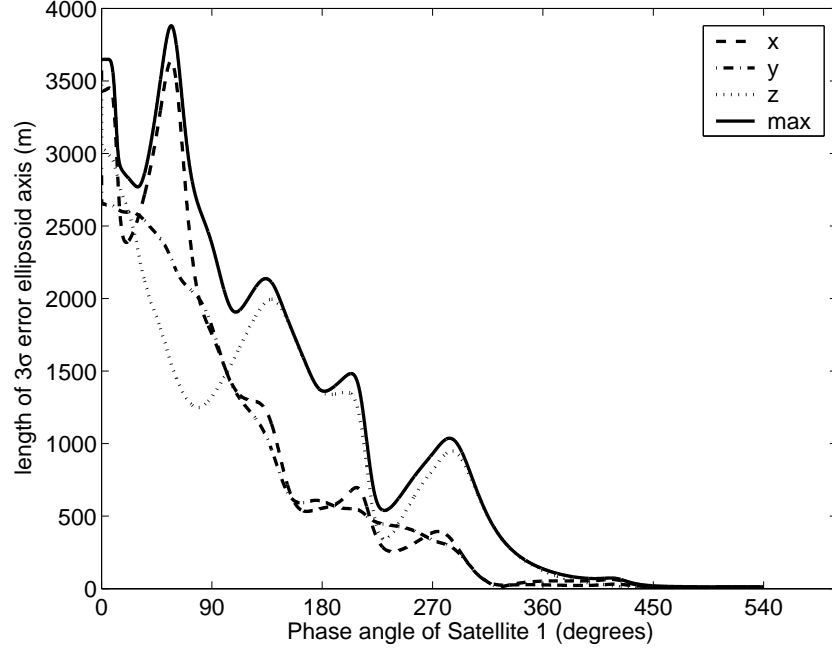


Figure 4.4: Plot of covariance in time showing convergence using the Kalman Filter for a LL1B Halo₂ constellation with $\Delta\tau = 90^\circ$.

After looking at these Kalman filter results for several different halo orbits, it was found that it took about 1.5 orbit periods for the solution to converge, regardless of the halo orbit period. This means that, operationally, the halo orbits with a shorter period will lead to quicker and more accurate navigation. In picking the fit span, it was decided to use 1.5 Orbit 1 periods for all tests involving Halo₂ and Halo-Halo constellations. In Halo-Earth and Halo-Moon constellations, it becomes difficult to converge on the short-period orbit using a batch processor over long integration times. So for these tests, the integration time was shortened to 0.5 Orbit 1 periods.

With both spacecraft starting at different phase angles in a Halo₂ constellation, the difference in phase angle, $\Delta\tau = \tau_2 - \tau_1$, remains constant. Figure 4.5 shows how the orbit determination accuracy varies with $\Delta\tau$.

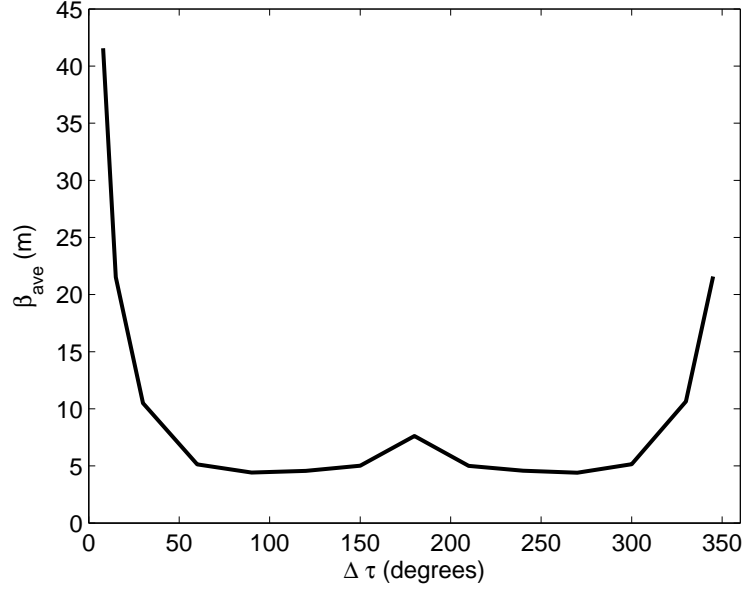


Figure 4.5: Navigation accuracy for two spacecraft on a halo orbit with varying separation in phase angle τ .

The main thing to note from Figure 4.5 is that the orbit determination error goes up as the spacecraft get close to each other at $\tau_2 \approx 0^\circ$ and $\tau_2 \approx 360^\circ$. In fact, the entire state vector becomes unobservable as the spacecraft get too close. While the shape of the error in the middle of the plot varies for different halo orbits, the large error at the edges occurs for every halo orbit. This result is because the magnitude of the relative motion of the spacecraft decreases as the distance between them decreases. Even Halo-Halo constellations can have large error if the spacecraft remain close to each other throughout the fit span. This shows that Liaison Navigation would not work for spacecraft in close formations, but only for spacecraft with large separations.

Due to the interaction between the observation geometry and the geometry of the unstable dynamics described in Chapter 5, the value of the error metric, β_{ave} , varies with the difference in phase angle. Because of this variation, it became necessary to find one representative value of β_{ave} for each combination of orbits. This metric will be called β_{con} and is used to rank the navigation accuracy of the different constellation geometries. In order to find a value of β_{con}

that would be a good approximation of the true constellation navigation accuracy, the value of β_{ave} was computed for the following values of $\Delta\tau$ (in degrees):

$$\left[0 \quad 7.5 \quad 15 \quad 30 \quad 60 \quad 90 \quad 120 \quad 150 \quad 180 \quad 210 \quad 240 \quad 270 \quad 300 \quad 330 \quad 345 \right]$$

It was also found that the value of β_{ave} varied slightly when values of τ_1 and τ_2 themselves were changed while holding $\Delta\tau$ constant. To account for those variations, the value of β_{ave} was computed three different times with all the values of $\Delta\tau$ listed above. τ_1 was set to 0, 90, and 180 degrees for the three different runs. For one value of $\Delta\tau$, the lowest β_{ave} of the three is selected. Of those selected values of β_{ave} , one is chosen to reflect the overall navigation accuracy of the constellation. If the two spacecraft were in orbits of the same period, the lowest of the selected values of β_{ave} is used to represent the accuracy of that constellation. However, if the spacecraft are in orbits of differing periods, it is impossible to maintain a constant $\Delta\tau$. Because of that, the navigation accuracy will vary as the $\Delta\tau$ changes. In that case, the highest β_{ave} is used to represent the error for that constellation. The resulting error in this approximation was judged to be sufficiently small that a good ranking of constellations could be found using β_{con} .

4.4 Constellation Geometry Comparisons

Initial tests of Halo₂ constellations at LL₁ showed that the navigation error was large for the LL1A and LL1AA orbits, which were the closest to the x-y plane. The x-y plane is the only plane in the CRTBP about which the vector field of accelerations and its time derivative are symmetric. Because of this symmetry, libration orbits become more planar as they approach the x-y plane. When both spacecraft are in the same plane, the observations have no out-of-plane component, and thus it is impossible to estimate the out-of-plane position and velocity. To verify this conclusion, several more LL₁ halo orbits were integrated close to the x-y plane and the values of β_{con} were separated into x, y, and z components and plotted in Figure 4.6. For this plot, observations were computed at varying time intervals so that each Halo₂ constellation would produce the same number of observations in 1.5 halo orbit periods. It appears that the

z component of the position is not well resolved until the value of maximum $|z|$ is at least 0.04 nondimensional units.

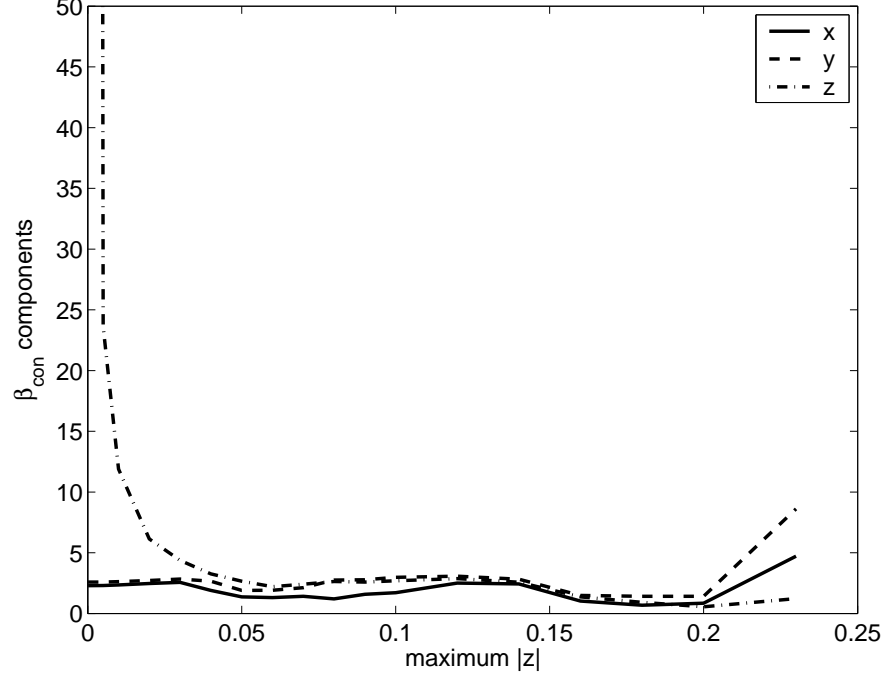


Figure 4.6: β_{con} separated into x, y, and z components for LL₁ Halo₂ constellations.

It can also be seen from Figure 4.6 that the error for LL₁ Halo₂ constellations has local minima around maximum $|z|$ values of 0.06 and 0.2, with the lower minimum occurring around 0.2. It is still not known why the orbits near 0.2 result in better orbit accuracy using Liaison Navigation, but the results from LL₂ Halo₂ constellations follow a similar pattern.

Besides the coplanar cases, Liaison Navigation also resulted in unobservable state parameters when the two spacecraft were in trajectories that were symmetric across the x-y plane, such as LL1B and LL1BB, with the same value of τ . In this configuration, the crosslinks only had a vertical or z component, so the x and y components could not be estimated.

Values of β_{con} were computed for Halo₂ constellations at LL₁, LL₂, and LL₃. β_{con} was also computed for all Halo-Halo constellations in the LL₁, LL₂ and LL₃ test orbits, as well as Halo-Halo constellations with one spacecraft at LL₁ and the other at LL₂. In addition, β_{con}

was computed for all the possible Halo-Moon and Halo-Earth constellations. The results of the simulations showed that the initial position and velocity vectors of both spacecraft were observable for most constellations using Liaison Navigation. Some of the best constellations had values of β_{con} that were less than 1 m, while the worst constellation geometries resulted in an unobservable orbit determination problem. Although not depicted in these results, Liaison Navigation also works for constellations with one spacecraft in Earth orbit and one in lunar orbit. Figures 4.7 through 4.13 show β_{con} for all possible constellations. The shading of the boxes gives a visual indicator of β_{con} , with lighter shading indicating lower values. The value of β_{con} is also printed in each box. For example, in Figure 4.7, the top left box labeled 1228.3 corresponds to the constellation where Orbit 1 is LL1A and Orbit 2 is LL1A. The bottom left box labeled 2.9 corresponds to the constellation with LL1FF for Orbit 1 and LL1A for Orbit 2. Note that the boxes are blank in the top right corners of Figures 4.7, 4.8, and 4.9 due to symmetry in the results.

		LL1A	LL1B	LL1C	LL1D	LL1E	LL1F		
Orbit 1	LL1A	1228.3						LL1A	
	LL1B	8.7	4.6					LL1B	
	LL1C	9.6	19.9	3.9				LL1C	
	LL1D	4.6	19.9	14.4	2.3			LL1D	
	LL1E	4.4	5.4	7.4	4.3	1.9		LL1E	
	LL1F	2.9	3.4	4.1	4.1	6.9	12.7	LL1F	
	LL1AA	1347.4	8.8	9.0	3.7	2.8	1.4	LL1AA	
	LL1BB	8.7	9.9	5.8	3.5	1.4	1.0	LL1BB	
	LL1CC	9.3	5.4	1.9	1.1	0.8	0.8	LL1CC	
	LL1DD	4.6	5.0	2.4	1.0	1.1	0.9	LL1DD	
	LL1EE	4.4	2.5	1.8	3.4	1.1	4.0	LL1EE	
	LL1FF	2.9	2.0	2.5	2.8	4.5	22.7	LL1FF	
		LL1A	LL1B	LL1C	LL1D	LL1E	LL1F		
		Orbit 2							

Figure 4.7: Plot of β_{con} (m) for Halo₂ and Halo-Halo constellations at LL₁.

		LL2A	LL2B	LL2C	LL2D	LL2E	LL2F		
Orbit 1	LL2A	1134.7						LL2A	
	LL2B	6.3	1.8					LL2B	
	LL2C	4.4	5.5	3.0				LL2C	
	LL2D	4.1	7.8	5.3	1.7			LL2D	
	LL2E	5.3	6.1	5.9	4.7	1.3		LL2E	
	LL2F	7.0	11.4	9.4	11.3	13.2	3.0	LL2F	
	LL2AA	4690.1	5.5	3.4	1.4	1.4	0.6	LL2AA	
	LL2BB	6.3	1.4	1.9	1.2	1.0	0.4	LL2BB	
	LL2CC	4.4	2.8	1.2	1.5	1.1	0.3	LL2CC	
	LL2DD	4.1	2.3	2.0	0.9	1.6	0.6	LL2DD	
	LL2EE	5.3	3.2	2.2	2.6	1.0	1.9	LL2EE	
	LL2FF	6.9	6.1	4.9	6.4	9.2	2.8	LL2FF	
		LL2A	LL2B	LL2C	LL2D	LL2E	LL2F		
		Orbit 2							

Figure 4.8: Plot of β_{con} (m) for Halo₂ and Halo-Halo constellations at LL₂.

		LL3A	LL3B	LL3C	LL3D	LL3E		
Orbit 1	LL3A	21879.1					LL3A	
	LL3B	206.0	56.3				LL3B	
	LL3C	68.4	117.4	37.6			LL3C	
	LL3D	44.8	53.1	79.6	24.0		LL3D	
	LL3E	46.8	43.6	63.5	43.9	17.2	LL3E	
	LL3AA	84062.0	213.3	64.3	47.5	40.7	LL3AA	
	LL3BB	205.8	28.2	78.7	55.4	45.6	LL3BB	
	LL3CC	68.4	91.2	17.1	65.6	45.3	LL3CC	
	LL3DD	44.8	55.7	72.2	14.3	76.1	LL3DD	
	LL3EE	46.8	49.5	56.1	86.8	16.5	LL3EE	
		LL3A	LL3B	LL3C	LL3D	LL3E		
		Orbit 2						

Figure 4.9: Plot of β_{con} (m) for Halo₂ and Halo-Halo constellations at LL₃.

		LL1a	LL1b	LL1c	LL1d	LL1e	LL1f		
Orbit 1	LL2a	6677.4	7.8	5.9	3.2	1.1	1.1	LL2a	
	LL2b	13.8	10.3	5.0	2.4	0.8	0.9	LL2b	
	LL2c	5.9	3.3	3.6	2.3	0.9	0.6	LL2c	
	LL2d	4.2	3.0	2.8	3.3	1.0	0.8	LL2d	
	LL2e	5.2	3.3	2.0	1.5	2.8	2.0	LL2e	
	LL2f	5.5	7.0	5.9	7.3	10.0	8.8	LL2f	
	LL2aa	6278.9	6.7	6.0	3.2	1.1	1.1	LL2aa	
	LL2bb	11.4	9.5	5.4	3.7	1.0	0.9	LL2bb	
	LL2cc	5.3	6.2	8.1	4.1	1.2	0.7	LL2cc	
	LL2dd	4.3	7.5	4.6	8.9	1.4	1.2	LL2dd	
	LL2ee	5.2	4.2	2.3	2.6	3.8	2.6	LL2ee	
	LL2ff	5.5	4.5	3.6	5.0	4.7	11.7	LL2ff	
		LL1a	LL1b	LL1c	LL1d	LL1e	LL1f		
Orbit 2									

Figure 4.10: Plot of β_{con} (m) for Halo-Halo constellations with one spacecraft at LL_1 and one at LL_2 .

		LL1A	LL1B	LL1C	LL1D	LL1E	LL1F		
Orbit 2	La	105	11	12	18	68	255	La	
	Laa	107	11	12	18	63	230	Laa	
	Lb	11	8	6	7	42	219	Lb	
	Lbb	9	6	5	7	44	199	Lbb	
	Lc	13	5	5	7	35	141	Lc	
	Lcc	13	5	5	8	39	108	Lcc	
	Lccc	12	4	4	7	42	164	Lccc	
	Ld	3932	13	10	15	60	167	Ld	
	Le	1568	5	4	5	30	106	Le	
	Lf	2143	8	5	7	25	73	Lf	
	Lff	2165	7	5	7	26	79	Lff	
	Lfff	1902	6	5	7	26	104	Lfff	
	Ea	11	7	8	5	7	23	Ea	
	Eb	3807	13	10	6	9	49	Eb	
		LL1A	LL1B	LL1C	LL1D	LL1E	LL1F		
		Orbit 1							

Figure 4.11: Plot of β_{con} (m) for Halo-Earth and Halo-Moon constellations at LL_1 .

		LL2A	LL2B	LL2C	LL2D	LL2E	LL2F		
Orbit 2	La	102	12	9	13	35	205	La	
	Laa	117	12	9	13	34	314	Laa	
	Lb	12	7	7	8	20	157	Lb	
	Lbb	10	6	7	10	24	184	Lbb	
	Lc	13	5	5	8	24	121	Lc	
	Lcc	16	5	5	8	26	171	Lcc	
	Lccc	16	5	5	8	22	166	Lccc	
	Ld	5380	12	9	12	31	147	Ld	
	Le	2393	5	4	7	18	90	Le	
	Lf	2751	6	5	9	18	82	Lf	
	Lff	2830	6	6	9	18	93	Lff	
	Lfff	3110	7	5	9	19	83	Lfff	
	Ea	15	6	5	4	4	11	Ea	
	Eb	8462	18	7	5	6	14	Eb	
			LL2A	LL2B	LL2C	LL2D	LL2E	LL2F	
		Orbit 1							

Figure 4.12: Plot of β_{con} (m) for Halo-Earth and Halo-Moon constellations at LL₂.

		LL3A	LL3B	LL3C	LL3D	LL3E			
Orbit 2	La	380	5	3	3	6	La		
	Laa	729	5	3	3	7	Laa		
	Lb	63	4	3	3	6	Lb		
	Lbb	137	4	2	2	6	Lbb		
	Lc	119	4	3	3	6	Lc		
	Lcc	195	4	3	3	6	Lcc		
	Lccc	195	4	3	3	6	Lccc		
	Ld	3140	6	3	3	7	Ld		
	Le	2305	5	2	3	5	Le		
	Lf	2638	5	3	3	7	Lf		
	Lff	2502	5	3	3	6	Lff		
	Lfff	2541	5	3	3	6	Lfff		
Ea	1682	429	319	203	160	Ea			
Eb	169538	344	188	182	146	Eb			
		LL3A	LL3B	LL3C	LL3D	LL3E			
		Orbit 1							

Figure 4.13: Plot of β_{con} (m) for Halo-Earth and Halo-Moon constellations at LL₃.

β_{con} for constellations including spacecraft in halo orbits with low vertical components, such as LL1A or LL1AA, were the worst. The results generally get better as the two halos move farther from the plane. This pattern was repeated for the LL₂ and LL₃ halo orbits also.

The length of the halo orbit periods generally decreases from A to F for all of the halo families. The best results in Figures 4.7, 4.8 and 4.10 were obtained when Orbit 1 was a long period halo and Orbit 2 was a short period halo. This was because the spacecraft in Orbit 2 did much more than 1.5 orbits in the time it took the spacecraft in Orbit 1 to do its required 1.5 orbits. The more revolutions a spacecraft can perform within the fit span, the more geometrically diverse observations can be obtained and the error is reduced.

The LL₃ constellations featured in Figure 4.9 resulted in orbit determination errors that were around 10 times larger than the LL₁ and LL₂ constellations. This seems to agree with Figure 2.7 which showed that the strength of the asymmetry of the third-body perturbation was weak at LL₃. In addition, the LL₃ Halo-Earth constellations in Figure 4.13 had very poor observability. This is because most of the orbit dynamics at LL₃ are due to the Earth's gravity, not the Moon's.

For the Halo-Moon constellations in Figures 4.11 and 4.12, the ones containing the lunar orbits La, Laa, or Ld seem to have conspicuously worse results. These are the circular, 100 km altitude Lunar orbits. Because they are so low, more of observations are blocked by the Moon. While most Halo-Moon constellations had about 0-10% of the observations blocked by the Moon, the low-altitude constellations had between 25 and 40% of the observations blocked.

4.5 Orbit Determination Parameter Comparisons

Out of the many different constellation geometries, 18 were selected for further study and called “baseline” orbits. Table 4.2 shows the 18 baseline orbit constellations and the resulting values of β_{con} using the baseline test settings as outlined previously. These baseline orbits were used in different test cases to find how the covariance of the orbit estimates change when certain parameters are varied. For each test case, one or two settings were changed, and the rest of the

settings were the same as in the preceding analysis (the baseline settings).

Table 4.2: DESCRIPTION OF BASELINE ORBITS.

Baseline orbit number	Orbit 1	Orbit 2	Baseline Value of β_{con} (m)	Constellation Type
1	LL1b	LL1b	4.6	Halo ₂
2	LL1dd	LL1d	1.0	Halo-Halo
3	LL1e	LL1b	5.4	Halo-Halo
4	LL1dd	LL1f	0.9	Halo-Halo
5	LL2c	LL2c	3.0	Halo ₂
6	LL2b	LL2b	1.8	Halo ₂
7	LL2cc	LL2f	0.3	Halo-Halo
8	LL2d	LL2b	7.8	Halo-Halo
9	LL3e	LL3e	17.2	Halo ₂
10	LL3c	LL3a	68.4	Halo-Halo
11	LL2c	LL1f	0.6	Halo-Halo
12	LL2b	LL1c	5.0	Halo-Halo
13	LL1c	Lcc	4.9	Halo-Moon
14	LL1e	Lb	42.2	Halo-Moon
15	LL2c	Le	3.9	Halo-Moon
16	LL2d	Laa	13.3	Halo-Moon
17	LL3c	Lbb	2.5	Halo-Moon
18	LL3e	Lf	6.7	Halo-Moon

Case 1: The same time period was used for all constellations: 4 nondimensional time units or 17.4 days. In general, constellations with shorter orbit periods did better. This is because observations from all possible vantage points are obtained sooner. As expected, the Halo-Moon orbits faired much better with this longer fit span. This shows that the Halo-Moon constellations are able to recover orbit information faster than the Halo₂ or Halo-Halo constellations. However, due to uncertainties in the lunar gravity field, orbit integration times would probably have to be shorter when one spacecraft is in lunar orbit. Also, the errors in the lunar gravity field were not modeled in these simulations. These would offset some of the advantages for Halo-Moon constellations.

Case 2: The data rate was changed so that observations were taken less often. A measurement was computed every 0.002 nondimensional time units (≈ 750 seconds) instead of every 0.001 time units. The resulting error increased consistently for all baseline orbits by an average

of 41%.

Case 3: The effect of a sinusoidal error in the observations was computed using the consider covariance technique outlined in Chapter 6 of Tapley et al. (2004). The amplitude and the frequency of the sine wave were the consider parameters, with the nominal amplitude modeled as 0.5 m and the period as the shorter of the two orbit periods. The standard deviations of the error in those parameters was 0.5 m for the amplitude and 1/4 period for the frequency. The phase of the sinusoid was assumed to be zero at t_0 . This increased the values of β_{con} by an average of 600%.

Case 4: The effect of an error in the force model on the covariance was computed using the consider covariance technique. A constant error in the acceleration for the x, y, and z directions was modeled as three consider parameters for each satellite. The standard deviation for the error in the accelerations was set at $1 \times 10^{-8} \text{ m/s}^2$. The resulting RSS magnitude of the 1σ , 3D unknown acceleration vector would be about 26% of the magnitude of the acceleration due to solar radiation pressure for a 1000 kg spacecraft with a 10 m^2 cross section and reflectivity of 1.5. These errors in acceleration increased the values of β_{con} quite dramatically for most orbits. However, as a general rule, the Halo-Moon constellations fared better.

Case 5: An error in the range measurements was introduced in the form of a range bias error with a standard deviation of 5 m. The range bias was added to the state to be estimated along with the positions and velocities of both spacecraft. The results showed that it is possible to estimate the range bias using only SST. However, the overall error in the position increased. There was an average increase of 53% in the value of β_{con} .

Case 6: The range bias was estimated as well as including errors in the force model in the form of consider covariance parameters. The resulting increases in β_{con} varied widely. While some values of β_{con} increased by many thousands of percentage points, constellation 14 had an increase of only 0.3% in the error metric.

Case 7: Range rate measurements were used instead of range. The noise on the range rate observations was modeled as Gaussian with a standard deviation of 0.5 mm/s. The orbit

estimate errors increased for all of the baseline constellations by an average of about 2900%, confirming that Doppler would indeed be a weaker data type.

Case 8: Because of the large link distances involved, it is probable that highly directional antennas would need to be used when generating the SST range measurements. Unless the spacecraft have more than one high gain antenna, they would not be able to continuously track each other and communicate with other entities simultaneously. Because of that, observations were taken in two-hour blocks separated by two-hour periods without any measurements to simulate link periods when the spacecraft were communicating with landers, tracking user spacecraft, or communicating with ground controllers. The resulting increase in β_{con} averaged 46% for all the baseline constellations.

Case 9: This run was meant to simulate as close as possible the orbit accuracy attainable in a real operations environment. One final run was performed using the LL2c and Lc orbits. This was one of the better constellations, although it wasn't the best. In this run, the interval between observations was reduced to 0.0001 time units (≈ 37.5 seconds), which required a much larger ephemeris file. Consider covariance analysis for unknown accelerations was performed as before with the range bias included in the estimated state vector. Two-hour communication periods were separated by two-hour periods with no observations. The standard deviation on the range measurement noise was set to 1 m, and range rate measurements were not used. A range of phase angle values was used for satellites 1 and 2, and the worst-case β_{con} was 9.79 m. For that case, the maximum range between the spacecraft was about 86,000 km. The β_{ave} for the satellite in the halo was 17.4 m and 2.4 m for the satellite in lunar orbit. The number of observations for 0.5 LL2c orbit periods (≈ 3.6 days) was 3805, with 384 observations blocked by the Moon.

4.6 Monte Carlo Analysis of the Covariance

To verify that the covariance analysis was correct, a Monte Carlo analysis was conducted using the LL2c-Lc Halo-Moon constellation. The spacecraft in LL2c was placed at $\tau = 0^\circ$, and

the spacecraft in Lc was placed at $\nu = 90^\circ$ (true anomaly). Observations were processed every ≈ 375 seconds with 2 hour blackout periods. A range bias was added to the state vector and the fit span was 0.5 LL2c orbit periods long. The satellite states were perturbed by normally distributed random numbers with a 1σ of 1×10^{-6} (about 384 m for position and 1 mm/s for velocity). The range bias was perturbed with a normally distributed random number with a 1σ of 5 m. After converging on a solution, the estimated state was compared to the true state. This was done 1000 times. If the covariance matrix is realistic, the orbit error will be inside the 3D, 2σ error ellipsoid for 73.9% of the runs. To find if the error is inside the 2σ error ellipsoid, the size of the error ellipsoid that intersects the orbit error vector is computed for each satellite. The size of the ellipsoid, L , has units of standard deviations (σ) and is computed as shown in Tapley et al. (2004) section 4.16.

$$L_i^2 = \mathbf{x}_i^T P_i^{-1} \mathbf{x}_i \quad (4.26)$$

\mathbf{x}_i is the error vector for spacecraft i , or the true state subtracted from the state estimate. P_i is the 3×3 position covariance matrix for spacecraft i . For the LL2c-Lc constellation, 74% of the values of L_1 and 73% of the values of L_2 were below 2σ . For the range bias covariance to be accurate, the range bias error should be less than 2σ for 95.4% of the runs. The range bias error was within 2σ for 98% of the range bias errors.

The LL1c-LL1d Halo-Halo constellation was also tested in the same way using 1000 runs. The spacecraft in LL1c was placed at $\tau = 0^\circ$, and the spacecraft in LL1d was placed at $\tau = 90^\circ$. Observations were processed every ≈ 375 seconds with 2 hour blackout periods. A range bias was added to the state vector and the fit span was 1.5 LL1c orbit periods long. The satellite states were perturbed by normally distributed random numbers with a 1σ of 1×10^{-7} (about 38 m for position and 0.1 mm/s for velocity). The range bias was perturbed with a normally distributed random number with a 1σ of 5 m. For this constellation, 72% of the values of L_1 , 71% of the values of L_2 , and 97% of the range bias errors were below 2σ . For the constellation LL2c-Lc constellation, the covariance appears to be accurate, but optimistic by a few percentage points for the constellation LL1c-LL1d. This is probably because the accuracy of the Halo-Halo orbit

estimates was worse than for the Halo-Moon orbits, and the dynamics are so highly nonlinear in halo orbits that the linear approximation used to generate the state transition matrix results in a small error.

Based on the simulations in the Earth-Moon CRTBP, Liaison Navigation in lunar halo orbits not only appears possible, but also has the potential to be highly accurate. Remember that the β_{ave} and β_{con} metrics are based on the 3σ error ellipsoid. Based on these simulations, it seems plausible that an actual application of Liaison Navigation in lunar halo orbits would be able to achieve a 1σ orbit accuracy around 10 m. If so, the improved orbit accuracy for spacecraft in libration orbits provided by Liaison Navigation would lead to a decrease in the ΔV needed for stationkeeping, since more accurate knowledge of the orbit leads to smaller stationkeeping maneuvers (Gómez et al., 1998).

When selecting halo constellation geometries for use in Liaison Navigation, orbit determination accuracy is improved if the following conditions are met.

- Spacecraft should have relatively large separation distances.
- Not all the spacecraft can remain in the same plane for their entire trajectories.
- Libration orbits with shorter periods lead to quicker convergence.

Simulations in different three-body systems and with perturbations to the CRTBP will be addressed in Chapters 6, 7, and 8.

Chapter 5

Observability and Geometry

5.1 Observability

In Chapter 2, the success of Liaison Navigation depended on finding whether SST observations alone could be used to observe the states of all participating spacecraft. The test for observability was the condition number of the information matrix, $\text{cond}(\Lambda)$. With machine precision in mind, $\text{cond}(\Lambda)$ had to be less than 10^{16} for the problem to be observable. Chapter 2 explained intuitively why Liaison Navigation could not be used in the two-body problem. In that case, the absolute orientation of the orbit planes was not observable. To verify this numerically, a reasonable approach would be to plot a position error ellipsoid for a spacecraft and observe the orientation of the largest uncertainty. If the largest uncertainty were perpendicular to the radial direction from the primary body, that would seem to verify that it was indeed the absolute orientation that was not observable. When Λ is not positive definite, it is not possible to invert it to generate the covariance, P . In that situation, Λ itself must be used instead of examining the covariance.

The eigenvalues of the information matrix can be interpreted inversely from the way the eigenvalues of the covariance are interpreted. Where the largest eigenvalue of the covariance matrix represented the largest uncertainty, the largest eigenvalue of the information matrix represents the least uncertainty or the most information. When the observations have provided no information in a certain direction, the information matrix will have an eigenvalue of zero

with a corresponding eigenvector in that same direction. These eigenvectors with an eigenvalue of zero show the direction of the unobservability.

5.2 Observation Effectiveness

It was found in Chapter 4 that the Liaison orbit determination accuracy for two spacecraft depended on $\Delta\tau$, or the difference in halo orbit phase angle $\tau_2 - \tau_1$. τ is defined in Chapter 3. It was also found that the absolute values of τ_1 and τ_2 at the beginning of the fit span affected the results as well. An important question is, why do these different constellation geometries affect the orbit determination accuracy so much?

One way to find insight into this problem is to look at the effectiveness of each individual observation. The information matrix was computed from Equation 4.14:

$$\Lambda = \sum_{i=1}^{\ell} H_i^T W H_i.$$

The effectiveness of observation i , $\delta\Lambda(t_i)$, can be written (Scheeres, 2001)

$$\delta\Lambda(t_i) = H_i^T W H_i. \quad (5.1)$$

$\delta\Lambda$ is like an information matrix for the observation at t_i alone. To find the amount of information obtained for the position of a particular spacecraft, the 3×3 position portion of $\delta\Lambda$ corresponding to spacecraft j can be extracted and called $\delta\Lambda_j$. A single measure of the effectiveness of $\delta\Lambda_j$ is found by computing the square root of the maximum eigenvalue of $\delta\Lambda_j$, or $\sqrt{\max \text{eig}(\delta\Lambda_j)}$.

Plotting $\sqrt{\max \text{eig}(\delta\Lambda_j)}$ for unstable halo orbits and two Keplerian orbits show interesting differences, as can be seen in Figures 5.1 and 5.2. The two-body orbits used to create Figure 5.1 were lunar orbits with a semimajor axis of 10,000 km. One was equatorial with an eccentricity of about 0.001 and the other was polar with an eccentricity of about 0.08.

In general, the effectiveness of the halo orbit observations increase exponentially, but there are several dips in effectiveness where almost no information is obtained. Both spacecraft 1 and 2 have two large dips, or “blackout periods” where the effectiveness decreases up to three

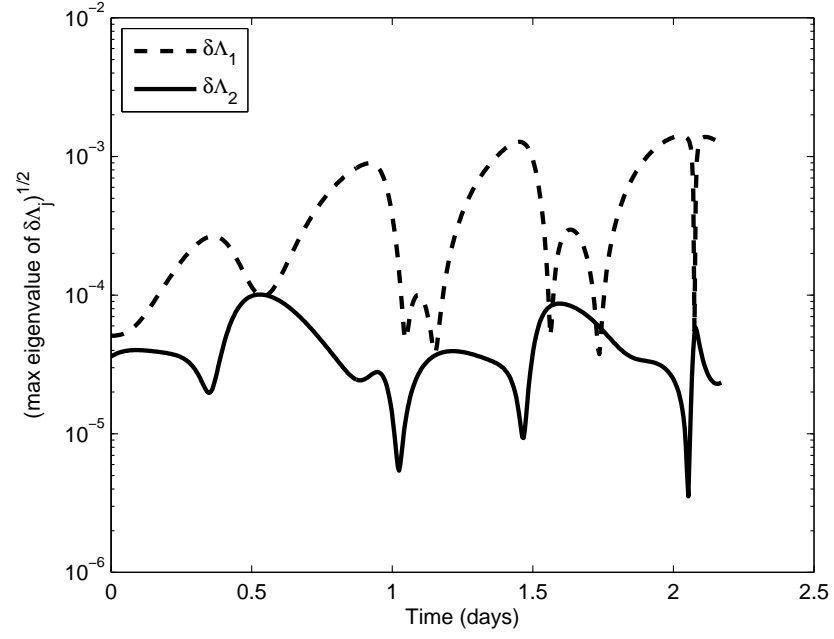


Figure 5.1: Observation effectiveness for a Lb-Le Moon-Moon constellation.

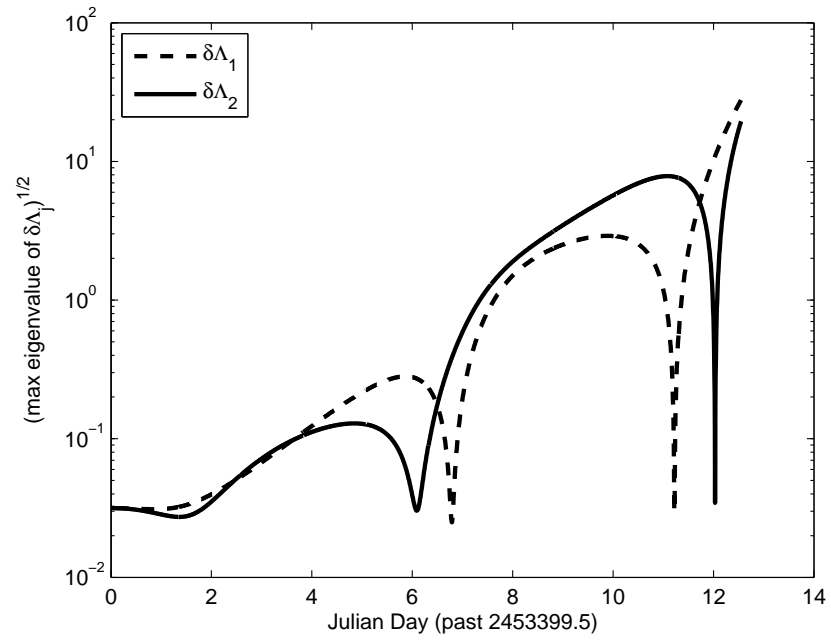


Figure 5.2: Observation effectiveness for a LL1B Halo₂ constellation.

orders of magnitude. On the other hand, the Keplerian orbit shows a much shallower trend for the increase in effectiveness over time and the dips in effectiveness are much smaller than for the halo orbit.

$\delta\Lambda_j$ also contains information describing the effectiveness in estimating the position of spacecraft j in the x, y, and z components separately. For the x component of spacecraft j , this is done by taking the square root of the first value on the diagonal $\delta\Lambda_j$. The y component would be the square root of the second value on the diagonal $\delta\Lambda_j$, and so on. Figures 5.3 and 5.4 show $\delta\Lambda_1$ split into x, y, and z components.

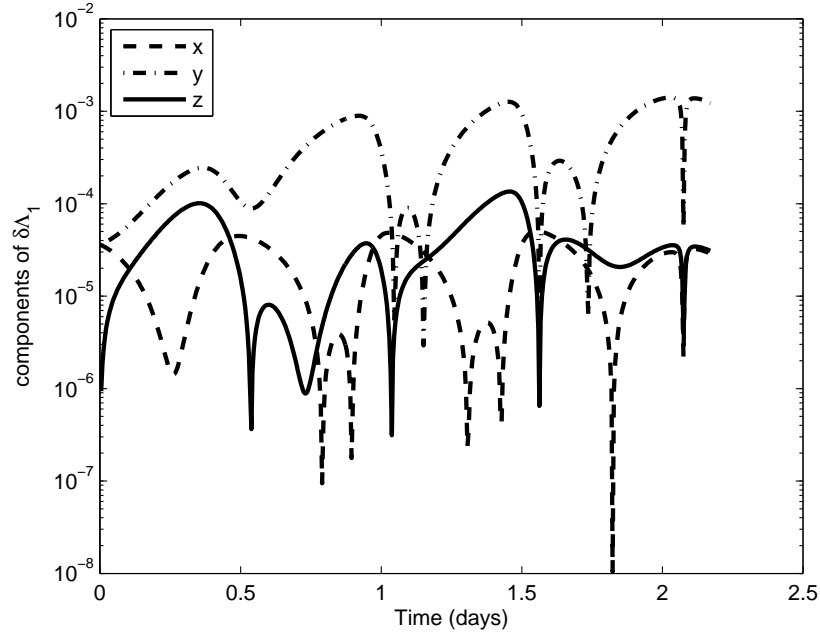


Figure 5.3: Components of observation effectiveness for Spacecraft 1 in the Lb-Le Moon-Moon constellation.

While the x, y, and z components of $\delta\Lambda_1$ for a Keplerian orbit will all dip to lower values, they usually do not dip together, meaning that while no information is obtained for the z component of position for a spacecraft, there is still information obtained for the x and y components, and the observation is not a total waste. However, notice in Figure 5.4 that the x, y, and z components of $\delta\Lambda_1$ dip in rapid succession at seven days past the epoch and nearly

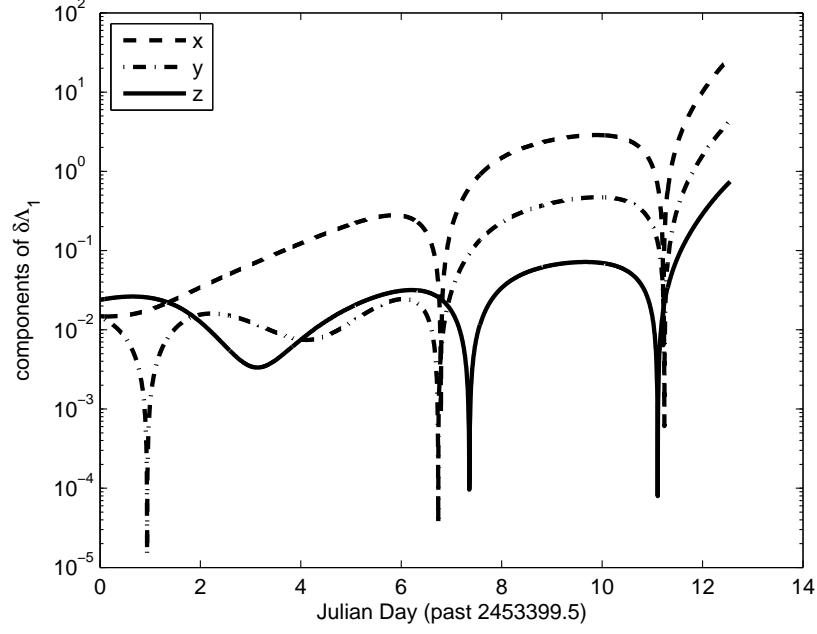


Figure 5.4: Components of observation effectiveness for Spacecraft 1 in the LL1B Halo₂ constellation.

simultaneously at 11 days past epoch. When all three plots dip simultaneously, that means no position information is obtained from that observation at all during the blackout period.

To see why that is, $\delta\Lambda$ must be dissected into its various parts. Using Equation 4.9, the component parts of $\delta\Lambda$ are

$$\delta\Lambda(t_i) = \Phi^T(t_i, t_k) \tilde{H}_i^T W \tilde{H}_i \Phi(t_i, t_k) \quad (5.2)$$

Thus, $\delta\Lambda$ is influenced by the observation geometry, \tilde{H} , and the state transition matrix, Φ , and the observation noise W . W does not change and is independent from the orbit type, so it will not be discussed. Scheeres et al. (2001) explains the relationship between \tilde{H} and Φ and most of the following discussion follows from that paper. First it will be necessary to review the properties of \tilde{H} and Φ .

Φ governs how the uncertainty in an orbit state changes over time. This can be seen from Equation 4.23, which shows how a covariance matrix at time t_k changes upon arriving at

time t_i .

$$P_i = \Phi(t_i, t_k) P_k \Phi^T(t_i, t_k)$$

To look at how the uncertainty changes in a generic way, P_k can be set to the identity matrix and the equation becomes

$$P_i = \Phi(t_i, t_k) \Phi^T(t_i, t_k). \quad (5.3)$$

$\Phi\Phi^T$ takes the form of a covariance matrix and shows how uncertainty changes in time. The 3×3 position portion of $\Phi\Phi^T$ can be plotted as an error ellipsoid to see how the position uncertainty propagates. If an axis of the $\Phi\Phi^T$ error ellipsoid becomes larger than unity, the uncertainty is increasing in that direction. Likewise, if an axis of the ellipsoid becomes less than unity, uncertainty along that axis is getting smaller. According to Scheeres et al. (2001), the error ellipsoid of an orbit in the two-body problem or a Keplerian orbit will expand in the alongtrack direction as time progresses. However, for an unstable orbit like a halo orbit, the stability characteristics of the orbit create a more significant affect than a downtrack error.

When the state transition matrix, Φ , of a periodic orbit like a halo orbit is propagated for one period, it can be called a Monodromy matrix. The eigenvalues of the monodromy matrix, λ_i , have special properties. Two of the eigenvalues will be equal to one. One corresponds to movement along the orbit, and the other corresponds to movement along a surface of constant Jacobi energy. Two will be oscillatory and are complex conjugates with a modulus of one (Howell et al., 1997). These correspond to nearby quasi-periodic orbits. The last two correspond to exponential expansion and contraction of the uncertainty. If λ_i is one of these two exponential eigenvalues, then the other will be $1/\lambda_i$. The eigenvalue greater than one corresponds to the unstable manifold, and its eigenvector describes the direction along which a perturbation will increase exponentially. The stable manifold corresponds to the eigenvalue less than one, and its eigenvector describes the direction along which a perturbation will decrease exponentially. In other words, a spacecraft perturbed along the stable manifold will return to the nominal periodic orbit, but one perturbed along the unstable manifold will exponentially depart the

periodic orbit.

When the state transition matrix has been propagated through time intervals other than one period, local stable and unstable eigenvalues exist, although the eigenvalues equal to unity do not. The local unstable and stable manifolds dominate the dynamics for a halo orbit error ellipsoid. Instead of increasing uncertainty in the alongtrack direction, the largest increase in uncertainty occurs in the direction of the local unstable manifold. On the other hand, the uncertainty along the local stable manifold decreases. The result is that the $\Phi\Phi^T$ error ellipsoid becomes increasingly long and thin.

A way of verifying this difference between Keplerian orbits and halo orbits is to plot the aspect ratio of the $\Phi\Phi^T$ position error ellipsoids. The aspect ratio is the length of the largest axis divided by the length of the shortest axis. Figure 5.5 shows the aspect ratios for both a Halo orbit and a Keplerian orbit over two orbit periods.

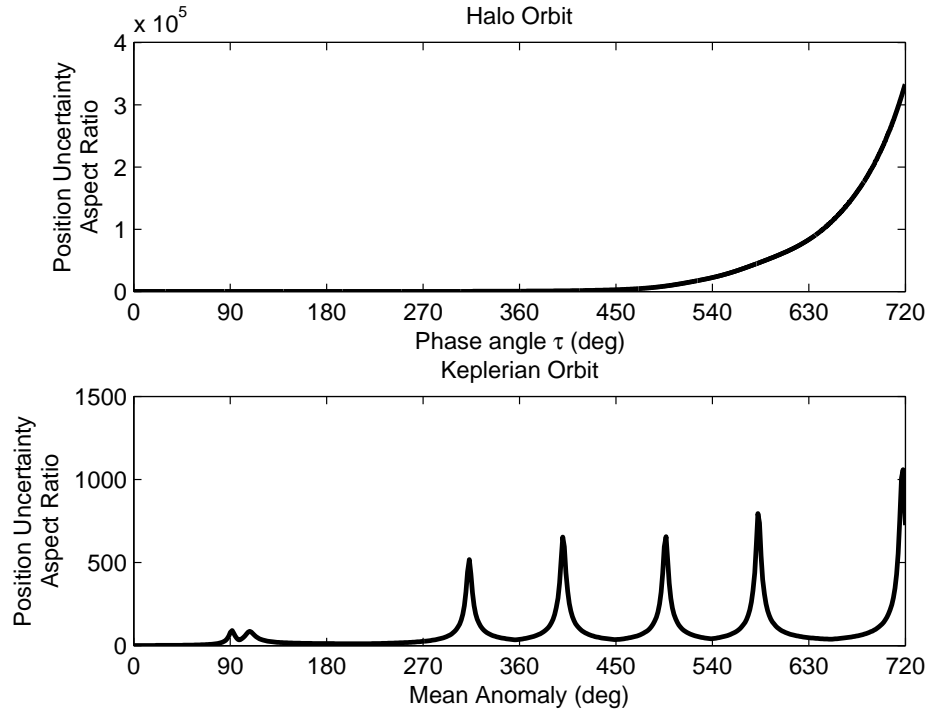


Figure 5.5: Position error ellipsoid aspect ratios for a halo orbit and a Keplerian orbit.

The aspect ratio of the halo orbit error ellipsoid increases exponentially. The aspect ratio for the Keplerian orbit also increases, but it oscillates so that the aspect ratio recedes to low levels periodically.

The reason that the shape of the $\Phi\Phi^T$ error ellipsoids is important is that an observation that senses along the large axis of the uncertainty is more effective. If a small perturbation propagates into a large uncertainty along a certain vector, sensing along that vector will enable a magnified perception of the initial state. On the other hand, a small perturbation in the initial state along the direction of the stable manifold is reduced, so sensing along this direction gives less information about the initial state. Figure 5.6 shows this graphically.

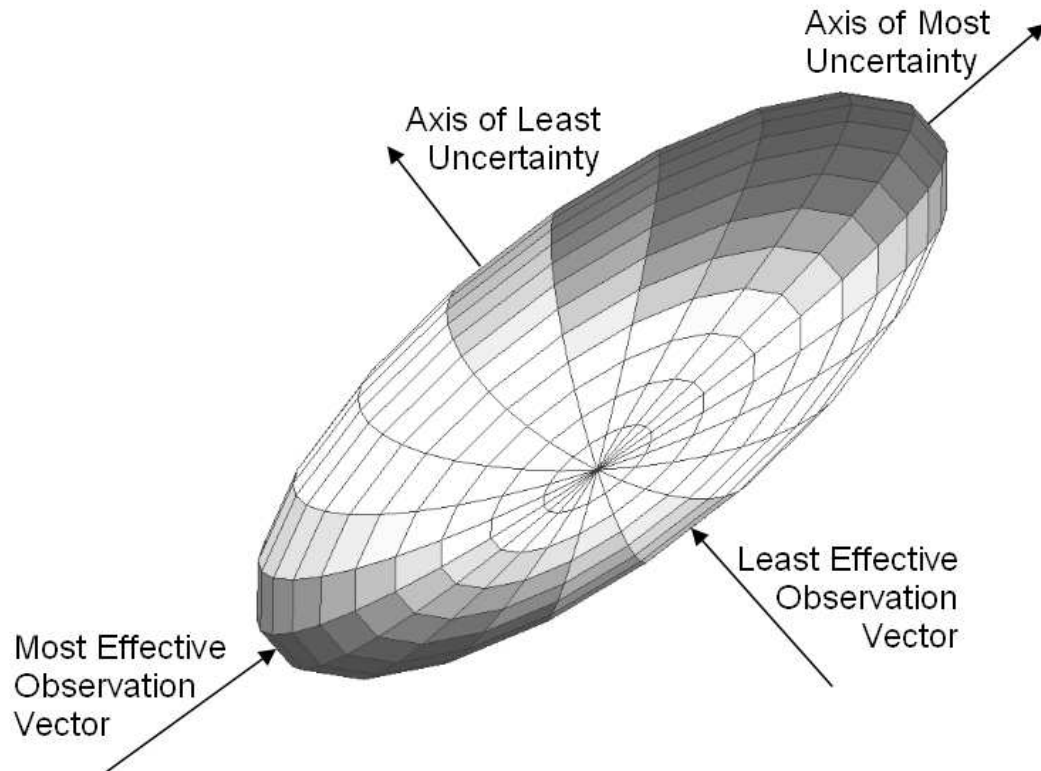


Figure 5.6: Relationship between the shape of the uncertainty ellipsoid and the effectiveness of an observation vector.

Plotting the angle between the largest axis of the position error ellipsoid and the sensing direction shows that the dips in observation effectiveness coincide with moments when the

sensing direction is perpendicular to the local unstable manifold. This can be seen in Figure 5.7. The observation effectiveness has a blackout when the angle between the local unstable manifold and the sensing direction becomes perpendicular.

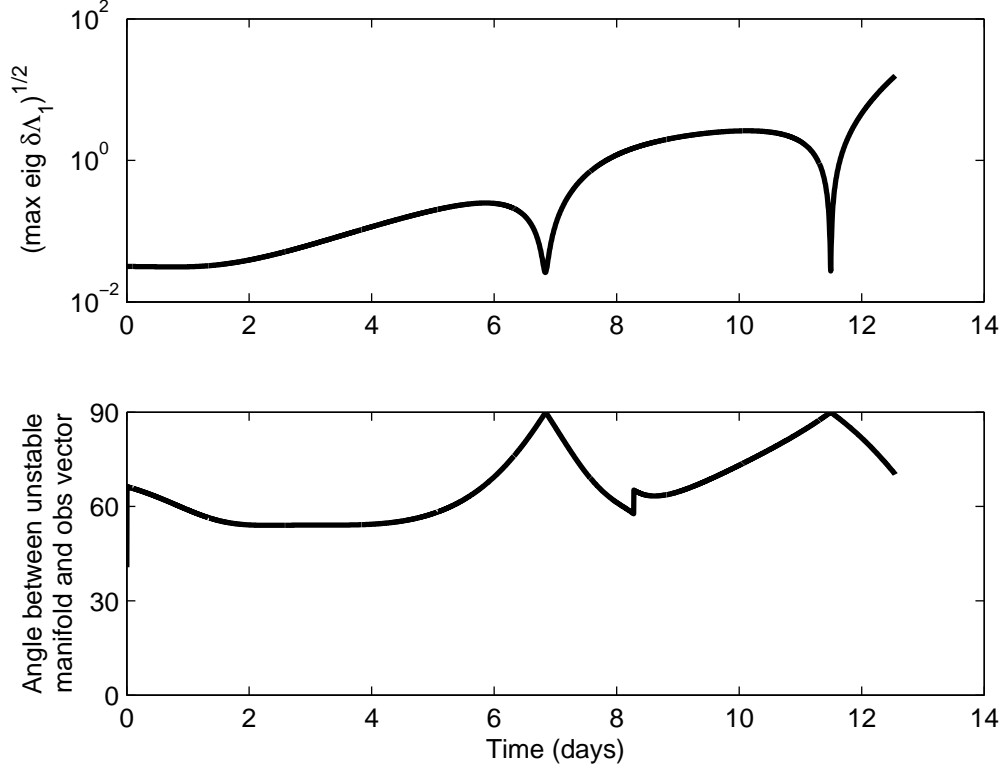


Figure 5.7: Relationship between the sensing direction-local unstable manifold angle and the observation effectiveness.

Thus we find the answer to the question posed in the beginning of the chapter. The values of $\Delta\tau$, τ_1 , and τ_2 influence the accuracy of orbit determination because they change geometry of the observations with respect to the unstable manifold. This changes the timing and extent of the “blackout periods” when the observations are perpendicular to the local unstable manifold and are not effective. If a blackout period occurs near the end of the fit span, the observations that could have been the most effective are basically blocked out or lost. Knowledge of these principles can be used to advantage when scheduling tracking passes or maneuvers as described by Anderson et al. (2003), and should be an important part of any unstable orbit navigation.

Chapter 6

Liaison Navigation for Other Three-body Systems

While simulations of Liaison Navigation in Chapter 4 focused on Earth-Moon halo orbits, this chapter investigates the usefulness of Liaison Navigation in other three-body systems, starting with Sun-Earth halo orbits. An analysis is performed using a Sun-Earth halo orbit similar to the Genesis science orbit, and then the investigation is extended to Sun-Mars halo orbits. Finally, Liaison navigation results were generated for six three-body systems in our Solar System that span the range of common three-body mass ratios.

6.1 Sun-Earth Halo Orbits

To evaluate the effectiveness of Liaison Navigation in Sun-Earth halo orbits, a set of simulations was performed that were similar to those in Chapter 4. Families of halo orbits were generated around the two collinear Lagrange points near the Earth in the Sun-Earth system (EL_1 and EL_2). For each family of halo orbits, a certain number were selected as test orbits, and ephemeris files were generated for each one. Figures 6.1 and 6.2 show the distribution of the initial conditions of the test halo orbits.

6.2 Sun-Earth Liaison Navigation Methods

Orbit determination tests were conducted using the same settings as in Chapter 4, with some exceptions. Range observations were generated from the ephemeris files every 0.001 time units, which is about 84 minutes in the Sun-Earth system. The same orbit determination error

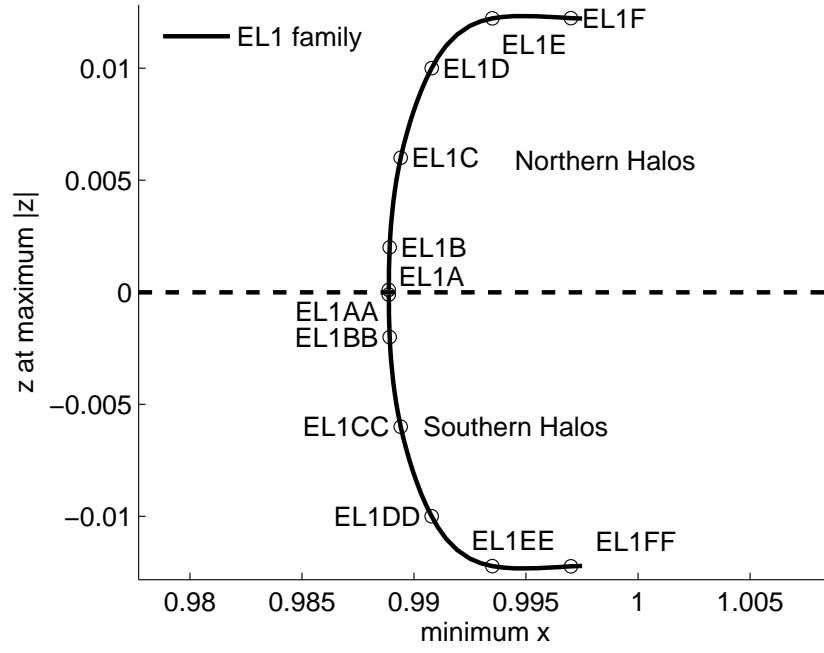


Figure 6.1: Initial conditions and names of Sun-Earth L_1 test orbits.

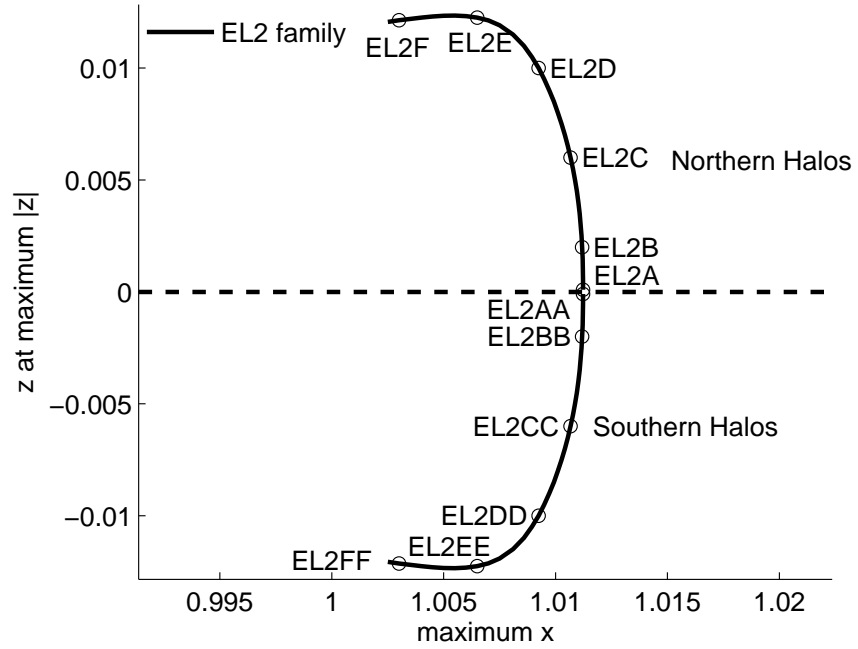


Figure 6.2: Initial conditions and names of Sun-Earth L_2 test orbits.

metric used in Chapter 4, β_{ave} , was used again.

The value of the error metric, β_{ave} , varies with the difference in phase angle, τ for the satellites as outlined in Chapter 5, so it became necessary to find one representative value of β_{ave} for each combination of orbits. This metric was called β_{con} and is used to rank the navigation accuracy of the different constellation geometries. In order to find a value of β_{con} that would be a good approximation of the true constellation navigation accuracy, the value of β_{ave} was computed for the following values of $\Delta\tau$ (in degrees):

$$\left[0 \quad 7.5 \quad 15 \quad 30 \quad 60 \quad 90 \quad 120 \quad 150 \quad 180 \quad 210 \quad 240 \quad 270 \quad 300 \quad 330 \quad 345 \right]$$

β_{ave} also varies slightly when values of τ_1 and τ_2 themselves were changed while holding $\Delta\tau$ constant. To account for those variations, the value of β_{ave} was computed three different times with all the values of $\Delta\tau$ listed above. τ_1 was set to 0, 90 and 180 degrees for the three different runs. Values of β_{con} were computed in the manner described in Chapter 4, and the results show the same trends that were seen for the Earth-Moon halo orbits in Chapter 4.

It was hypothesized that the values of β_{con} for Sun-Earth halo orbits would be larger than for Earth-Moon halo orbits, since the Sun-Earth halo orbits themselves are larger. However, it appears that the values of β_{con} at EL₁ and EL₂ are very similar to the values of β_{con} at LL₁ and LL₂ when the fits span the same period in nondimensional time units. Even the general pattern in the results is remarkably similar. It appears that the actual size of the halo orbits does not have much affect on the orbit accuracy.

6.3 Liaison Navigation Analysis of the Genesis Mission

While keeping the same test settings was useful for comparing the performance of Liaison Navigation in the Earth-Moon and Sun-Earth systems, it is not necessarily practical. For example, a fit span of 1.5 orbit periods might be feasible in the Earth-Moon system where it is approximately three weeks. However, in the Sun-Earth system that translates into fit span of about nine months. Waiting that long for an orbit solution is definitely not feasible.

The Genesis mission provides a recent example of a mission to Sun-Earth libration points. The trajectory design for the planned science orbit at EL_1 is a useful reference (Howell et al., 1997). The general characteristics of the science orbit seemed to match the EL1B orbit relatively well, in that the maximum vertical components of the Genesis orbit and EL1B were very similar. The planned fit span for Genesis was 60 days, with 60 days between stationkeeping maneuvers (Han et al., 2001). Using two spacecraft in EL1B, crosslink range observations were simulated every 2×10^{-4} nondimensional units, or about 16 minutes, for 60 days. After trying various differences in phase angle, β_{con} was 774 km with an optimum $\Delta\tau$ of 150° . This level of accuracy would not have been acceptable for Genesis, which had estimated error on the order of 10 km. The reason for the large error was that the fit span was too short for Liaison Navigation to converge. Various techniques were tried to achieve sufficient convergence in the required 60 days, which is about 1/3 of the halo orbit period.

The first attempt at achieving faster convergence was to decrease the interval between observations by half to about 8 minutes. This doubled the number of observations. After running the tests again, the resulting β_{con} was 948 km, which was even higher than when the lower data rate was used. This increase was probably only a statistical artifact due to variations in the β_{con} metric because of the small sample size used to generate it.

The second attempt at achieving faster convergence was to add an additional satellite. This turned out to be much more effective. With three satellites on the EL1B orbit separated by 120 degrees of phase angle, the worst value of β_{ave} was only 690 m. The other effective way of achieving faster convergence using Liaison Navigation was to put one of the spacecraft into a very short period orbit. For the Earth-Moon system, putting one of the spacecraft into a relatively short period lunar orbit achieved this in a practical way. However, if the goal is to achieve autonomy, placing a spacecraft in an Earth orbit in the Sun-Earth system is not very practical. One might as well use ground-based tracking stations on the Earth instead of an Earth-orbiting satellite since the telecommunication link distance would be about the same. The other option is to include more spacecraft in the constellation to improve convergence time.

A large number of tests were run using the Kalman filter with different numbers of spacecraft to test the speed of convergence. The time to convergence was judged visually and somewhat subjectively. From the results of these tests, an approximate relationship between the number and placement of the spacecraft and the speed of convergence was generated. The results shown in Table 6.1 describe approximately how long it takes to converge on a solution using Liaison Navigation (in terms of halo orbit periods) based on the number of satellites in various constellations. Of course, actual results vary and should always be verified for any particular mission being planned.

Table 6.1: APPROXIMATE SPEED OF CONVERGENCE FOR LIAISON NAVIGATION WITH VARIOUS CONSTELLATION TYPES.

No. of halo s/c	No. of planetary s/c	Convergence time in halo orbit periods
2	0	1
3	0	1/2
4	0	1/3
5	0	1/4
1	1	1/4
2	1	1/8

Note: An example of a planetary spacecraft (s/c) would be one in a lunar orbit with a period much shorter than the halo.

From Table 6.1, it can be seen that the short-period planetary orbits lead to the fastest convergence for a specific number of spacecraft.

6.4 Three Spacecraft Constellations in Sun-Earth Halo Orbits

Next, three-spacecraft constellations were simulated using the rest of the Sun-Earth halo test orbits. All three spacecraft were placed in the same halo orbit, making it a Halo₃ constellation. For these tests, only two of the three spacecraft could track each other at any one time. Actual spacecraft hardware could lead to simultaneous links between all three, but that was not simulated at this time. After about every 27 hours, the link pair was rotated so that each spacecraft took turns being inactive. Range observations were simulated from the ephemeris

files every 2×10^{-4} time units, which is about 16 minutes, and the total fit span was 1/3 of the halo orbit period. The range observations had an added white noise component with a standard deviation of 1 m.

The first spacecraft was placed at the phase angles (in degrees)

$$\begin{bmatrix} 0 & 45 & 90 & 135 & 180 & 225 & 270 & 315 \end{bmatrix}$$

The next two spacecraft were spaced evenly ahead of the first with the same $\Delta\tau$ such that $\Delta\tau = \tau_2 - \tau_1 = \tau_3 - \tau_2$. For each value of τ_1 , the value of β_{ave} was computed in a loop for each $\Delta\tau$ listed below, in degrees.

$$\begin{bmatrix} 15 & 30 & 60 & 90 & 120 \end{bmatrix}$$

For each $\Delta\tau$, β_{ave} was computed for each of the eight values of τ_1 . The highest β_{ave} of the eight was selected. Of those selected values of β_{ave} , the lowest is chosen to be β_{con} , which represents the overall accuracy of that constellation. This was done for all of the Northern Sun-Earth halos. As has been seen before, β_{con} for the EL1A halo orbits was the worst, around 10 km, due to the proximity to the plane of symmetry. The error goes down to about 500 m for EL1C through EL1E and jumps back up to 2 km at EL1F. EL₂ orbits showed a very similar pattern. This general pattern was also seen with the lunar halo orbits.

6.5 Sun-Mars Halo Orbits

A set of Sun-Mars halo orbits were generated using the same techniques that were used for the Sun-Earth halo orbits. The halo families were generated for the AL₁ and AL₂ Lagrange points, and the initial conditions for the halos are shown in Figures 6.3 and 6.4. It was found that the Sun-Mars halo orbits had the same problem with quick convergence as the Sun-Earth halos. However, at Mars the halo orbit periods are about one year instead of six months. This means that the Halo₂ constellations at Mars would have to have fit spans about a year long, using the rule of thumb in Table 6.1.

Decreasing the length of the fit spans at Mars is a little easier than at Earth. Short period

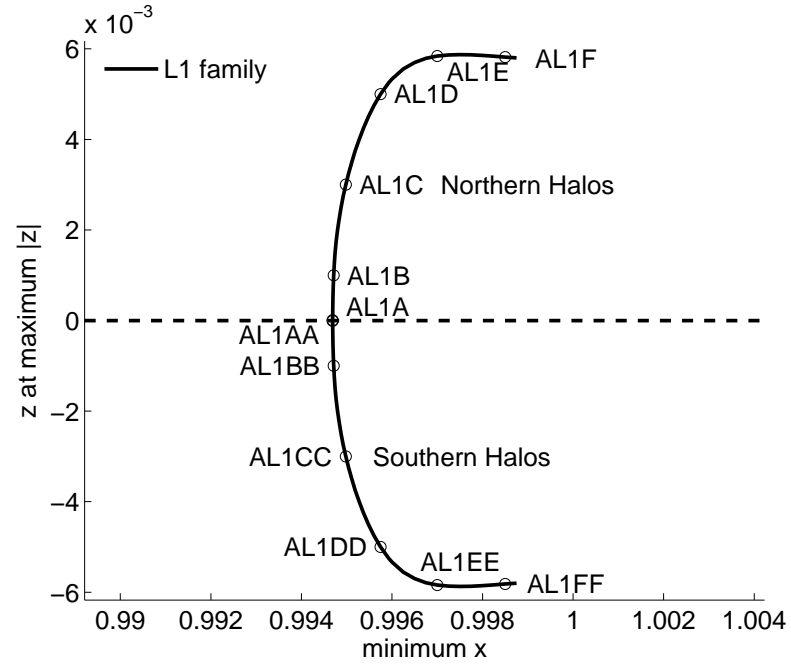


Figure 6.3: Initial conditions and names of Sun-Mars L_1 test orbits.

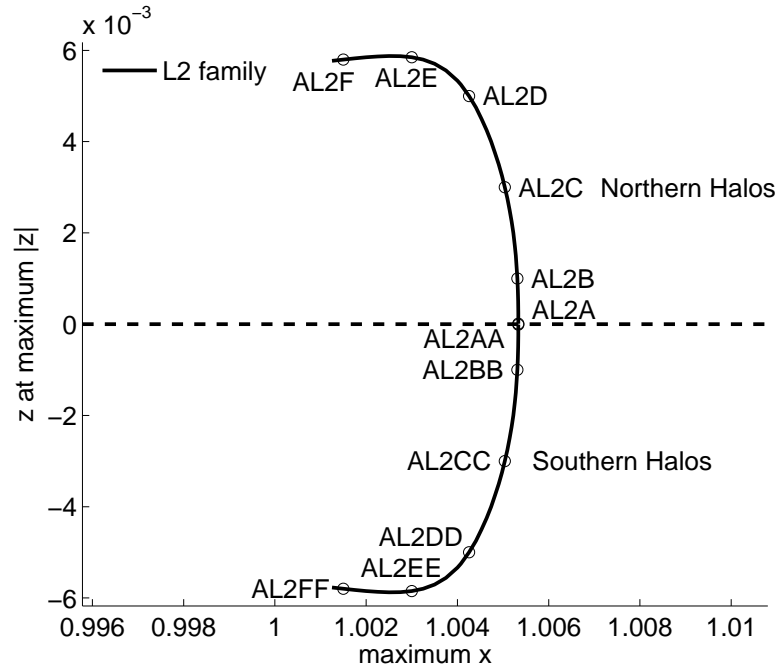


Figure 6.4: Initial conditions and names of Sun-Mars L_2 test orbits.

Mars orbiters can be used to significantly speed up convergence while keeping the telecommunication link distances short as compared to Mars-Earth links. The initial conditions for a low Mars orbit was created using Keplerian elements. The semimajor axis was 10,000 km, the inclination was 90° , the longitude of the node was also 90° , and the other elements were zero. These initial conditions were converted to Cartesian position and velocity and converted to the Sun-Mars rotating coordinate frame. The orbit was then propagated using the three-body equations of motion, and an ephemeris file was created.

A test was performed using a three-satellite constellation at Mars. Two of the spacecraft were in the AL1D halo orbit, separated by a $\Delta\tau$ of 150° . The SST measurements simulated were SST range with Gaussian noise with a 1σ of 1 m. The measurements were restricted so that only two spacecraft could track each other at any one time. Range biases were included in the state estimates, and a fit span of about 45 days was used. The value of β_{ave} for this test was 82 m. This would be a very good result if it were achieved in an actual mission. The problem is that the fit span for the Mars orbit is 45 days, and it would be hard to get a good fit to a Mars orbit that long. A fit span for the Mars orbit would ideally be only a day or two.

The problem with reducing the fit span for the constellation to only a few days is that the state is not truly observable. The true orbits and the estimate of the orbits could drift apart over time without being observed. To solve this problem while still using the batch processor, a “hybrid” fit span was used. With this hybrid fit span, 90 days of Halo₂-type tracking data is used for the two Mars halo spacecraft, but the data from the Mars orbiter is only included on the last 2 days of that 90-day period. The beginning and ending dates for these two fit spans of different lengths then move up two days for the next orbit update. This ensures a truly observable estimate and results in fairly good accuracy. β_{ave} for this case was about 2.1 km. The two halo orbiters had $\bar{\beta}$'s of about 3 km, and the Mars orbiter had a $\bar{\beta}$ of 33 m.

These results could be improved by including some of the previous 2-day fit spans for the Mars orbiter and treating the Mars orbiter as if it were an additional spacecraft in the state estimate for each 2-day fit span used. The estimates for the Mars orbiter on the earlier 2-day

fits would be discarded since they would not be as timely as the estimate generated on the last 2-day fit. However, the observations from those earlier 2-day fits would still improve the overall accuracy of the constellation.

A way of avoiding the need for hybrid fit spans would be to use a sequential processor such as the Extended Kalman Filter, which is described in Chapter 9.

6.6 Conclusions for Sun-Earth and Sun-Mars Halo Orbits

The orbit accuracy of Liaison Navigation for Sun-Earth halo orbits turned out to be very similar to Earth-Moon halo orbits when the data rate and fit span length were equal in nondimensional time units. For Sun-Earth halo orbits, the halo orbit period is approximately six months, and it would be impractical to integrate the orbits over the entire period. That would mean that the first orbit estimates would not be available for six months. In addition, several stationkeeping maneuvers should be performed each period. These conditions require that Liaison Navigation converge within only a fraction of a halo orbit period. A higher data rate does not help achieve significantly faster convergence. There were two effective methods found for achieving faster convergence. The first was to put one of the spacecraft in a short period orbit. An example of that would be a lunar orbit in the case of the Earth-Moon system. The second method was to increase the number of spacecraft in the Liaison constellation.

A simulation of a three-satellite constellation in an orbit similar to the Genesis science orbit at EL_1 resulted in a three-dimensional orbit accuracy of 690 m. An actual application of Liaison Navigation in the Genesis orbit would have larger error than that, but achieving this level of accuracy provides some more evidence that Liaison Navigation could be practical and effective.

At Mars, the even longer halo orbit periods create additional complications. A hybrid fit span approach similar to the one described here would probably be useful and could result in acceptable orbit accuracies.

6.7 Other Three-body Systems

Halos were generated around the L_1 and L_2 Lagrange points of a total of six three-body systems that represent a wide range of planetary systems. The parameters for the six three-body systems are displayed in Table 6.2.

Table 6.2: THREE-BODY SYSTEMS USED FOR LIAISON NAVIGATION SIMULATIONS IN THE CRTBP.

μ	Time Conversion (days/nondim time)	Length Conversion (km/nondim length)	Solar System Equivalent
0.01215	4.343	3.844×10^5	Earth-Moon
0.0009545	689.5	7.783×10^8	Sun-Jupiter
2.366×10^{-4}	2.538	1.222×10^6	Saturn-Titan
4.700×10^{-5}	0.2816	4.218×10^5	Jupiter-Io
3.003×10^{-6}	58.13	1.496×10^8	Sun-Earth
3.244×10^{-7}	109.3	2.279×10^8	Sun-Mars

Liaison Navigation was performed for two- and three-spacecraft constellations in varying geometries and fit span lengths for each of the three-body systems in Table 6.2. The orbit determination accuracy was generated along with other statistics. The results for all of the three-body systems show very similar patterns.

Chapter 7

Four- and n-body Models and Simulations

This chapter looks at the effects of additional bodies on orbit determination accuracy in lunar halo orbits (Hill et al., 2006a). First, a four-body problem is simulated. The new fourth body is the Sun. Solar gravity and radiation pressure are added to the force model when generating the halos. The gravitational model used is called the bicircular model (Gómez et al., 2001). Next, the JPL ephemeris for the planets is used to create halo orbits with the added effects of all of the Solar System planets. For four- and n-body models, a multiple shooting differential corrector must be used to obtain halo orbits that are not truly periodic, but “quasi-periodic.”

7.1 Bicircular Model

In the bicircular model, the Earth and Moon travel in circles about their mutual barycenter. The Sun travels in another circle about the Earth-Moon barycenter. Usually, this is done in a rotating frame so that the Earth and Moon always lie on the x axis of the frame, with the Sun still traveling in a circle about the origin with the proper period. A slight variation on the bicircular model was used for this study. It can be called the “inertial bicircular model.” In the inertial bicircular model, the Sun and the Earth-Moon barycenter travel in circles about the Sun-Earth/Moon barycenter. The Earth and Moon then travel in circles about the Earth-Moon barycenter. This was done to make the frame inertial, which simplifies the acceleration terms due to the gravity of each body. The inertial bicircular model also will make it more straightforward when adding in changes in the geometry of the primary body orbits.

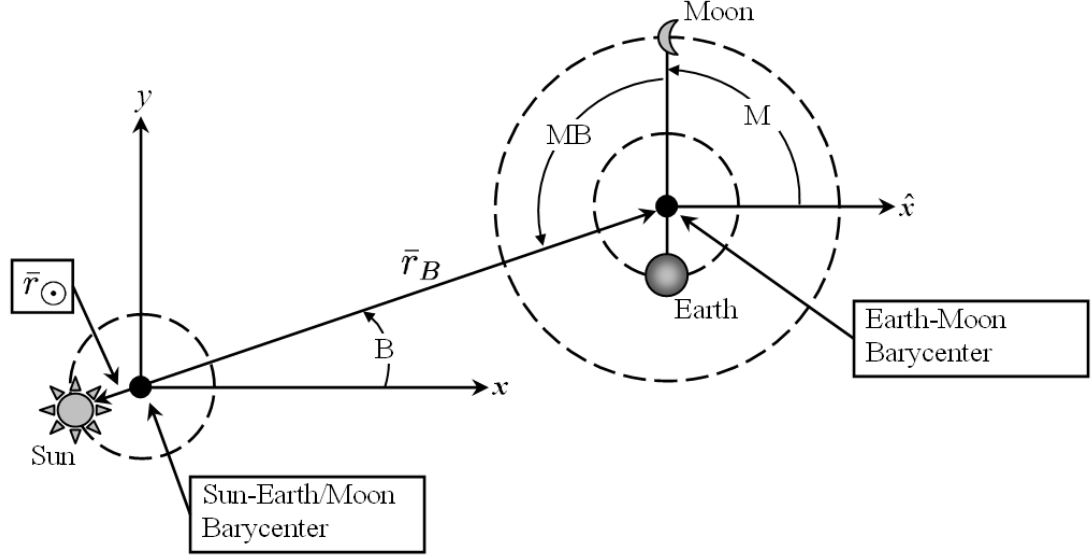


Figure 7.1: Geometry of the Inertial Bicircular Model.

Figure 7.1 shows an illustration of the inertial bicircular model. In the figure, the origin is at the Sun-Earth/Moon barycenter. B is the angle measured from the x axis of the inertial frame to the line from the Sun to the Earth-Moon barycenter. M is the angle between the x direction and the line joining the Earth and Moon. MB is the angle between the Earth-Moon line and the line between the Earth-Moon barycenter and the Sun. All angles are positive in the counter-clockwise direction.

The position of the Earth-Moon barycenter is computed with the following equation:

$$\mathbf{r}_B = r_{\odot\oplus}(1 - \mu_3) [\cos(B) \quad \sin(B) \quad 0]^T. \quad (7.1)$$

\mathbf{r}_B is the vector position of the Earth-Moon barycenter. $r_{\odot\oplus}$ is the length of the semimajor axis of the Earth's orbit about the sun. μ_3 is the gravitational parameter for the three-body system including the Sun and the Earth/Moon Barycenter. It is computed as follows:

$$\mu_3 = \frac{\mu_{\oplus} + \mu_{\mathcal{L}}}{\mu_{\oplus} + \mu_{\mathcal{L}} + \mu_{\odot}}. \quad (7.2)$$

The position of the Sun is computed with this equation:

$$\mathbf{r}_{\odot} = -r_{\odot\oplus} \mu_3 [\cos(B) \quad \sin(B) \quad 0]^T. \quad (7.3)$$

The positions of the Earth and Moon are found with these equations:

$$\mathbf{r}_{\zeta} = \mathbf{r}_B + (1 - \mu_2) r_{\oplus\zeta} [\cos(M) \quad \sin(M) \quad 0]^T \quad (7.4)$$

$$\text{and } \mathbf{r}_{\oplus} = \mathbf{r}_B - \mu_2 r_{\oplus\zeta} [\cos(M) \quad \sin(M) \quad 0]^T. \quad (7.5)$$

μ_2 is the gravitational parameter for the three-body system which includes the Earth and the Moon:

$$\mu_2 = \frac{\mu_{\zeta}}{\mu_{\oplus} + \mu_{\zeta}}. \quad (7.6)$$

$r_{\oplus\zeta}$ is the length of the semimajor axis of the Moon's orbit about the Earth.

Since the Moon's orbit about the Earth is not exactly in the ecliptic plane, it was advantageous to be able to adjust the inertial bicircular model accordingly to see what would happen to the orbit determination accuracy. To do this, further adjustments were made to the bicircular model so that the Earth and Moon traveled in circular orbits that were inclined with respect to the plane of the ecliptic, which in this case is the plane of the Sun and the Earth/Moon barycenter. Figure 7.2 shows how this was done.

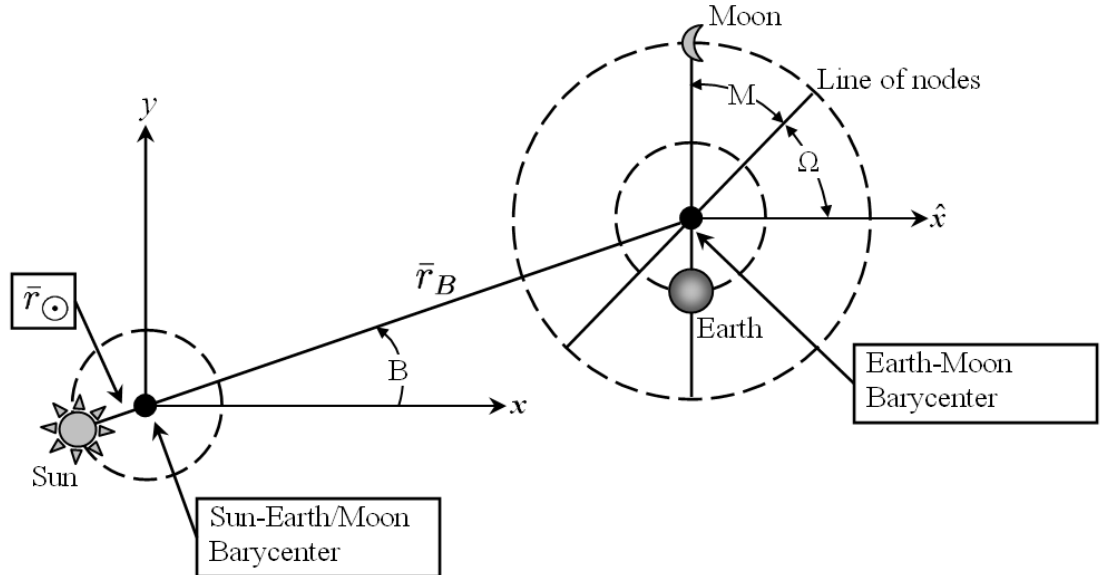


Figure 7.2: Geometry of the inclined Inertial Bicircular Model.

Figure 7.2 is similar to Figure 7.1, except Ω is the angle between the x direction and the ascending node of the Moon. At this point, the Moon's orbit ascends through the ecliptic with inclination i . The ecliptic in this case is the plane containing the Sun and the Earth-Moon barycenter. M is the angle from the ascending node to the line joining the Earth and Moon.

The positions of the Earth-Moon barycenter and the Sun are computed using the equations listed previously. The positions of the Earth and Moon are computed, then rotated first about the x direction by the angle i and then about the z direction by the angle Ω .

$$\mathbf{r}_{\mathcal{L}} = \mathbf{r}_B + (1 - \mu_2) r_{\oplus \mathcal{L}} \begin{bmatrix} \cos(-\Omega) \cos(M) + \sin(-\Omega) \cos(-i) \sin(M) \\ -\sin(-\Omega) \cos(M) + \cos(-\Omega) \cos(-i) \sin(M) \\ \sin(-i) \sin(M) \end{bmatrix} \quad (7.7)$$

$$\mathbf{r}_{\oplus} = \mathbf{r}_B - \mu_2 r_{\oplus \mathcal{L}} \begin{bmatrix} \cos(-\Omega) \cos(M) + \sin(-\Omega) \cos(-i) \sin(M) \\ -\sin(-\Omega) \cos(M) + \cos(-\Omega) \cos(-i) \sin(M) \\ \sin(-i) \sin(M) \end{bmatrix} \quad (7.8)$$

In orbit determination tests, results from the three-body problem and the bicircular model were to be compared. To keep units and numbers consistent in ephemerides for both models, the bicircular accelerations were converted to three-body accelerations by making the spacecraft's acceleration due to the Sun's gravity equal to the acceleration of the Earth-Moon barycenter. This effectively negates the effect of the Sun on the spacecraft.

Finally, some orbits were propagated with the effect of SRP included as well. The acceleration due to SRP is (Vallado and McClain, 2001)

$$\ddot{\mathbf{r}}_{SRP} = p_{SR} c_R \frac{A_{\odot}}{m} \frac{\mathbf{r}_{\odot sat}}{|\mathbf{r}_{\odot sat}|}. \quad (7.9)$$

c_R is the reflectivity of the spacecraft. A_{\odot} is the cross-sectional area of the spacecraft facing the Sun in square meters. m is the mass of the spacecraft in kilograms. $\mathbf{r}_{\odot sat}$ is the vector from the center of the Sun to the spacecraft. p_{SR} is the pressure of solar radiation in Pascals. This is about 4.51×10^{-6} Pa at the Earth. For varying distances from the Sun, p_{SR} would be

$$p_{SR} = 4.51 \times 10^{-6} \text{ Pa} \frac{(149,597,870 \text{ km})^2}{|\mathbf{r}_{\odot sat}|^2}. \quad (7.10)$$

$\mathbf{r}_{\odot sat}$ should be in km. A factor ℓ can be applied to represent the fraction of the Sun's face that is visible. When km and km/s are the units used for position and velocity, respectively, the acceleration due to the Sun's gravity and SRP can be combined, resulting in

$$\ddot{\mathbf{r}}_{SRP+\odot} = \left[\ell c_R \frac{A_{\odot}}{m} (149,597,870 \text{ km})^2 (4.51 \times 10^{-6} \text{ Pa}) \frac{1 \text{ km}}{1000 \text{ m}} - \mu_{\odot} \right] \frac{\mathbf{r}_{\odot sat}}{|\mathbf{r}_{\odot sat}|^3}. \quad (7.11)$$

$\ell = 1$ when there is a clear line of sight vector between the spacecraft and the Sun, and $\ell = 0$ when the Sun's light is blocked by a body. When determining the line of sight, it was assumed that the Moon would be the only body that would eclipse the Sun. The angle between the center of the Moon and the center of the Sun was called ς and is found using the dot product.

$$\varsigma = \arccos \left(\frac{\mathbf{r}_{\odot sat} \cdot \mathbf{r}_{\mathcal{L} sat}}{|\mathbf{r}_{\odot sat}| |\mathbf{r}_{\mathcal{L} sat}|} \right) \quad (7.12)$$

$\mathbf{r}_{\odot sat}$ is the vector from the center of the Sun to the spacecraft and $\mathbf{r}_{\mathcal{L} sat}$ is from the Moon to the spacecraft. $|\mathbf{r}_{\odot sat}|$ and $|\mathbf{r}_{\mathcal{L} sat}|$ are the magnitudes of those vectors. The angle between the center and limb for the two bodies are found assuming that the bodies are spherical.

$$\varsigma_{\odot} = \arctan \left(\frac{R_{\odot}}{|\mathbf{r}_{\odot sat}|} \right) \quad (7.13)$$

$$\varsigma_{\mathcal{L}} = \arctan \left(\frac{R_{\mathcal{L}}}{|\mathbf{r}_{\mathcal{L} sat}|} \right) \quad (7.14)$$

R_{\odot} and $R_{\mathcal{L}}$ are the radii of the primary bodies. The relations below were used in determining ℓ .

$$\ell = \begin{cases} 1, & \varsigma \geq \varsigma_{\mathcal{L}} + \varsigma_{\odot} \\ \frac{\varsigma - \varsigma_{\mathcal{L}}}{2\varsigma_{\odot}} + \frac{1}{2}, & \varsigma_{\mathcal{L}} - \varsigma_{\odot} \leq \varsigma < \varsigma_{\mathcal{L}} + \varsigma_{\odot} \\ 0, & \varsigma < \varsigma_{\mathcal{L}} - \varsigma_{\odot} \end{cases} \quad (7.15)$$

This is based on the assumption that $\varsigma_{\mathcal{L}} \gg \varsigma_{\odot}$. If that is false, it only negatively affects the computation of ℓ when the Sun is partially eclipsed.

7.2 Multiple Shooting Differential Corrector

In the four-body problem, as well as other n-body problems, there are no longer any periodic solutions because the same positions of the primaries do not repeat within any reason-

able length of time. This means that the periodic halo orbits found in the three-body problem do not occur in the four-body problem. Instead, trajectories must be computed that are fairly close to periodic, at least for the time interval desired. These quasi-periodic orbits can be called quasi-halo orbits. A numerical method used to find a continuous libration trajectory in the four-body problem is a multiple shooting differential corrector adapted from the work of Howell and Pernicka (1988) and Wilson. This technique can also be used to find numerical examples of the nonperiodic Lissajous orbits described in Chapter 3.

To initialize the multiple shooting differential corrector, a reference trajectory is required. For these “initial guess” trajectories, a halo orbit from the CRTBP was used which had been rotated and scaled to fit the inertial bicircular frame. Patch points were selected along the halo so that there were four patch points per halo orbit period with a certain time interval between them. A trajectory segment is propagated using the inertial bicircular model starting at each patch point for the proper amount of time. These trajectory segments won’t match up at the end points due to the added effect of the Sun’s gravity. Using two levels of iteration, the initial conditions of each segment are corrected until they can be patched together into a continuous trajectory.

7.2.1 Level 1

In the first level of iteration, the velocity at each patch point is corrected until the end positions on each trajectory segment match the start positions of the succeeding segment. Putting all the segments together result in a trajectory that is continuous in position, but not in velocity. There will be velocity discontinuities or ΔV ’s at each interior patch point.

7.2.2 Level 2

The ΔV ’s at each interior patch point are reduced in the second level of iteration by adjusting the positions and times of the patch points. After correcting the positions and times of the patch points, the Level 1 iteration must be repeated to make the trajectory continuous in

position. After the ΔV 's reach a sufficiently small value, the trajectory is considered continuous.

7.2.3 Implementation of Multiple Shooting

When using the multiple shooting differential corrector, the positions and times at the exterior patch points of the trajectory are usually adjusted to a much greater extent than the interior patch points. This results in some “end effects” in the trajectories where the spacecraft would quickly fall away from the libration point if the trajectory were propagated away from the end points. For this study, libration orbits of one halo orbit period were desired. To eliminate end effects, the reference trajectory used in the multiple shooting differential corrector consisted of three complete revolutions of the halo orbit. After converging on a continuous trajectory, the first and last revolutions of the quasi-periodic orbit were discarded and the center portion of the orbit was used to create an ephemeris file.

7.2.4 Ephemerides for Orbit Determination

Halo orbits from the CRTBP were used as initial conditions for finding quasi-periodic halo orbits in the bicircular model. The CRTBP halo orbits were computed using the technique explained by Howell (1984). Families of halo orbits were generated around the lunar L_1 and L_2 Lagrange points (LL_1 and LL_2) in the CRTBP. For each family of halo orbits around a Lagrange point, a certain number were selected as test orbits and ephemeris files were generated. Figures 4.1 and 4.2 show the distribution of the initial conditions of the test halo orbits. The halo orbits shown that have a “Northern” orientation were rotated and scaled into the inertial bicircular frame to initialize the multiple shooting differential corrector.

An example of a quasi-periodic orbit obtained from the multiple shooting differential corrector is shown next to the CRTBP halo used to generate it in Figure 7.3. Both are displayed in the rotating frame of the CRTBP, where a length unit is equal to the distance between the Earth and the Moon. τ was described in Chapter 3. The orbits are plotted for slightly more than one halo orbit period, and they are very similar. It might be possible to see that the bicircular

orbit does not exactly repeat. The orbit does not come back exactly to its initial position and is slightly offset in the upper middle portion of the left side.

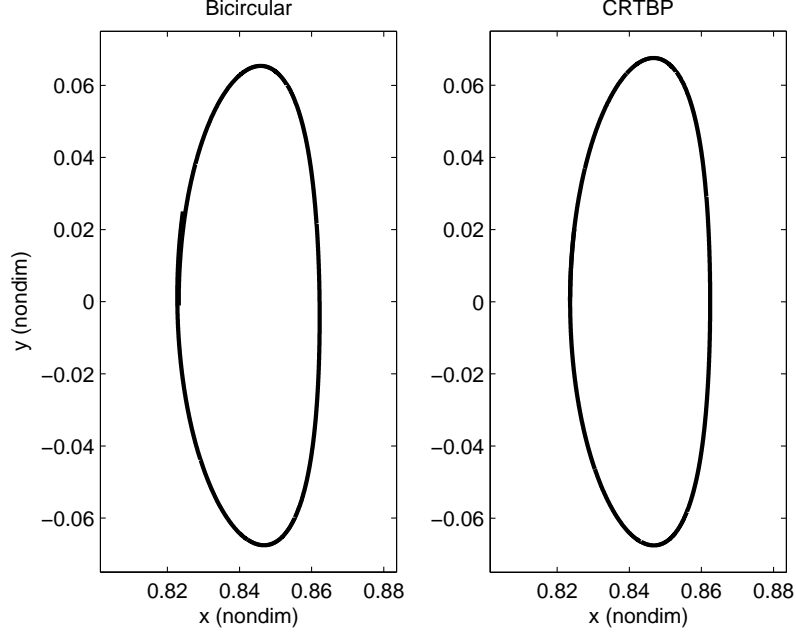


Figure 7.3: Halo orbits computed in the CRTBP and the Bicircular model using LL1B with $\tau = 0$ and $MB(t_0) = 0$ and projected into the x-y plane.

7.3 Test Methods

To determine how the inclusion of a fourth body affected the orbit determination accuracy, a covariance analysis was conducted using the techniques outlined in Chapter 4. All of the constellations used in the simulations consisted of two spacecraft in bicircular orbits which were generated from the same three-body halo orbit, making them Halo₂ constellations. The two spacecraft were separated by a difference in phase angle, $\Delta\tau$, that remained constant. Since the Northern and Southern halo orbits are symmetric, only the Northern halo orbits were used. The two spacecraft tracked each other continuously, unless the Earth or the Moon blocked the line of sight (LOS) vector. Range observations were generated from the ephemeris files every six minutes. These observations were used to generate the \tilde{H}_i matrices. The state transition

matrices were obtained from the ephemeris files for each orbit. The information matrix, H^TWH , was computed, and the covariance matrix was used to compute navigation error metrics without actually estimating the state. The range observations had an added white noise component with a standard deviation of 1 m. The fit span for these tests was one halo orbit period.

7.3.1 Bicircular

For the bicircular constellations, the values of τ and the positions of the primaries were computed using the following equations:

$$\begin{aligned}\tau_1 &= 0, \\ \tau_2 &= \begin{bmatrix} 30 & 60 & 90 & 120 & 150 & 180 & 210 & 240 & 270 & 300 & 330 \end{bmatrix}, \\ S(t_0) &= 0, \\ \text{and } MB(t_0) &= \begin{bmatrix} 0 & -45 & -90 & -135 & -180 & -225 & -270 & -315 \end{bmatrix}.\end{aligned}$$

All angles are shown in degrees. $S(t_0)$ is the value of angle S at time t_0 , where t_0 is the initial epoch in the ephemeris. Similarly, $MB(t_0)$ is the value of angle MB at time t_0 . Since there are eleven different values of τ_2 and eight of $MB(t_0)$, for each two-spacecraft constellation there were 88 different combinations for orbit determination runs. Choosing β_{con} from those 88 different runs was performed by averaging the values of β_{ave} for each τ_2 . The lowest average was chosen to be β_{con} .

For the CRTBP constellations, the halo orbits were propagated by nullifying the effect of Sun on the spacecraft as described previously. Since the positions of the primaries don't matter, the values of τ were computed using the following equations:

$$\begin{aligned}\tau_1 &= 0, \\ \text{and } \tau_2 &= \begin{bmatrix} 30 & 60 & 90 & 120 & 150 & 180 & 210 & 240 & 270 & 300 & 330 \end{bmatrix}.\end{aligned}$$

Angles are shown in units of degrees. For the CRTBP runs, there were only 11 runs computed. β_{con} for the CRTBP runs was the lowest value of β_{ave} .

7.3.2 Inclined Bicircular

For the inclined bicircular constellations, the CRTBP halo orbits LL1B and LL1C were used to generate the ephemerides for use in orbit determination. The values of τ and the positions of the primaries were computed using the following equations:

$$\begin{aligned}\tau_1 &= 0, \\ \tau_2 &= 120, \\ S(t_0) &= 0, \\ M(t_0) &= \begin{bmatrix} 0 & 30 & 60 & 90 & 120 & 150 \end{bmatrix}, \\ \text{and } \Omega &= \begin{bmatrix} 0 & 30 & 60 & 90 & 120 & 150 \end{bmatrix}.\end{aligned}$$

$M(t_0)$ is the value of angle M in Figure 7.2 at time t_0 . Ω is the value of that angle in the same figure. When $M(t_0)$ and Ω were between 180 and 360 degrees, it was found that the orbit determination results were almost identical to when they were between 0 and 180 degrees. Because of that, the results were not computed between 180 and 360 degrees. Since there are six different values of $M(t_0)$ and six of Ω , for each two-spacecraft constellation there were 36 different orbit determination runs. Choosing β_{con} from those 36 different runs was performed by averaging all the values of β_{ave} .

This process was performed for inclinations of 0, 1, 2, 5, and 10 degrees. The effect of the inclination could be seen by comparing the results for inclined orbits to the zero-inclination case.

7.3.3 Solar Radiation Pressure

To test the effect of SRP on the orbit determination accuracy, a pair of ephemerides was created using equations of motion that included SRP accelerations in the multiple shooting differential corrector. These orbits were initialized using the LL1B halo orbit at $\tau_1 = 0^\circ$ and $\tau_2 = 120^\circ$, and the inclined inertial bicircular model with a 5° inclination between the Earth-Moon orbit and the Sun-Earth orbit. The initial positions of the primaries were found using

$M(t_0) = 0$ and $\Omega = 0$. The fit span was 1 halo orbit period, with observations every six minutes. The standard deviation of the noise on the range observations was 1 m. c_R was 1.5, A was 5 m², and m was 1000 kg.

7.4 Four-body Test Results

7.4.1 Bicircular

When comparing the values of β_{ave} for the CRTBP and the inertial bicircular model, there was a great degree of variability. Depending on the geometry of the primary bodies, β_{ave} for the CRTBP could be larger or smaller than for the inertial bicircular model. Table 7.1 shows the average percent increase or decrease in β_{ave} . It also shows the average standard deviation of β_{ave} in the bicircular model. These values of standard deviation were computed separately for each $\Delta\tau$ and then averaged. The standard deviations are displayed as percentages of β_{con} for the CRTBP. As an example of how to read the table, a constellation of two spacecraft in the bicircular LL1D halo orbit would have orbit determination results about 0.41% better than the CRTBP on average, but the accuracy would vary $\pm 12\%$ of 39.9 m as the geometry of the Sun, Earth, and Moon changed. Averaging it all together, the bicircular β 's are 3.3% larger than for CRTBP with a standard deviation of about 15%. As stated before, these results are very rough due to the large variability.

7.4.2 Inclined Bicircular

The LL1B and LL1C orbits were selected for tests involving inclination between the plane with the Sun and Earth/Moon barycenter and the Earth-Moon orbit plane. Since the Moon's orbit is inclined about 5° with respect to the ecliptic, a range of inclinations were chosen around this value. It was found that the higher the inclination, the worse β turned out to be. Table 7.2 shows that β_{ave} increased by about 1% for the 5° inclination as compared to the 0° inclination. The standard deviation of β_{ave} stayed at similar values for all inclinations. The percent change at 0° inclination in Table 7.2 doesn't match the percent change in Table

Table 7.1: COMPARISON OF ORBIT DETERMINATION ACCURACY FOR BICIRCULAR AND CRTBP HALO ORBITS.

Orbit Name	CRTBP β_{con} (m)	Bicircular change in β_{ave} (%)	Bicircular std. dev. of β_{ave} (% of CRTBP)
LL1A	29700	2.6	13
LL1B	136	2.4	9.0
LL1C	139	6.4	15
LL1D	39.9	-0.41	12
LL1E	106	-16	21
LL1F	158	16	27
LL2A	26500	-0.76	8.5
LL2B	70.6	-0.59	7.6
LL2C	63.1	0.84	9.0
LL2D	56.6	14	37
LL2E	92.6	12	66
LL2F	353	2.7	18

7.1 because the ephemerides for this comparison were only generated using a $\Delta\tau$ of 120° and different Sun-Earth-Moon geometries than before.

Table 7.2: COMPARISON OF ORBIT DETERMINATION ACCURACY FOR DIFFERENT INCLINATIONS OF THE MOON'S ORBIT PLANE.

Inclination (degrees)	change in LL1B β_{con} (% of CRTBP)	change in LL1C β_{con} (% of CRTBP)
0	-2.36	7.52
1	-2.09	7.68
2	-1.82	7.82
5	-0.992	8.22
10	0.486	8.74

7.4.3 Solar Radiation Pressure

With an infinite *a priori* variance on c_R , the resulting standard deviations on the c_R estimates were 0.023 for the spacecraft at $\tau_1 = 0$, and 0.029 for the spacecraft at $\tau_1 = 120$. This seems to be fairly good, since those represent only 1-2% of the total c_R . Even though c_R estimates were fairly tight, β_{ave} went from 112.96 m without SRP to 243.79 m with SRP. When

c_R is not estimated, the effect of SRP on the orbit determination accuracy is negligible. In that case, β_{ave} was 112.93 m.

7.4.4 Final Four-Body Simulation

A final run was performed using the bicircular model that was meant to simulate as close as possible the orbit accuracy attainable in a real operations environment. The first orbit was the LL1B halo at $\tau_1 = 120$ in the inclined inertial bicircular model. $M(t_0)$ and Ω were zero degrees. The second orbit was a lunar orbit propagated using the same model. The initial conditions were obtained using Keplerian elements, which were converted to Cartesian position and velocity. The Keplerian orbit was circular with an altitude of 5,000 km above the Moon. The inclination was 90° and the longitude of the node, argument of perigee, and true anomaly were all zero. Both orbits were computed using SRP. c_R was 1.5 and A/m was $5 \text{ m}^2/1000 \text{ kg}$ for both spacecraft. The interval between observations was six minutes. Consider covariance analysis was performed for a sinusoidal observation error. The modeled amplitude of this error was zero, but a 1σ uncertainty of 50 cm was considered. The range bias and reflectances were estimated along with the positions and velocities of the spacecraft. Observations were generated in two-hour periods which were separated by two-hour periods with no observations. The standard deviation on the range measurement noise was set to 1 m. The fit span was half of a LL1B halo orbit period, or about six days. During that time, the maximum range between the spacecraft was about 64,000 km, and the average range was about 55,000 km. β_{ave} was 24.1 m. The $\bar{\beta}$ for the satellite in the halo was 38.5 m and 9.9 m for the satellite in lunar orbit. Remember that these β values are 3σ . The number of observations during the fit span was 711, with 6 observations blocked by the Moon. The standard deviation for the range bias estimate was 2.7 m. The standard deviations for the reflectance parameters for spacecraft one and two were 0.02 and 0.01 respectively.

The results of this final run showed that Liaison Navigation still performs very well when a fourth body and SRP are added to the force model. In addition, the range bias and reflectance parameters were estimated to good precision. It seems like an average 1σ orbit

determination accuracy on the order of 10 m might be possible for Liaison Navigation in actual mission operations.

7.5 JPL DE405 Ephemeris

To add more realism to the simulations, precise planetary ephemerides from JPL were used to propagate the trajectories using the gravitational force of multiple planets. The JPL planetary ephemerides are provided through an ftp server at

`ftp://ssd.jpl.nasa.gov/pub/eph/export/ascii/`

Greg Lehr, a fellow graduate student at the Colorado Center for Astrodynamics Research, obtained the necessary data files, code, and instructions for its use and devised a method of propagating a trajectory using all of the planets. Of the several ephemeris types available from JPL, the DE405 ephemeris was the one selected for this research (Standish, 1998). DE405 data files provide planetary ephemeris data in the form of coefficients to be used in Chebyshev interpolation. The ephemeris includes positions for each of the nine solar system planets, the Sun, and the Moon in the International Celestial Reference Frame (ICRF, see Ma et al. (1998)) and was created in May-June of 1997. These files are in ASCII format, but they can be converted into binary and the resulting file can then be efficiently queried to provide planetary positions and velocities at the desired epoch. This was done by modifying C code written by Mark Hoffman of NASA's Johnson Space Center in 1998 and obtained from the same ftp server at the address

`ftp://ssd.jpl.nasa.gov/pub/eph/export/C-versions/hoffman/`

Trajectories were propagated in the ICRF inertial frame so that the acceleration due to each of the planetary bodies would be in the form of the two-body equation.

$$\ddot{\mathbf{r}} = -\frac{\mu_{\text{body}} \cdot \mathbf{r}_{\text{body sat}}}{r_{\text{body sat}}^3} \quad (7.16)$$

μ_{body} is the gravitational parameter of the body and $\mathbf{r}_{\text{body sat}}$ is the vector from the center of the body to the spacecraft. The accelerations of all the bodies are vectorially added to give a

single acceleration vector due to gravitational forces. The acceleration due to solar radiation pressure is added to produce the total acceleration.

The first simulations were used to compare orbit determination accuracy of halo orbits generated in the full ephemeris problem to those generated in simplified models. The simulations were performed using two spacecraft on the same halo orbit, which was either LL1B or LL1C. The first spacecraft was located at $\tau_1 = 0^\circ$ and the second at $\tau_2 = 120^\circ$. Quasi-halo orbits were generated using the DE405 ephemeris on a random day of each month in the year 2005 using the multiple shooting differential corrector. Appendix A describes how a halo orbit can be converted from the CRTBP to ICRF (the JPL ephemeris model) to initialize the multiple shooting differential corrector. All orbits were propagated using the Sun, Venus, Earth, the Moon, Mars, Jupiter, Saturn, and SRP. The fit span for these tests was one halo orbit period.

β_{con} was found by averaging all the values of β_{ave} for the twelve epochs. The resulting values of β_{con} are shown in Table 7.3. The orbit determination accuracy appears to get worse when the more accurate force models are used, but still remain in the same order of magnitude. From the standard deviations, it can be seen that the variability due to the geometry of the planetary bodies is quite large.

Table 7.3: COMPARING ORBIT DETERMINATION ACCURACY FOR VARIOUS FORCE MODELS.

Orbit Name	CRTBP $\beta_{con}(m)$	Bicircular $\beta_{con} \pm \text{stdev (m)}$	DE405 Ephemeris $\beta_{con} \pm \text{stdev (m)}$
LL1B	103.19	102.17 \pm 15.0	107.96 \pm 33.8
LL1C	83.62	90.49 \pm 8.1	96.43 \pm 30.5

7.6 Conclusions from the n-body Simulations

When trying to decipher the effect of a fourth body on Liaison Navigation accuracy, the only certain conclusion is that the fourth body introduces large variability in accuracy as the

primary bodies shift positions. On average, the effect of the Sun's gravity on Earth-Moon halo orbits seems to increase the orbit determination error on the order of 3%, while introducing fluctuations with standard deviations between approximately 10 and 40% of the mean. The effect of the inclination between the Sun-Earth orbit plane and the Earth-Moon orbit plane also added about 1% to the orbit determination error. SRP itself does not seem to effect the dynamics enough to cause an increase in the orbit determination error, although the estimation of the reflectance (c_R) caused the error metric to increase.

Upgrading the force model to include precise planetary ephemerides resulted in halo orbits with larger orbit determination errors than the CRTBP and the bicircular model. The accuracy was still on the same order of magnitude.

These small differences between the CRTBP and the bicircular and full ephemeris model show that the CRTBP should be a reasonable approximation when estimating rough orbit determination accuracy.

Chapter 8

Liaison Navigation with Maneuvers and Gravity Fields

This chapter examines the effects of maneuver estimation and gravity field models on Liaison Navigation accuracy in lunar halo orbits. Using the DE405 planetary ephemerides, a constellation was simulated with one spacecraft in a halo orbit and one in lunar orbit. Quasi-periodic libration orbits similar to halo orbits were computed using the multiple shooting differential corrector described in Chapter 7. Impulsive maneuvers were computed to keep the halo orbiter close to a nominal halo trajectory, and these maneuvers were successfully estimated. Finally, the effect of the lunar gravity field was included. Using this realistic force model, it was shown in simulations that the orbit determination accuracy using Liaison Navigation could be on the order of 10 m RSS.

8.1 Lunar Gravity Field

To find the effect of the lunar gravity field on the orbit determination accuracy, A. S. Konopliv's LP100K gravity model was used (Konopliv et al., 2001). This gravity model was determined using data from the Lunar Orbiter, Apollo, Clementine, and Lunar Prospector programs. For a Moon-fixed reference frame, a simplified orientation was simulated where the x axis points directly to the center of the Earth, the z axis points north, perpendicular to the Moon's orbit plane, and the y axis is perpendicular to the x and z axes, approximately in the direction opposite to the Moon's velocity vector. The errors in this orientation should not affect the goal of determining the extent to which the aspherical gravity of the Moon changes the orbit

determination results.

The gravity field is modeled using U , an aspherical potential function excluding the two-body term. For the gravity field formulation, see pp. 508-521 and pp. 553-554 of Vallado and McClain (2001).

$$U = \frac{\mu}{r} \sum_{n=2}^{\infty} \sum_{m=0}^n \left(\frac{R_{\mathcal{L}}}{r} \right)^n P_{n,m}[\sin(\phi)] \{C_{n,m} \cos(m\lambda) + S_{n,m} \sin(m\lambda)\} \quad (8.1)$$

The potential is in terms of the spherical coordinates of radius, r , latitude, ϕ , and longitude, λ .

They are related to the body-fixed, Cartesian position $\mathbf{r} = [x \ y \ z]^T$ in this way:

$$\begin{aligned} r &= \sqrt{x^2 + y^2 + z^2} \\ \phi &= \sin^{-1}(z/r) \\ \lambda &= \tan^{-1}(y/x). \end{aligned} \quad (8.2)$$

In Eqn. 8.1, $R_{\mathcal{L}}$ is the radius of the Moon, μ is the gravitational parameter of the Moon, and n and m are the degree and order of the spherical harmonic model respectively. $C_{n,m}$ and $S_{n,m}$ are coefficients describing the magnitude of the spherical harmonics, and are specific to the gravity field model being used. $P_{n,m}[\sin(\phi)]$ is an associated Legendre function computed using the following recursion, substituting $\sin(\phi)$ for α .

$$\begin{aligned} P_{0,0}[\alpha] &= 1 \\ P_{1,0}[\alpha] &= \alpha = \sin(\phi) \\ P_{1,1}[\alpha] &= \cos(\phi) \\ P_{n,0}[\alpha] &= \frac{(2n-1)\alpha P_{n-1,0}[\alpha] - (n-1)P_{n-2,0}[\alpha]}{n} \quad n \geq 2 \\ P_{n,m}[\alpha] &= P_{n-2,m}[\alpha] + (2n-1)\cos(\phi)P_{n-1,m-1}[\alpha] \quad m \neq 0, m < n \\ P_{n,n}[\alpha] &= (2n-1)\cos(\phi)P_{n-1,m-1}[\alpha] \quad n \neq 0 \end{aligned} \quad (8.3)$$

The coefficients $C_{n,m}$ and $S_{n,m}$ are often available in normalized form. The normalized coefficients, $\bar{C}_{n,m}$ and $\bar{S}_{n,m}$ must be unnormalized using the conversion factor $\Pi_{n,m}$.

$$S_{n,m} = \frac{\bar{S}_{n,m}}{\Pi_{n,m}} \quad C_{n,m} = \frac{\bar{C}_{n,m}}{\Pi_{n,m}} \quad (8.4)$$

the equation for $\Pi_{n,m}$ is

$$\Pi_{n,m} = \sqrt{\frac{(n+m)!}{(n-m)!(2-\delta_{0m})(2n+1)}}. \quad (8.5)$$

δ_{0m} is the Kronecker delta, $\delta_{0m} = 1$ for $m = 0$ and $\delta_{0m} = 0$ for $m \neq 0$.

The acceleration in body-fixed, Cartesian coordinates, \mathbf{a} , is found by taking the gradient of the potential in spherical coordinates and using the chain rule.

$$\mathbf{a} = \left(\frac{\partial r}{\partial \mathbf{r}}\right)^T \frac{\partial U}{\partial r} + \left(\frac{\partial \phi}{\partial \mathbf{r}}\right)^T \frac{\partial U}{\partial \phi} + \left(\frac{\partial \lambda}{\partial \mathbf{r}}\right)^T \frac{\partial U}{\partial \lambda} \quad (8.6)$$

The partials in the equation are:

$$\begin{aligned} \frac{\partial U}{\partial r} &= -\frac{\mu}{r^2} \sum_{n=2}^{\infty} \sum_{m=0}^n \left(\frac{R_{\mathcal{L}}}{r}\right)^n (n+1) P_{n,m}[\sin(\phi)] \\ &\quad \times \{C_{n,m} \cos(m\lambda) + S_{n,m} \sin(m\lambda)\} \end{aligned} \quad (8.7)$$

$$\begin{aligned} \frac{\partial U}{\partial \phi} &= \frac{\mu}{r} \sum_{n=2}^{\infty} \sum_{m=0}^n \left(\frac{R_{\mathcal{L}}}{r}\right)^n \{P_{n,m+1}[\sin(\phi)] - m \tan(\phi) P_{n,m}[\sin(\phi)]\} \\ &\quad \times \{C_{n,m} \cos(m\lambda) + S_{n,m} \sin(m\lambda)\} \end{aligned} \quad (8.8)$$

$$\begin{aligned} \frac{\partial U}{\partial \lambda} &= \frac{\mu}{r} \sum_{n=2}^{\infty} \sum_{m=0}^n \left(\frac{R_{\mathcal{L}}}{r}\right)^n m P_{n,m}[\sin(\phi)] \\ &\quad \times \{S_{n,m} \cos(m\lambda) - C_{n,m} \sin(m\lambda)\} \end{aligned} \quad (8.9)$$

$$\frac{\partial r}{\partial \mathbf{r}} = \begin{bmatrix} \frac{x}{r} & \frac{y}{r} & \frac{z}{r} \end{bmatrix} \quad (8.10)$$

$$\frac{\partial \phi}{\partial \mathbf{r}} = \frac{1}{\sqrt{x^2 + y^2}} \begin{bmatrix} -\frac{xz}{r^2} & -\frac{yz}{r^2} & 1 - \frac{z^2}{r^2} \end{bmatrix} \quad (8.11)$$

$$\frac{\partial \lambda}{\partial \mathbf{r}} = \frac{1}{x^2 + y^2} \begin{bmatrix} -y & x & 0 \end{bmatrix}. \quad (8.12)$$

The equations of motion are integrated in the inertial frame, so the spacecraft state vector must be converted from the inertial frame to the body-fixed frame before computing the accelerations. After computing the body-fixed accelerations, they must be converted back into the inertial frame. Let $[\gamma]_{3 \times 3}$ be a rotation matrix that converts a three-dimensional position or velocity vector from body-centered inertial to body-fixed coordinates.

As mentioned before, γ was created by assuming the Moon's equator was in the Earth-Moon orbit plane, and the lunar prime meridian was on the vector between the center of the

Moon and the center of the Earth. There is about a 6° error in this assumption, but for these simulations it was adequate. γ can also be computed using the Lunar Librations from the DE405 or DE403 ephemerides. These are three Euler angles, which according to Newhall and Williams (1997), are ϕ , the rotation angle along the Earth's mean equator of J2000 from the equinox to the ascending node of the lunar equator, θ , the inclination of the lunar equator with respect to the Earth's mean equator, and ψ , the angle along the lunar equator from the node to a longitude of zero. Figure 8.1 from Newhall and Williams shows the angles graphically. Make sure not to confuse the ϕ mentioned here with the ϕ that represents latitude.

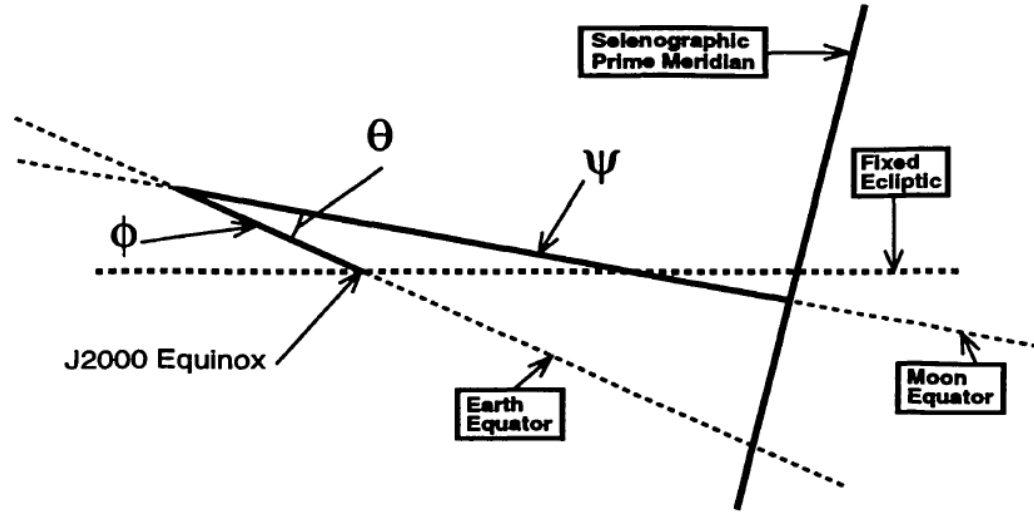


Figure 8.1: The equatorial system in which the Libration Euler angles are defined. (The value of ϕ would be negative as shown.) Credit: Newhall and Williams (1997).

Using these angles from the JPL ephemeris, γ for converting from the Moon-Centered inertial (based on ICRF) to Moon-Centered Moon-Fixed would be:

$$\gamma = \begin{bmatrix} C(\psi)C(\phi) - S(\psi)C(\theta)S(\phi) & C(\psi)S(\phi) + S(\psi)C(\theta)C(\phi) & S(\psi)S(\theta) \\ -S(\psi)C(\phi) - C(\psi)C(\theta)S(\phi) & -S(\psi)S(\phi) + C(\psi)C(\theta)C(\phi) & C(\psi)S(\theta) \\ S(\theta)S(\phi) & -S(\theta)C(\phi) & C(\theta) \end{bmatrix}. \quad (8.13)$$

where C and S represent sine and cosine functions, respectively. These lunar libration angles are used in all the simulations in Chapters 9 and 10.

To include the gravity field in the variational equations used to create matrix A , the partial of \mathbf{a} with respect to \mathbf{r} is computed from pp. 744-746 (see errata) of Vallado and McClain (2001).

$$\begin{aligned} \frac{\partial \mathbf{a}}{\partial \mathbf{r}} &= \left(\frac{\partial r}{\partial \mathbf{r}} \right)^T \frac{\partial}{\partial \mathbf{r}} \frac{\partial U}{\partial r} + \left(\frac{\partial \phi}{\partial \mathbf{r}} \right)^T \frac{\partial}{\partial \mathbf{r}} \frac{\partial U}{\partial \phi} + \left(\frac{\partial \lambda}{\partial \mathbf{r}} \right)^T \frac{\partial}{\partial \mathbf{r}} \frac{\partial U}{\partial \lambda} \\ &+ \frac{\partial}{\partial \mathbf{r}} \left(\frac{\partial r}{\partial \mathbf{r}} \right)^T \frac{\partial U}{\partial r} + \frac{\partial}{\partial \mathbf{r}} \left(\frac{\partial \phi}{\partial \mathbf{r}} \right)^T \frac{\partial U}{\partial \phi} + \frac{\partial}{\partial \mathbf{r}} \left(\frac{\partial \lambda}{\partial \mathbf{r}} \right)^T \frac{\partial U}{\partial \lambda} \end{aligned} \quad (8.14)$$

The first set of new partials are:

$$\frac{\partial}{\partial \mathbf{r}} \frac{\partial U}{\partial r} = \begin{bmatrix} \frac{\partial^2 U}{\partial r^2} & \frac{\partial^2 U}{\partial r \partial \phi} & \frac{\partial^2 U}{\partial r \partial \lambda} \end{bmatrix} \begin{bmatrix} \frac{\partial \mathbf{r}_{r\phi\lambda}}{\partial \mathbf{r}} \end{bmatrix}_{3 \times 3} \quad (8.15)$$

$$\frac{\partial}{\partial \mathbf{r}} \frac{\partial U}{\partial \phi} = \begin{bmatrix} \frac{\partial^2 U}{\partial \phi \partial r} & \frac{\partial^2 U}{\partial \phi^2} & \frac{\partial^2 U}{\partial \phi \partial \lambda} \end{bmatrix} \begin{bmatrix} \frac{\partial \mathbf{r}_{r\phi\lambda}}{\partial \mathbf{r}} \end{bmatrix}_{3 \times 3}, \quad (8.16)$$

$$\frac{\partial}{\partial \mathbf{r}} \frac{\partial U}{\partial \lambda} = \begin{bmatrix} \frac{\partial^2 U}{\partial \lambda \partial r} & \frac{\partial^2 U}{\partial \lambda \partial \phi} & \frac{\partial^2 U}{\partial \lambda^2} \end{bmatrix} \begin{bmatrix} \frac{\partial \mathbf{r}_{r\phi\lambda}}{\partial \mathbf{r}} \end{bmatrix}_{3 \times 3} \quad (8.17)$$

where

$$\begin{bmatrix} \frac{\partial \mathbf{r}_{r\phi\lambda}}{\partial \mathbf{r}} \end{bmatrix}_{3 \times 3} = \begin{bmatrix} \frac{\partial r}{\partial \mathbf{r}} \\ \frac{\partial \phi}{\partial \mathbf{r}} \\ \frac{\partial \lambda}{\partial \mathbf{r}} \end{bmatrix}. \quad (8.18)$$

The partials with respect to spherical coordinates are

$$\begin{aligned} \frac{\partial^2 U}{\partial r^2} &= \frac{\mu}{r^3} \sum_{n=2}^{\infty} \left(\frac{R_{\mathcal{L}}}{r} \right)^n (n+2)(n+1) \sum_{m=0}^n P_{n,m}[\sin(\phi)] \\ &\quad \times \{C_{n,m} \cos(m\lambda) + S_{n,m} \sin(m\lambda)\} \end{aligned} \quad (8.19)$$

$$\begin{aligned} \frac{\partial^2 U}{\partial r \partial \phi} &= \frac{\partial^2 U}{\partial \phi \partial r} \\ &= -\frac{\mu}{r^2} \sum_{n=2}^{\infty} \left(\frac{R_{\mathcal{L}}}{r} \right)^n (n+1) \sum_{m=0}^n \{P_{n,m+1}[\sin(\phi)] - m \tan(\phi) P_{n,m}[\sin(\phi)]\} \\ &\quad \times \{C_{n,m} \cos(m\lambda) + S_{n,m} \sin(m\lambda)\} \end{aligned} \quad (8.20)$$

$$\begin{aligned} \frac{\partial^2 U}{\partial r \partial \lambda} &= \frac{\partial^2 U}{\partial \lambda \partial r} \\ &= -\frac{\mu}{r^2} \sum_{n=2}^{\infty} \left(\frac{R_{\mathcal{L}}}{r} \right)^n (n+1) \sum_{m=0}^n m P_{n,m}[\sin(\phi)] \\ &\quad \times \{S_{n,m} \cos(m\lambda) - C_{n,m} \sin(m\lambda)\} \end{aligned} \quad (8.21)$$

$$\begin{aligned}
\frac{\partial^2 U}{\partial \phi^2} &= \frac{\mu}{r} \sum_{n=2}^{\infty} \left(\frac{R_{\mathcal{L}}}{r} \right)^n \sum_{m=0}^n \\
&\quad \{C_{n,m} \cos(m\lambda) + S_{n,m} \sin(m\lambda)\} \\
&\quad \times \{\tan(\phi) P_{n,m+1}[\sin(\phi)] \\
&\quad + (m^2 \sec^2(\phi) - m \tan^2(\phi) - n(n+1)) P_{n,m}[\sin(\phi)]\}
\end{aligned} \tag{8.22}$$

$$\begin{aligned}
\frac{\partial^2 U}{\partial \phi \partial \lambda} &= \frac{\partial^2 U}{\partial \lambda \partial \phi} \\
&= \frac{\mu}{r} \sum_{n=2}^{\infty} \left(\frac{R_{\mathcal{L}}}{r} \right)^n \sum_{m=0}^n m \{P_{n,m+1}[\sin(\phi)] - m \tan(\phi) P_{n,m}[\sin(\phi)]\} \\
&\quad \times \{S_{n,m} \cos(m\lambda) - C_{n,m} \sin(m\lambda)\}
\end{aligned} \tag{8.23}$$

$$\frac{\partial^2 U}{\partial \lambda^2} = -\frac{\mu}{r} \sum_{n=2}^{\infty} \left(\frac{R_{\mathcal{L}}}{r} \right)^n \sum_{m=0}^n m^2 P_{n,m}[\sin(\phi)] \{C_{n,m} \cos(m\lambda) + S_{n,m} \sin(m\lambda)\}. \tag{8.24}$$

The second derivatives of the spherical coordinates are:

$$\frac{\partial^2 r}{\partial \mathbf{r}^2} = \begin{bmatrix} \frac{1}{r} - \frac{x^2}{r^3} & -\frac{xy}{r^3} & -\frac{xz}{r^3} \\ -\frac{yx}{r^3} & \frac{1}{r} - \frac{y^2}{r^3} & -\frac{yz}{r^3} \\ -\frac{zx}{r^3} & -\frac{zy}{r^3} & \frac{1}{r} - \frac{z^2}{r^3} \end{bmatrix} \tag{8.25}$$

$$\begin{aligned}
\frac{\partial^2 \phi}{\partial \mathbf{r}^2} &= \frac{1}{(x^2 + y^2)^{\frac{3}{2}}} \begin{bmatrix} \frac{zx^2}{r^2} & \frac{zxy}{r^2} & 0 \\ \frac{zxy}{r^2} & \frac{zy^2}{r^2} & 0 \\ \frac{z^2x}{r^2} - x & \frac{z^2y}{r^2} - y & 0 \end{bmatrix} \\
&\quad + \frac{1}{r^2 \sqrt{x^2 + y^2}} \begin{bmatrix} \frac{2zx^2}{r^2} - z & \frac{2xyz}{r^2} & \frac{2xz^2}{r^2} - x \\ \frac{2xyz}{r^2} & \frac{2zy^2}{r^2} - z & \frac{2yz^2}{r^2} - y \\ \frac{2z^2x}{r^2} & \frac{2z^2y}{r^2} & \frac{2z^3}{r^2} - 2z \end{bmatrix}
\end{aligned} \tag{8.26}$$

$$\frac{\partial^2 \lambda}{\partial \mathbf{r}^2} = \frac{1}{(x^2 + y^2)^2} \begin{bmatrix} 2xy & y^2 - x^2 & 0 \\ y^2 - x^2 & -2xy & 0 \\ 0 & 0 & 0 \end{bmatrix}. \tag{8.27}$$

Once the matrix $\frac{\partial \mathbf{a}}{\partial \mathbf{r}}$ is computed, it must be rotated from the body-fixed frame to the inertial frame before being added to the rest of the A matrix. This is done with the rotation γ described

earlier. The inertial version of $\frac{\partial \mathbf{a}}{\partial \mathbf{r}}$ is

$$\left[\frac{\partial \mathbf{a}}{\partial \mathbf{r}_{inertial}} \right]_{3 \times 3} = \gamma^T \left[\frac{\partial \mathbf{a}}{\partial \mathbf{r}} \right]_{3 \times 3} \gamma. \quad (8.28)$$

$\frac{\partial \mathbf{a}}{\partial \mathbf{r}_{inertial}}$ can then be added to the proper portion of the A matrix.

8.2 Impulsive Maneuvers

A simple way of estimating impulsive maneuvers is by using a sequential filter such as the Extended Kalman Filter (EKF) and resetting the covariance after each maneuver. Using the EKF to estimate maneuvers is discussed in Chapter 9, but the batch processor was used for the simulations in this chapter. For the batch processor, estimating impulsive maneuvers, which are an instantaneous change in velocity or ΔV , is more difficult. The easiest method is to start a new orbit fit after every ΔV . Both the position and velocity are estimated immediately after the ΔV , and the fit span extends until the next ΔV . For Liaison Navigation, this can be a problem because stationkeeping in a halo orbit requires around three ΔV s per halo orbit period, but good orbit determination accuracy necessitates fit spans of an entire halo orbit period. This problem can be avoided by estimating only the velocity change at the time of a maneuver and assuming that there was no change in position at that time.

As a general example, the state vector to be estimated using orbit determination could contain the initial position and velocity and the ΔV as shown:

$$\mathbf{X} = [x \ y \ z \ \dot{x} \ \dot{y} \ \dot{z} \ \Delta V_x \ \Delta V_y \ \Delta V_z]^T. \quad (8.29)$$

When propagating the state vector, the derivatives of the ΔV parameters are zero, since they are constant. The A matrix used to propagate the state transition matrix would be of the following form:

$$A = \begin{bmatrix} B_{6 \times 6} & D_{6 \times 3} \\ C_{3 \times 6} & E_{3 \times 3} \end{bmatrix}. \quad (8.30)$$

The submatrix B consists of the same 6×6 A matrix that would be obtained if the ΔV were not being estimated. Partial derivatives of the time rate of change of the ΔV parameters are

contained in submatrices C and E . Since the $\Delta\mathbf{V}$ parameters are constants, their time derivatives are zero and C and E are always null matrices. Submatrix D contains partial derivatives that describe how the velocity and acceleration of the spacecraft are affected by the $\Delta\mathbf{V}$ parameters. Since the $\Delta\mathbf{V}$ is modeled as an impulsive maneuver, or an instantaneous change in velocity, D is a null matrix as well. So A is not changed by the $\Delta\mathbf{V}$ estimation, except to add zeros.

The change occurs in the state transition matrix itself, not its derivative. First, the trajectory is integrated up to the epoch of the $\Delta\mathbf{V}$. Then the $\Delta\mathbf{V}$ is applied to the velocity, and then the trajectory is integrated from that point onward. The state transition matrix looks like this:

$$\Phi(t, t_k) = \begin{bmatrix} \frac{\partial \mathbf{R}}{\partial \mathbf{R}_k} & \frac{\partial \mathbf{R}}{\partial \mathbf{V}_k} & \frac{\partial \mathbf{R}}{\partial \Delta \mathbf{V}} \\ \frac{\partial \mathbf{V}}{\partial \mathbf{R}_k} & \frac{\partial \mathbf{V}}{\partial \mathbf{V}_k} & \frac{\partial \mathbf{V}}{\partial \Delta \mathbf{V}} \\ \frac{\partial \Delta \mathbf{V}}{\partial \mathbf{R}_k} & \frac{\partial \Delta \mathbf{V}}{\partial \mathbf{V}_k} & \frac{\partial \Delta \mathbf{V}}{\partial \Delta \mathbf{V}} \end{bmatrix}. \quad (8.31)$$

\mathbf{R} is the position vector, \mathbf{V} is the velocity vector, and $\Delta\mathbf{V}$ is the impulsive maneuver. Since changes in the initial position or velocity do not affect the $\Delta\mathbf{V}$, $\frac{\partial \Delta \mathbf{V}}{\partial \mathbf{R}_k}$ and $\frac{\partial \Delta \mathbf{V}}{\partial \mathbf{V}_k}$ are always 3×3 null matrices. Since the $\Delta\mathbf{V}$ is a constant, $\frac{\partial \Delta \mathbf{V}}{\partial \Delta \mathbf{V}}$ is always a 3×3 identity matrix. $\frac{\partial \mathbf{R}}{\partial \Delta \mathbf{V}}$ and $\frac{\partial \mathbf{V}}{\partial \Delta \mathbf{V}}$ are 3×3 null matrices until the maneuver takes place, at which time $\frac{\partial \mathbf{V}}{\partial \Delta \mathbf{V}}$ is initialized to a 3×3 identity matrix.

In this way, only the $\Delta\mathbf{V}$ s are estimated, and the spacecraft position along the trajectory is continuous. This means that the fit span can include several maneuvers and be long enough for Liaison Navigation to be useful.

8.3 Simulation Results

All the orbit determination simulations were conducted using two spacecraft that tracked each other continuously, unless the Earth or the Moon blocked the line of sight (LOS) vector. Range observations were generated from the ephemeris files every six minutes. These observations were used to generate the \tilde{H}_i matrices. The state transition matrices were obtained from

the ephemeris files for each orbit. The information matrix, H^TWH , was computed, and the covariance matrix was used to compute navigation error metrics. The range observations had an added white noise component with a standard deviation of 1 m.

The purpose of this simulation was two-fold. One goal was to ascertain the orbit determination accuracy when estimating multiple ΔV 's and the other was to see if Liaison Navigation could provide orbit determination accurate enough to compute stationkeeping maneuvers on a perpetual basis. To do this, a constellation of two spacecraft was simulated. The first spacecraft was in a halo orbit about the lunar L_1 point and the second was in a lunar orbit with a periapsis altitude of 100 km, an apoapsis radius of 10,000 km, and an inclination of 90° . The argument of periapsis, longitude of the ascending node, and the true anomaly were all 0° . These elements were converted into a position and velocity and added to the position and velocity of the Moon in the ICRF. All orbits were propagated using the Sun, Venus, Earth, the Moon, Mars, Jupiter, Saturn, and SRP. The orbits were split into segments such that there would be 2, 3, 4, or 6 segments per halo orbit period. The beginning of each segment is called a patch point. Figure 8.2 shows a diagram of the various orbits used in the simulation.

The first orbit computed is the nominal halo orbit. The nominal halo orbit was generated with the multiple shooting differential corrector and spanned four revolutions. It was stored in the form of positions and velocities at each patch point. Next, the position, velocity, and reflectance of the first patch point on the nominal halo was perturbed using random numbers. This was the first state on the “true” halo. The first segment of the true halo was then propagated until the second patch point was reached. The first segment of the lunar orbit was propagated as well. Then spacecraft-to-spacecraft range observations were generated with added white noise. After enough segments of observations were generated, the states for both the halo and lunar orbiter were estimated using orbit determination. The fit span was anywhere from 2 to 6 segments. The new estimated orbit was used to update the positions, velocities, and maneuvers at each of the “estimated orbit” patch points in the fit span.

Since some of these fits spanned as much as 12 days, a separate lunar orbiter state was

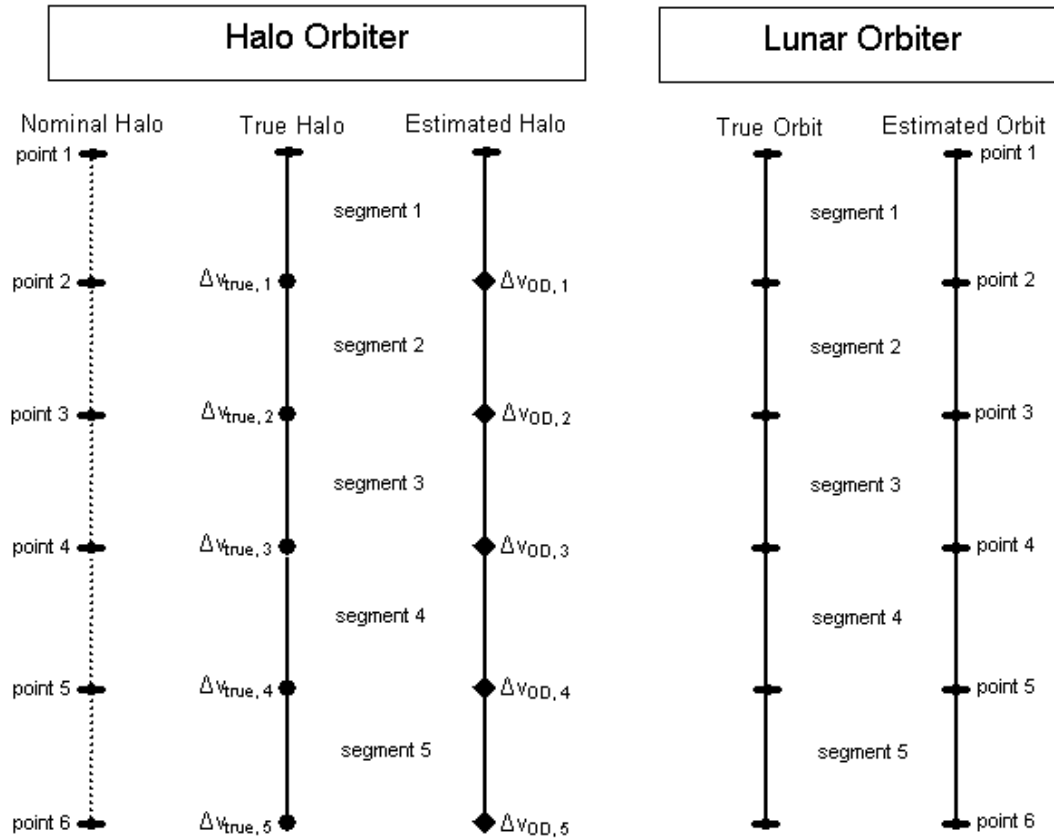


Figure 8.2: Simulation orbit and maneuver timeline.

estimated at the beginning of each segment to avoid divergence. In other words, the lunar orbiter was treated as a completely different spacecraft for each segment. Otherwise, small perturbations in the initial state of the lunar orbiter resulted in large deviations from the nominal trajectory after 12 days, and that led to problems converging on a solution.

The estimated orbits were then used to compute a stationkeeping maneuver, ΔV_{OD} . A differential corrector was used to target the next patch point on the nominal orbit starting from the latest position on the estimated orbit. This maneuver strategy is what was used for the Genesis mission (Williams et al., 2000). It was assumed that the execution of the stationkeeping maneuver would not be performed perfectly, so the true maneuver, ΔV_{true} , had a random 3% error added to each component. After the true and estimated maneuvers were added to the

proper states, the next segments of the true orbits were generated and the process repeated.

When initializing the simulation, orbit determination could not be performed until enough segments of observations were generated. In the meantime, the estimated orbits were found by adding random perturbations to the true orbits. Since the statistics of these perturbations would usually not match with the statistics of orbit estimates obtained from orbit determination, it took some time until the effects of the orbit determination accuracy would be fully felt in the stationkeeping results and the constellation would reach a steady state. Out of the four halo orbit periods in the simulations, only the results from the last two were tabulated. Various fit span lengths, segment lengths, and halo orbits were simulated. For each case, ten runs were performed and the results averaged and shown in Table 8.1.

Table 8.1: AVERAGED SIMULATION RESULTS FOR THE LIAISON NAVIGATION STATIONKEEPING STUDY.

Halo name	Segments per halo period	Segments per fit span	Average 3D, 1 σ OD accuracy (m)	Average distance from nominal halo at patch points (km)	Sum of the ΔV 's (m/s)
LL1B	2	2	2.220	21.26	1.696
	3	2	11.13	1.292	0.106
	3	3	5.565	1.233	0.103
	4	2	14.42	0.629	0.063
	4	3	9.116	0.671	0.067
	4	4	7.238	0.663	0.067
	6	3	19.40	0.350	0.040
	6	4	15.10	0.353	0.040
	6	5	11.19	0.352	0.039
	6	6	9.751	0.351	0.039
LL1C	2	2	1.792	4.204	0.375
	3	2	10.05	1.076	0.071
	3	3	4.974	1.083	0.073
	4	2	19.51	0.565	0.048
	4	3	7.837	0.577	0.048
	4	4	6.019	0.576	0.048
	6	3	26.48	0.332	0.031
	6	4	15.92	0.335	0.031
	6	5	10.76	0.334	0.030
	6	6	7.117	0.331	0.031

It can be seen from Table 8.1 that the distance from the nominal halo orbit to the real halo orbit is mainly affected by the frequency of the maneuvers, or the number of segments per halo orbit period. The same is true with the ΔV budget, or the sum of the ΔV 's. This means that none of the orbit determination errors were large enough to cause significant problems when computing the stationkeeping maneuver. However, the orbit determination accuracy was better when there were less maneuvers. For fits spanning an entire LL1B halo orbit period, the orbit determination accuracy increased from about 2 meters when there were two segments in the fit span to around 9 meters when there were six segments. This is because a new lunar orbiter state must be estimated for each segment, and a ΔV must be estimated for each interior patch point. The more segments there are in the fit, the more parameters to estimate.

Finally, the same simulation was repeated, but the orbits were propagated using the LP100K gravity field. The field was truncated to speed up computation time. The true halo orbit was generated using a 2×2 field, and the true lunar orbit used an 8×8 gravity field. Figure 8.3 compares the results for runs with different lunar gravity models. The bars labeled “Point Mass” show the results when the Moon was modeled only as a point mass. These are the same numbers as those in Table 8.1. The bars labeled “GravField” show results when the lunar gravity field was used in propagating the orbit, but not in the state transition matrix. The bars labeled “STM with GravField” show data obtained when the gravity field was used in both the orbit and state transition matrix. The orbit determination accuracy for “STM with GravField” was not significantly different than “Point Mass.” For “GravField,” there were large increases in error for some of the fit and segment types.

8.4 Conclusion

Modeling and estimating the stationkeeping maneuvers was found to be very useful in extending the length of the halo orbit fit span. This led to increased accuracy in the orbit estimates. Also, it was found that Liaison Navigation could be used as a tool both for autonomous orbit determination and for autonomous computation of stationkeeping maneuvers. Finally,

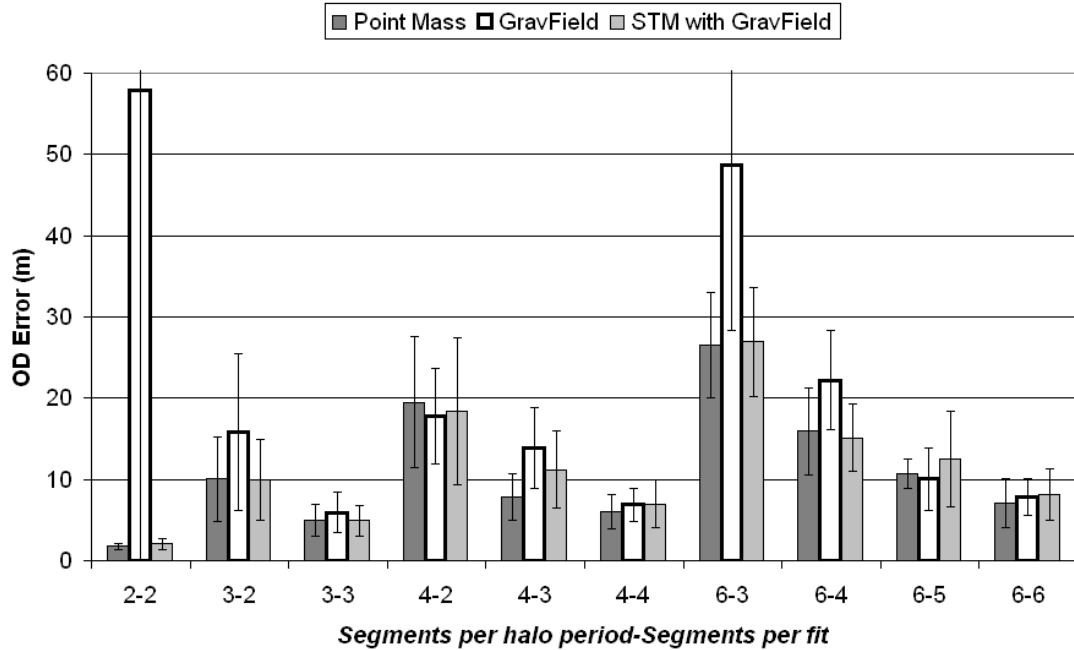


Figure 8.3: Orbit determination accuracy from the LL1C-Moon ΔV study when using a Lunar gravity field.

including the effects of the asymmetric gravity field of the Moon resulted in a highly accurate force model. Simulations using a truncated lunar gravity field resulted in 1σ orbit determination accuracy less than 10 m for a two-spacecraft constellation at the Moon, but this does not account for errors in the gravity field model itself.

Chapters 9 and 10 will show simulation results with gravity modeling errors in an EKF. The EKF can be used to estimate maneuver errors more gracefully than the method for the batch processor shown in this chapter.

Chapter 9

A Lunar Navigation and Communication Mission

To fulfill the mandate to return to the Moon outlined in the Vision for Space Exploration, NASA conducted the Exploration Systems Architecture Study (ESAS, November 2005). The ESAS final report issued in November 2005 lists ten sample landing sites for manned missions to the Moon. Six out of these ten sites are at the poles, limb, or far side of the Moon where direct communication links to Earth are impossible. Because of this, the ESAS study concluded that an orbital communication and navigation (comm/nav) infrastructure would be needed. According to ESAS, this constellation would be used to help provide support for orbit insertion, landing, surface operations, and Earth transit. It would be used for intervehicle and Moon-to-Earth communications as well as to provide tracking data for navigation. It should be designed to evolve seamlessly as the requirements and numbers of user spacecraft and missions increase. The constellation should also be “capable of uninterrupted, multi-year activity” in addition to being reliable and redundant.

Several concepts for a lunar comm/nav constellation have already been proposed. Farquhar (1970) proposed using halo orbits at Earth-Moon L_2 (LL_2) to provide communications for the far side of the Moon during the Apollo Program. Although the idea was not used for Apollo, a communications relay satellite at LL_2 could provide communications for the far side and south pole and enable better determination of the far side gravity field.

Spacecraft placed in halo orbits have several identified advantages and disadvantages when compared to spacecraft placed in low lunar orbits. Carpenter et al. (2004) showed that

a few halo orbiters could provide the same coverage as a larger number of lunar orbiters. Halo orbiters have longer communication contacts with the surface, meaning that there are fewer times when it is necessary to break contact with one spacecraft to acquire the signal of another. Tracking antenna pointing is easier because of the slower apparent motion of a halo orbiter when viewed from the lunar surface. Halo orbiters are illuminated by the Sun more than typical low lunar orbiters. Hill et al. (2006b) show that halo orbits are more fuel-efficient than low lunar orbits, meaning they require less energy to reach from Earth and they can have lower stationkeeping costs. A disadvantage is that the link distance from the Moon to a halo orbiter is larger than for a lunar orbiter. A disadvantage for many lunar comm/nav concepts is that they require several launches to build the constellations and a lot of expensive Deep Space Network (DSN) time to track each spacecraft.

This chapter presents a new method for the construction and operation of a comm/nav infrastructure at the Moon that takes advantage of all of the benefits of halo orbits and reduces the costs of establishing and maintaining that infrastructure. This constellation design was described by Hill et al. (2006b). The operational costs of the comm/nav constellation may be substantially reduced using Liaison Navigation. The costs of establishing the constellation may be substantially reduced using “Ballistic Lunar Transfers” (BLT). BLT’s are low-energy trajectories spacecraft may use to transfer from the Earth to the Moon for considerably less ΔV than conventional transfers. This chapter will show how the constellation orbits were chosen and summarize the mission design and the results of the Liaison Navigation simulations of the mission.

9.1 Mission Concept

The mission to the Moon would involve two spacecraft: one called “Snoopy” in a halo orbit at LL_2 and another called “Woodstock” in a low lunar, polar orbit. Snoopy would be able to provide communications coverage for the south pole of the Moon for extended periods of time. Woodstock would provide intermittent coverage for the lunar poles as well as other areas

of the Moon's surface. Both could be used as tracking stations for spacecraft orbiting, landing, or roving at the Moon.

During the validation phase of the mission, Snoopy would be used to track Woodstock, alone and in conjunction with the DSN. This tracking data could be processed on the ground to determine lunar gravity field parameters. During this time, orbit determination and maneuvers for both spacecraft would be computed both on the ground, and on Snoopy using Liaison Navigation. If Liaison Navigation provides adequate results in operation and proves to be a reliable method of performing autonomous orbit determination, Snoopy could be switched into autonomous navigation mode for the rest of the mission.

During the operational phase of the mission, Snoopy could be used to relay communications from the lunar far side and south pole to Earth. Woodstock could also be used to receive faint signals from rovers or landers on the Moon and relay them to Earth, either directly or through Snoopy. During periods when Snoopy is below the horizon at the south pole, Woodstock would provide periodic coverage since it passes over the poles once an orbit. Snoopy and Woodstock could be used to track other lunar spacecraft or to broadcast navigation signals. In the future, another halo orbiter could join Snoopy to provide continuous coverage to the lunar south pole using the method outlined by Grebow et al. (2006). With even more spacecraft, continuous coverage for the entire lunar far side and polar regions is possible using a constellation similar to that proposed by Carpenter et al. (2004).

9.1.1 Ballistic Lunar Transfers

The lunar comm/nav spacecraft would be placed into their mission orbits using a single launch vehicle. A low-energy BLT (Parker and Lo, 2005; Parker, 2006) would be used to transfer the two spacecraft together to a halo orbit about LL_2 .

The launch vehicle would propel the two spacecraft on the lunar transfer trajectory, and they would ballistically arrive at the lunar halo orbit, requiring no insertion maneuver at all. The entire transfer requires much less energy than a conventional direct transfer, allowing payloads

to be 25% to 33% larger in mass, depending on the launch vehicle (Hill et al., 2006b).

After the two spacecraft reach the halo orbit, Woodstock would separate and follow a low-energy transfer down to the Moon. Departing from the halo orbit only requires a few meters per second ΔV . However, there is a required injection maneuver to capture into the low lunar orbit. In the future, if the constellation is to be reconfigured, Snoopy may follow similar low-energy transfers to new mission orbits (Folta and Vaughn, 2004).

9.2 LL₂ Halo Orbit Selection (Snoopy)

There is a full continuum of orbits in the family of halo orbits about LL₂, and the optimum halo was selected for Snoopy using seven requirements. In addition to satisfying the needs of the current mission, the halo orbit was chosen so that in the future, a second spacecraft could be placed at LL₂ to provide continuous coverage of the south pole and other missions orbiting the Moon. The requirements are:

- (1) The LL₂ halo orbit should be above 10° elevation over the entire lunar south pole region (80° to 90°S) for the estimated length of the first lunar sorties, or seven continuous days of each halo orbit period.
- (2) With all other requirements satisfied, the LL₂ halo orbit stationkeeping costs should be minimized.
- (3) With all other requirements satisfied, the LL₂ halo orbit determination error should be minimized.
- (4) With all other requirements satisfied, the percentage of the time that Woodstock is not visible from either the Earth or Snoopy should be minimized, and tracking data should be obtainable over the entire lunar far side.
- (5) With a future second spacecraft in the halo orbit, at least one of the two halo orbiters should be above 10° elevation over the entire lunar south pole region at all times.

- (6) Either the two halo orbiters mentioned above, or Earth-based tracking stations should be able to track spacecraft in any lunar orbit at all times.
- (7) It should be possible for Woodstock to separate from Snoopy and, using only a very small perturbation to the trajectory, travel to a point where an insertion into the proper lunar orbit can be performed.

To verify compliance with the requirements, quantifiable metrics were computed for each of them.

9.2.1 Requirement 1

The LL_2 halo orbit should be above 10° elevation over the entire lunar south pole region (80° to 90° S) for the estimated length of the first lunar sorties, or seven continuous days of each halo orbit period. To verify compliance with this requirement, several locations in the lunar south pole regions were selected. For each of those surface locations, the azimuth and elevation of a halo orbiter were computed over an entire halo orbit period for a wide spectrum of LL_2 halo orbits generated in the CRTBP. The amount of time that a halo orbiter was above 10° was computed as a metric to verify that requirement 1 was met. Figure 9.1 shows the results at 80° S 0° E, which was the worst case. The Jacobi constant (Murray and Dermott, 1999) for the halo orbits, C , is computed using the following equation:

$$C = -V^2 + x^2 + y^2 + 2 \left(\frac{1-\mu}{r_1} + \frac{\mu}{r_2} \right). \quad (9.1)$$

V is the velocity in the rotating frame. Requirement 1 was satisfied for all halo orbits with Jacobi constants less than about 3.085.

9.2.2 Requirements 2 and 3

With all other requirements satisfied, the LL_2 halo orbit stationkeeping costs and the LL_2 halo orbit determination error should be minimized. To verify compliance with requirements 2 and 3, nominal trajectories were computed for a spectrum of halo orbits. The altitude of the

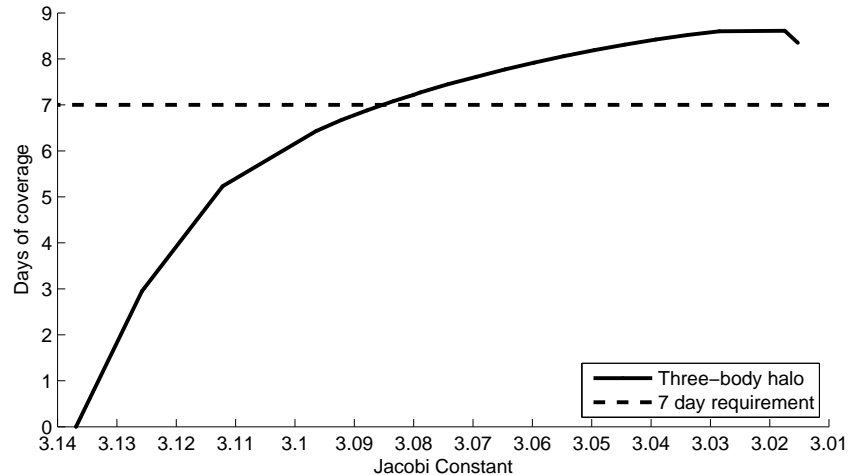


Figure 9.1: Number of days a halo orbiter is visible above 10° elevation at $80^\circ\text{S } 0^\circ\text{E}$

lunar orbit had not yet been selected, so a nominal polar, lunar orbit at 100 km altitude was computed. The orbit propagation included SRP and the gravitational forces of the Moon, Sun, Venus, Earth, Mars, Jupiter, and Saturn, computed using the JPL DE405 ephemeris. The nominal halo orbit was generated with a multiple shooting differential corrector (Howell and Pernicka, 1988; Wilson) and spanned four revolutions. A “true” orbit for each spacecraft was generated by randomly perturbing the initial conditions. Spacecraft-to-spacecraft range observations were generated and corrupted using white noise with a standard deviation of 1 m. The states for both the halo and lunar orbiter were estimated with a batch processor and Liaison Navigation. The results from Liaison Navigation were used to compute the stationkeeping maneuvers (SKM) required to keep Snoopy near the nominal halo orbit. For each halo orbit generated with a different Jacobi constant, ten simulations were performed. The orbit determination and SKM results were averaged and displayed in Figure 9.2. The orbit determination error shown is an average for the two spacecraft.

The orbit determination results show some noise because the data points are really an average of only 10 runs with random initial conditions. But the general trend is for the orbit determination error to trend upwards below a Jacobi constant of about 3.08. The stationkeeping

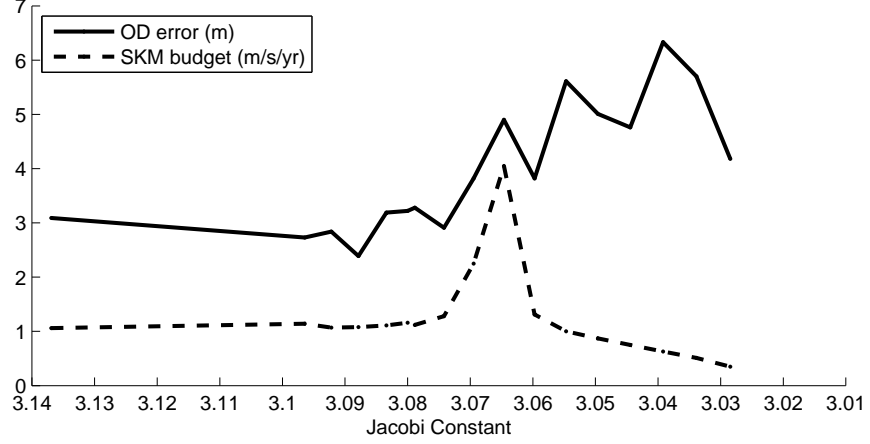


Figure 9.2: Orbit Determination and Stationkeeping simulation results.

results show that there is a large spike in the stationkeeping budget at a Jacobi constant of about 3.065. This spike is centered on the Jacobi constant for halo orbits with a period in 2:1 resonance with the Moon’s orbital period about the Earth. If this spike is avoided, the rest of the halo orbits have a yearly stationkeeping budget of about 1 m/s.

9.2.3 Requirement 4

With all other requirements satisfied, the percentage of the time that Woodstock is not visible from either the Earth or Snoopy should be minimized, and tracking data should be obtainable over the entire lunar far side. Compliance with this requirement was verified by simulating Snoopy’s halo orbit and Woodstock’s orbit in the CRTBP. A circular, polar, lunar orbit with an altitude of 100 km was used for Woodstock. About every six minutes for 4 months, if either Snoopy or the Earth was able to see and track Woodstock, then Woodstock’s latitude and longitude was computed and tallied in bins that were 10° of latitude by 10° of longitude. The density of tracking coverage for bin i, j , $D_{i,j}$, was computed using the number of tracking points tallied in the bin, $T_{i,j}$, the total number of points T_{total} , and the area of that bin on the surface of the Moon, $A_{i,j}$:

$$D_{i,j} = \frac{T_{i,j}/T_{total}}{A_{i,j}}. \quad (9.2)$$

The results were plotted and had a marked correlation between the position of Snoopy on its halo orbit, τ , and the Moon-fixed longitude of the ascending node of Woodstock's orbit, Ω . τ is a non-geometric angle similar to mean anomaly for halo orbits and is described in Chapter 3. For LL_2 halo orbits, τ is zero when the spacecraft is at the point closest to the Moon and goes through 360° in one halo orbit period. The value of Ω goes through 360° every time the Moon rotates in inertial space (≈ 28 days). Since the periods of the LL_2 halo orbits are approximately half of the rotation period of the Moon, there is a near 2:1 resonance between τ and Ω . The relationship between the two parameters can be quantified with the angle δ which is computed in the following way:

$$\delta = \tau - 2\Omega. \quad (9.3)$$

The value of δ for halo orbits only changes slowly, the rate of change depending on how close the halo orbit is to a 2:1 resonance with the Moon's orbit. By picking the right δ , the total Snoopy-Woodstock tracking gaps on the far side can be minimized. The total tracking gaps are computed as a percentage:

$$\text{Total tracking gaps} = \frac{\sum_i \sum_j T_{i,j}}{T_{total}} \times 100\%. \quad (9.4)$$

Figure 9.3 shows the best and worst that could be achieved for each halo orbit.

If the best case δ can be achieved, the gaps in tracking data are relatively low until the Jacobi constant goes below about 3.04.

9.2.4 Requirement 5

With a future second spacecraft in the halo orbit, at least one of the two halo orbiters should be above 10° elevation over the entire lunar south pole region at all times. To verify compliance with this requirement, the elevation was checked again at various south pole locations using two halo orbiters on the same halo orbit, phased 180° apart. The orbit propagation included SRP and the gravitational force of the Moon, the Sun, Venus, Earth, Mars, Jupiter, and Saturn computed using the JPL DE405 ephemeris. Each halo orbit was generated with a

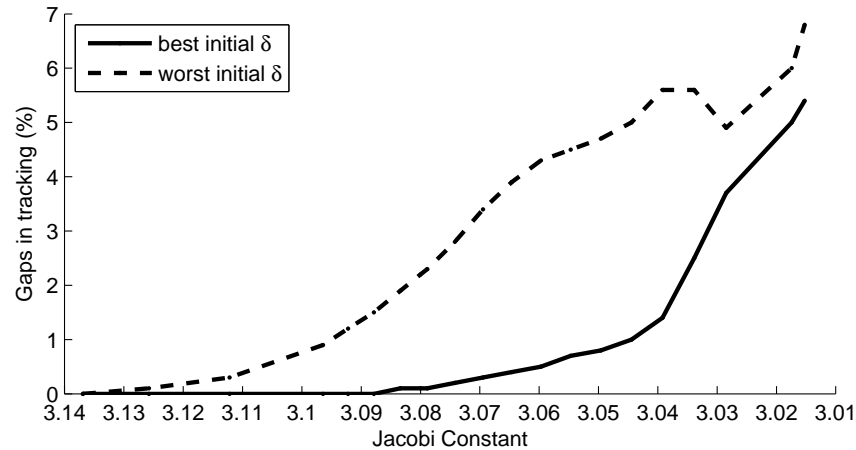


Figure 9.3: Gaps in tracking as a percentage of the time when Woodstock is not visible from Earth or Snoopy.

multiple shooting differential corrector (Howell and Pernicka, 1988; Wilson) and spanned five halo orbit periods. Gaps in tracking at a surface location occurred when both of the halo orbiters were below 10° elevation. In order for requirement 5 to be met, the tracking gaps had to occur 0% of the time. Figure 9.4 shows the tracking gaps for each halo orbit at the worst case surface location. The results are also shown when the minimum elevation requirement is increased to 15° . This coverage requirement was satisfied for all halo orbits with Jacobi Constants less than about 3.085.

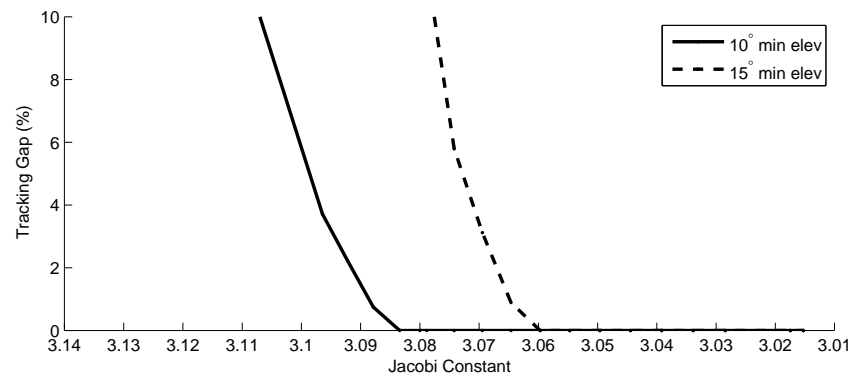


Figure 9.4: Tracking gaps as a percentage of the time neither of two halo orbiters is visible at the worst case surface locations.

9.2.5 Requirement 6

Either the two halo orbiters mentioned in requirement 5, or Earth-based tracking stations should be able to track spacecraft in any lunar orbit at all times. This requirement was checked in the same way as requirement 4, except that a second halo orbiter was simulated 180° away from the first. The percentage of the time when Woodstock could be tracked by neither the two halo orbiters nor the Earth is plotted in Figure 9.5. Complete coverage of Woodstock is possible with Earth tracking and two LL_2 halo orbiters except for orbits with Jacobi constants less than about 3.04.

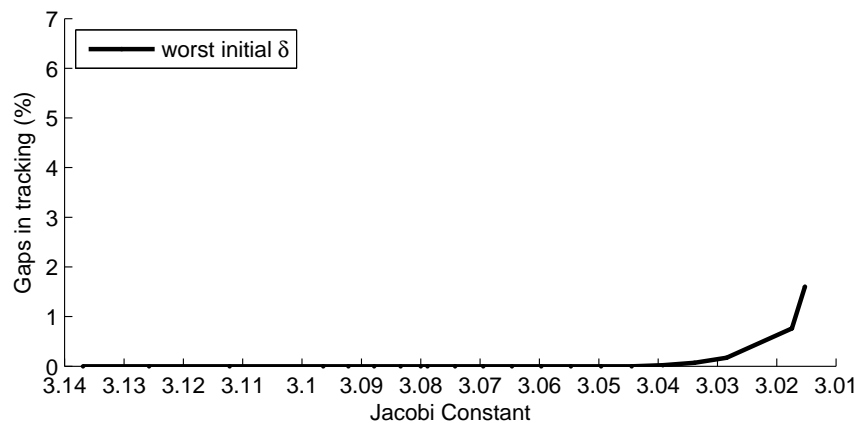


Figure 9.5: Gaps in tracking as a percentage of the time when Woodstock is not visible from Earth or two halo orbiters.

9.2.6 Requirement 7

It should be possible for Woodstock to separate from Snoopy and, using only a very small perturbation to the trajectory, travel to a point where an insertion into the proper lunar orbit can be performed. This requirement was examined by Jeffrey Parker, who found that the requirement would be met for halo orbits with Jacobi constant values in the ranges of 3.05–3.06, 3.11–3.13, and 3.14–3.15 (Hill et al., 2006b).

9.2.7 Selected Halo Orbit

An orbit selection plot was created and shown in Figure 9.6. Regions with high and low Jacobi constant were eliminated because they didn't provide sufficient coverage of the South Pole or Woodstock, respectively. The orbit selected had a Jacobi constant of 3.0597 because it provided excellent coverage of the south pole with two halo orbiters. At least one of the two halo orbiters would be above 15° elevation at all times. With Jacobi constants higher than this, the stationkeeping costs increased. Orbits with Jacobi constants lower than 3.06 had increasing error in the orbit determination and increasing tracking gaps in the Snoopy-Woodstock coverage. The Jacobi constant for this orbit also falls in the acceptable range mentioned for requirement 7.

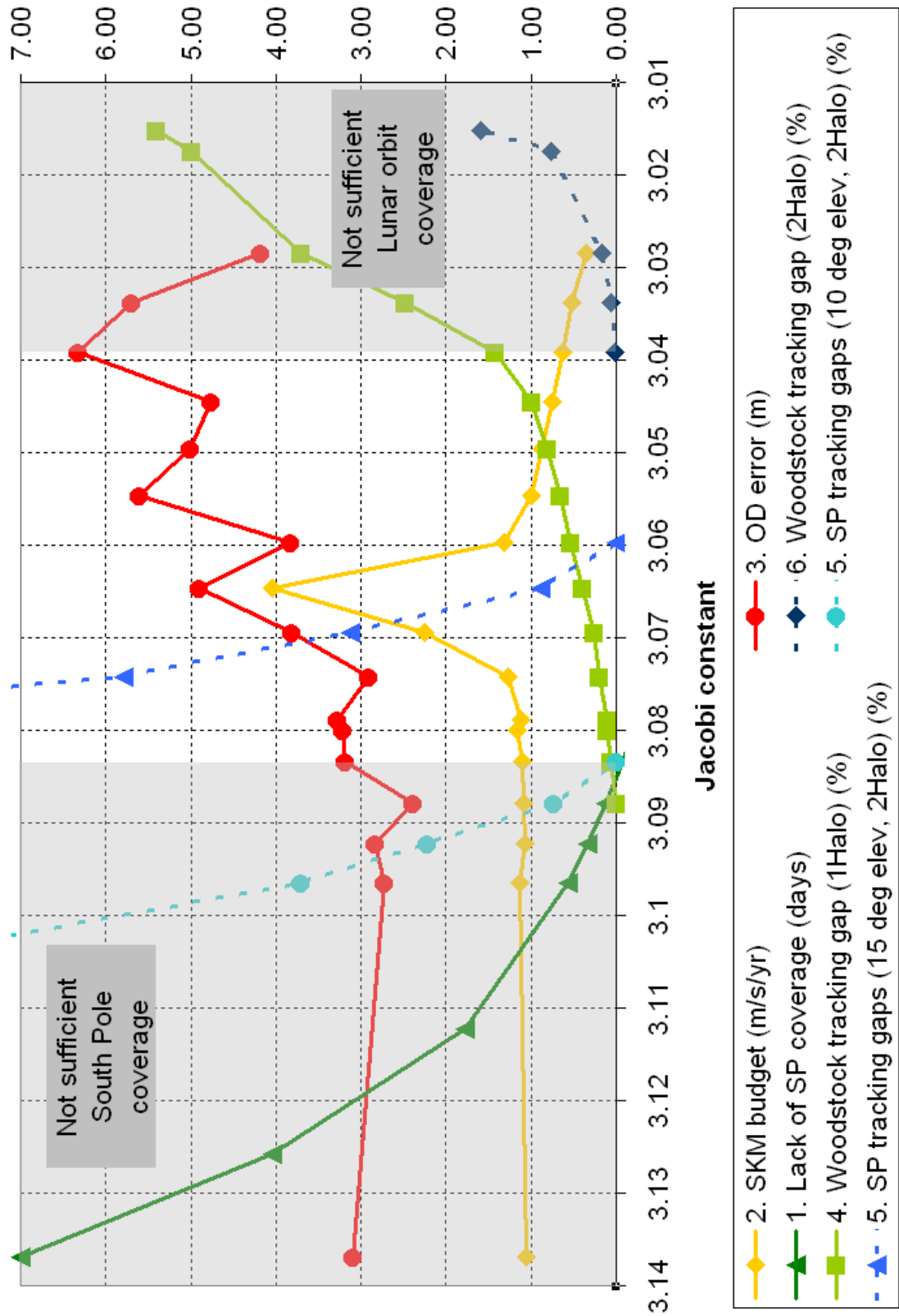


Figure 9.6: Plot used to select the halo orbit for Snoopy. The numbers in the legend correspond to the orbit selection requirement number. The legend also shows the vertical axis units for each metric. The chosen orbit has a Jacobi constant of about 3.06.

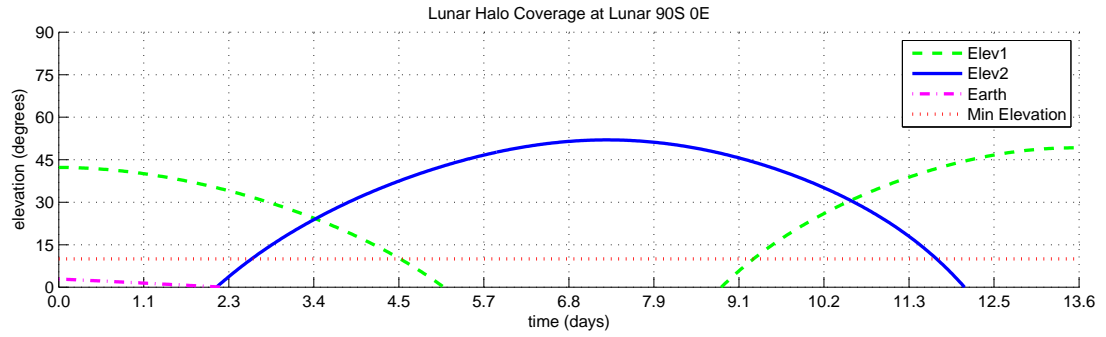


Figure 9.7: Elevation of two halo orbiters (Elev1, Elev2) and the Earth at the lunar south pole. The spacecraft are in the orbit selected for Snoopy, 180° apart. Orbits were propagated using the full ephemeris and SRP.

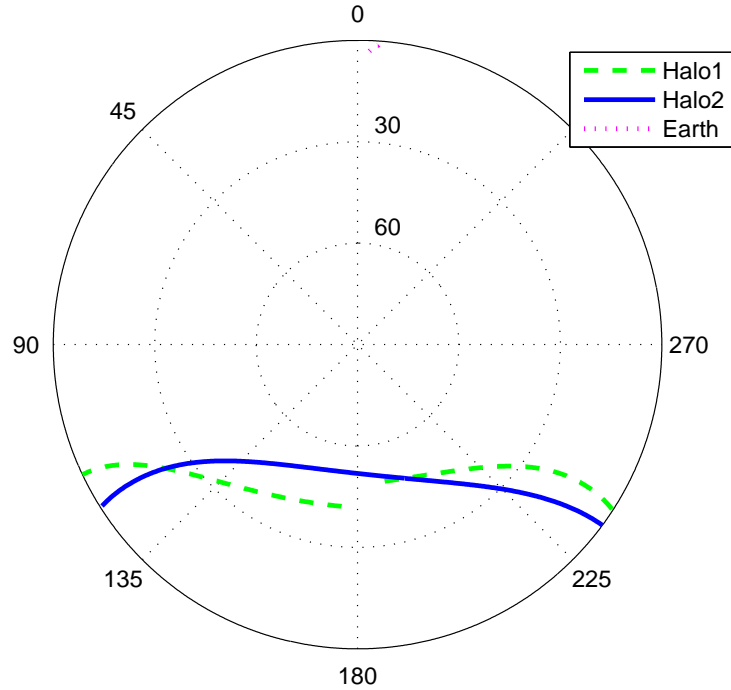


Figure 9.8: Skyplot of two halo orbiters at the lunar south pole. The spacecraft are in the orbit selected for Snoopy, 180° apart. Orbits were propagated using the full ephemeris and SRP.

For the selected orbit, Figure 9.7 shows the elevation at the south pole of two halo orbiters on Snoopy's nominal orbit over one halo period. Earth rises above 0° briefly at the beginning of the period. Figure 9.8 shows how the paths of the two halo orbiters across the sky would look

to an observer at the south pole. Figure 9.9 shows that for one halo orbiter, the Earth/Snoopy-Woodstock tracking gaps can be minimized by targeting a certain value of δ when inserting Woodstock into its lunar orbit. Figures 9.10 and 9.11 show maps of the density of Woodstock's tracking coverage over the entire lunar surface, centered on the far side.

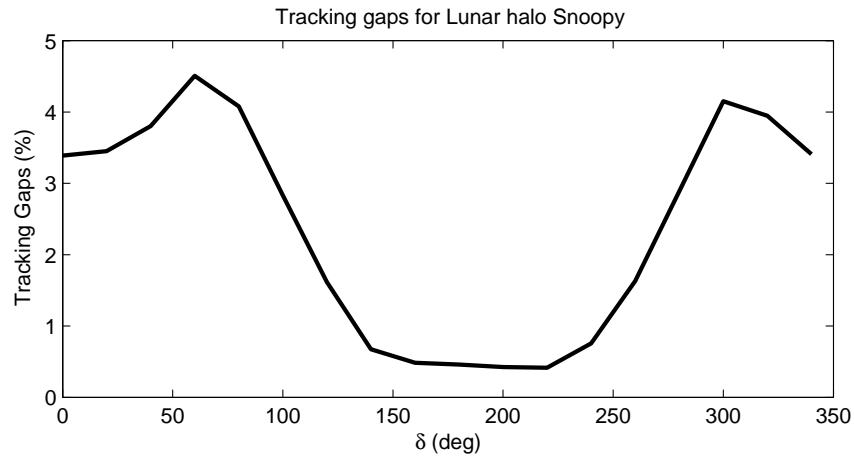


Figure 9.9: Earth/Snoopy-Woodstock tracking gaps (% of points).

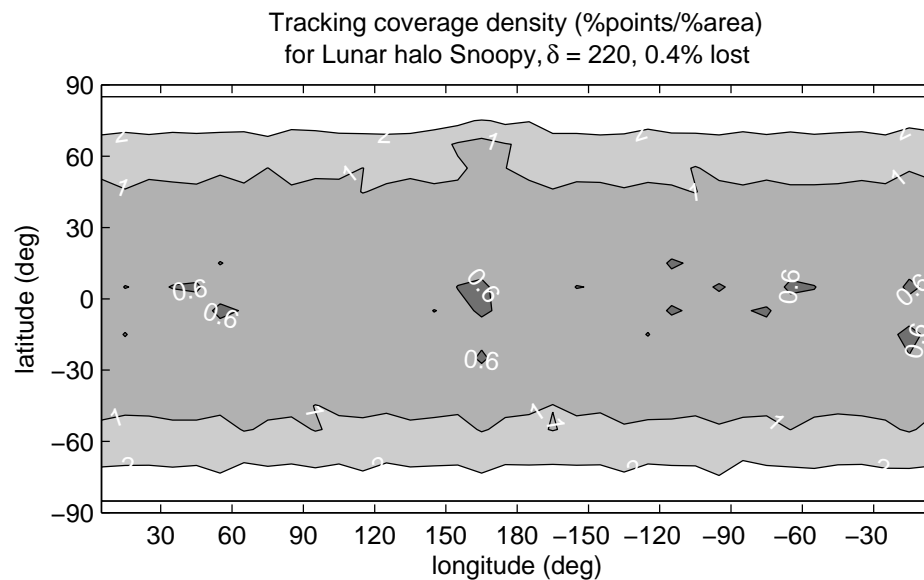


Figure 9.10: Earth/Snoopy-Woodstock tracking coverage density (% points/% area) at the optimum value of $\delta = 220^\circ$.

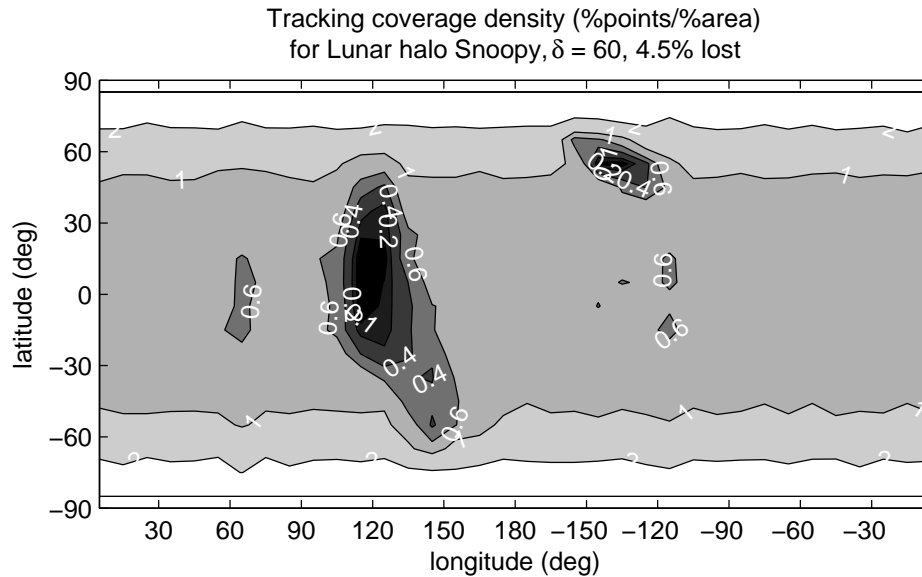


Figure 9.11: Earth/Snoopy-Woodstock tracking coverage density (% points/% area) at the worst case value of $\delta = 60^\circ$.

The density is expressed as the percentage of tracking data points in a latitude-longitude bin divided by the percentage of the lunar surface area contained in the bin. So, if the tracking coverage were uniform over the entire lunar surface, the density would be 1. For areas with less than the average coverage, the tracking density is less than 1, and it is greater than 1 for areas with more than the average tracking coverage. Because Woodstock is in a polar orbit, it passes over the poles once every orbit. The density is the highest in the high latitudes, and the density thins toward the equator. Figure 9.10 shows the tracking coverage density for an optimum value of δ and represents about the most uniform coverage possible for this polar orbit. Figure 9.11 shows how the orbit geometry at the worst value of δ can lead to holes in coverage over the lunar far side surface. The regions with low tracking coverage density, represented by the dark shading, are areas where neither the Earth nor Snoopy can see Woodstock in its orbit. The orbits were propagated using the full ephemeris and the LP100K lunar gravity field up to degree and order 30.

9.3 Low Lunar Orbit Selection (Woodstock)

The requirements established for selecting the low lunar orbit for Woodstock are:

- (1) The low lunar orbit should pass over the lunar South Pole.
- (2) Woodstock's orbit should be as low as possible for good estimation of the lunar far side gravity field.
- (3) The percentage of the time that Woodstock is not visible from either the Earth or Snoopy should be minimized, and tracking data should be obtainable over the entire lunar far side.
- (4) The stationkeeping costs of the lunar orbit should be minimized.

Requirement 1 can be satisfied if Woodstock is in a polar orbit, or an orbit with an inclination close to 90° . Requirement 3 is satisfied with the proper selection of δ as described in the Snoopy orbit selection process. To find a lunar orbit that satisfies requirements 2 and 4, Nicole Demandante performed a lunar orbit study, as shown in Hill et al. (2006b). The orbit chosen for Woodstock has an apoapsis altitude of 95 km and a periapsis altitude of 50 km. This orbit was relatively stable when compared to other similar low lunar orbits, and thus stationkeeping costs would be reduced.

Woodstock's descent from the halo orbit to the low lunar orbit was designed by Jeffrey Parker and explained in Hill et al. (2006b). Woodstock would take a 28-day transfer down to its low-lunar orbit injection point approximately 189 km above the lunar surface at an inclination of approximately 90° . The departure can be performed with a minimal maneuver, although it does require a large maneuver to become captured in its low-lunar orbit. Since 50 km is very close to the lunar surface, Woodstock was instead placed into a higher parking orbit before descending down to its final orbit. The parking orbit was polar with an altitude of 189×2000 km, requiring an insertion maneuver of 397.4 m/s. Additional maneuvers would be performed later to reduce Woodstock's orbit to a 50×95 km altitude.

Jeffery Parker also designed the launch and Ballistic Lunar Transfer that would be used to get to the Moon. The details of the mission, as shown in Hill et al. (2006b), are:

- Launch from a LEO parking orbit at an altitude of 534 ± 10 km at an inclination of $28.5^\circ \pm 0.02$ on September 20, 2011 at 2:00 am using approximately 3.11 km/s of ΔV .
- The transfer to the lunar halo orbit requires approximately 114 days and no deterministic maneuvers. There is a lunar flyby with a closest approach of about 22,474 km (altitude of 20,736 km) on September 22, 2011 at 8:05 am. The launch cost may be further reduced by approaching closer to the Moon.
- The lunar halo insertion requires no deterministic maneuver and occurs on approximately January 12, 2012.
- The sum total of the patch point ΔV 's, which theoretically may be removed, is equal to about 4.5 mm/s, including the entire transfer and eight halo revolutions.
- On February 2, 2012 at 6:39 am, Woodstock performs a 1.18 m/s maneuver to depart Snoopy.
- On February 5, 2012 at 12:53 am, Woodstock performs a 0.97 m/s maneuver to adjust its descent trajectory.
- On March 1, 2012 at 6:18 am, Woodstock arrives at perilune at an altitude of 189 km and an inclination of 90° , after following its descent for about 28 days.
- Woodstock performs a 397.4 m/s maneuver to enter its temporary 189×2000 km orbit, followed by additional maneuvers totaling 287.9 m/s to lower the orbit to a final 50×95 km polar orbit with periapsis near the lunar equator.

9.4 Spacecraft Design

The link distance between Snoopy and Woodstock is large, approximately 75,000 km, which means that each spacecraft requires high-gain communication antennas. These highly

directional antennas would need good pointing accuracy and the ability to point in many different directions. Because of these pointing requirements, both Snoopy and Woodstock would need to be three-axis stabilized spacecraft. The spacecraft would also need precise clocks to perform autonomous orbit determination or generate stable navigation beacons. Snoopy would be assigned to perform the onboard orbit determination for both spacecraft, although Woodstock could compute its own estimates as a cross-check. Both spacecraft would need photovoltaics to generate electricity. Snoopy's halo orbit is ideal for solar power since no eclipses occur in the trajectory generated, although that does not rule out the possibility that an eclipse could occur in a different time period.

A simple link budget analysis was done using Ka-band radio frequencies. Woodstock would have one high-gain antenna (41 dB with 1.3° beamwidth) for communicating with Earth and Snoopy. It would also have omni-directional antennas for communicating with assets on the lunar surface. Snoopy would have two high-gain antennas. One of these would have a narrow beam (1° beamwidth) to send and receive data to Earth at a high rate. The other would have a somewhat wider beam (3° beamwidth) so that the beam could cover the entire lunar surface while pointing at the center. Each spacecraft could receive data from the Moon at a rate of 18 Mbps using the narrow-beam antennas. This would require tracking the lunar surface transmitter with the antennas. A data rate of 2 Mbps would be possible with the wide beam antennas, which would not need to track the transmitter on the surface. These link budgets were made using a 1 m dish on the lunar surface with 10 W of transmit power.

Woodstock would need a large propulsion system for the lunar orbit insertion maneuver and the lunar SKM's. Snoopy's propulsion system could be much smaller due to the low cost of SKM's in the halo orbit. Table 9.1 shows estimated ΔV budgets for both spacecraft. Snoopy's SKM budget as computed from the Liaison Navigation simulation was only 16.2 cm/s per year, which is amazingly small. The longest nominal halo trajectory generated using the DE405 ephemeris was about a year. Since it is difficult to patch together different nominal trajectories without a ΔV , there would be at least one planned ΔV of about 1 m/s in a year. That

would mean that the SKM budget for Snoopy would be at least 1 m/s per year. The Woodstock Trajectory Correction Maneuver (TCM) budget was based on the Lunar Reconnaissance Orbiter (LRO) estimates (Folta, 2004). The SKM budget for Woodstock (56 m/s per year) was much less than that estimated for LRO (140 m/s per year) due to Woodstock's eccentric orbit and higher apoapsis.

Table 9.1: STATIONKEEPING BUDGETS FOR BOTH SPACECRAFT IN TERMS OF ΔV

Spacecraft	Maneuver Type	ΔV
Snoopy	SKM	16.2 cm/s/yr
Woodstock	TCM	75 m/s
Woodstock	Descent from Halo	1.9 m/s
Woodstock	Orbit Insertion	397.4 m/s
Woodstock	Orbit Lowering	287.9 m/s
Woodstock	SKM	56.3 m/s/yr

9.5 Liaison Navigation performance

To simulate the on-board performance of Liaison Navigation, there were three types of orbits generated. The first was a nominal halo orbit generated at LL_2 using the multiple shooting differential corrector mentioned before. The nominal orbit is divided into four segments per halo orbit period. The state at the beginning of each segment is called a patch point. At the time of each patch point, Snoopy is never exactly on this nominal orbit, so a SKM must be performed to get Snoopy closer to the nominal orbit. This was done with the method used for the Genesis Mission (Williams et al., 2000). A differential corrector is used to target the next patch point using the best estimate of the current position. The current velocity is corrected until the trajectory hits the next patch point. The SKM is performed to get Snoopy's velocity to match the corrected velocity. In this simulation, maneuver execution errors were modeled in each component direction as normally distributed with a standard deviation equal to 5% of the maneuver magnitude in that component.

Starting with an initial deviation from the nominal halo orbit, a true orbit was generated

for Snoopy. Snoopy was modeled as a 1000 kg spherical spacecraft with a cross-sectional area of 5 m². The JPL DE405 ephemeris was used to find the positions of the Earth, Moon, Sun, Venus, Mars, Jupiter and Saturn. Each planet was modeled as a point mass. The Moon's gravity field (up to degree and order 2) was modeled using the LP100K gravity model. SRP was modeled using an umbra/penumbra eclipse model with the solar pressure computed based on the distance from the Sun. A true orbit was generated for Woodstock in the same way, except the lunar gravity field parameters up to degree and order 20 were used. After generating the true orbits, range observations were computed every 60 seconds and normally distributed noise with a standard deviation of 1 m was applied. These observations were used to estimate the states of the spacecraft. The initial states for the estimated orbits were computed with randomly generated position, velocity, and reflectance errors. The initial position errors had a 1σ in each component of 100 m and 10 m for Snoopy and Woodstock, respectively. The velocity errors were about 6×10^{-4} m/s and 6×10^{-5} m/s, respectively.

A real-time state update would provide the spacecraft with accurate orbit determination quickly so that the spacecraft could be used as navigation support for other spacecraft. An Extended Kalman Filter (EKF) provides real-time state estimates, so it was ideal for this purpose. A summary of the EKF comes from Tapley et al. (2004) and uses their notation. A simplified spacecraft state could consist of three position and velocity components for each spacecraft. For two spacecraft, the state vector would be written:

$$\mathbf{X} = [x_1 \ y_1 \ z_1 \ \dot{x}_1 \ \dot{y}_1 \ \dot{z}_1 \ x_2 \ y_2 \ z_2 \ \dot{x}_2 \ \dot{y}_2 \ \dot{z}_2]^T,$$

where the subscripts denote the spacecraft number. The equations of motion are written:

$$\dot{\mathbf{X}} = F(\mathbf{X}, t), \quad \mathbf{X}_i \equiv \mathbf{X}(t_i). \quad (9.5)$$

An observation at time t_i is denoted by \mathbf{Y}_i , and the state deviation and observation residuals are written:

$$\mathbf{x}(t) = \mathbf{X}(t) - \mathbf{X}^*(t), \quad \mathbf{y}(t) = \mathbf{Y}(t) - \mathbf{Y}^*(t), \quad (9.6)$$

where \mathbf{X}^* is the reference solution, or the “best guess” orbit, and \mathbf{Y}^* is an observation computed using the reference solution. The observations can be related to the state with the \tilde{H} matrix, which is

$$\tilde{H}_i = \left[\frac{\partial G}{\partial \mathbf{X}} \right]_i^* \quad (9.7)$$

G is a function that computes observations from a state vector in the following way:

$$\mathbf{Y}_i = G(\mathbf{X}_i, t_i) + \epsilon_i, \quad (9.8)$$

where ϵ_i is the observation error. If crosslink range, ρ , is the observation type then \tilde{H}_i is of the form:

$$\tilde{H}_i = \left[\begin{array}{cccccccccccc} \frac{\partial \rho}{\partial x_1} & \frac{\partial \rho}{\partial y_1} & \frac{\partial \rho}{\partial z_1} & \frac{\partial \rho}{\partial \dot{x}_1} & \frac{\partial \rho}{\partial \dot{y}_1} & \frac{\partial \rho}{\partial \dot{z}_1} & \frac{\partial \rho}{\partial x_2} & \frac{\partial \rho}{\partial y_2} & \frac{\partial \rho}{\partial z_2} & \frac{\partial \rho}{\partial \dot{x}_2} & \frac{\partial \rho}{\partial \dot{y}_2} & \frac{\partial \rho}{\partial \dot{z}_2} \end{array} \right]_i \quad (9.9)$$

State deviations at time t may be mapped back to an epoch, t_k , with the state transition matrix Φ in the following way:

$$\mathbf{x}(t) = \Phi(t, t_k) \mathbf{x}_k. \quad (9.10)$$

The state transition matrix is integrated along with the state using the following relation:

$$\dot{\Phi}(t, t_k) = A(t) \Phi(t, t_k) \quad \text{where} \quad A(t) = \frac{\partial F(\mathbf{X}^*, t)}{\partial \mathbf{X}(t)} \quad \text{and is of the form:} \quad (9.11)$$

$$A = \left[\begin{array}{cccccc} \frac{\partial \dot{x}_1}{\partial x_1} & \frac{\partial \dot{x}_1}{\partial y_1} & \frac{\partial \dot{x}_1}{\partial z_1} & \cdots & \frac{\partial \dot{x}_1}{\partial \dot{z}_2} \\ \frac{\partial \dot{y}_1}{\partial x_1} & \frac{\partial \dot{y}_1}{\partial y_1} & \frac{\partial \dot{y}_1}{\partial z_1} & & \\ \frac{\partial \dot{z}_1}{\partial x_1} & \frac{\partial \dot{z}_1}{\partial y_1} & \frac{\partial \dot{z}_1}{\partial z_1} & & \vdots \\ \vdots & & & \ddots & \\ \frac{\partial \ddot{z}_2}{\partial x_1} & & \cdots & & \frac{\partial \ddot{z}_2}{\partial \dot{z}_2} \end{array} \right]^* \quad (9.12)$$

If it is assumed that the observation errors can be modeled as white noise, and the standard deviation in the observation noise is denoted σ_ρ , a weighting matrix R^{-1} can be used to weight the observations, where

$$R = \sigma_\rho^2. \quad (9.13)$$

The EKF requires an *a priori* covariance, P_0 . The EKF works by propagating the state deviation and the covariance at time $k - 1$ to the next observation epoch, k , using the “time update” equations:

$$\bar{P}_k = \Phi(t_k, t_{k-1})P_{k-1}\Phi^T(t_k, t_{k-1}). \quad (9.14)$$

P_{k-1} is the covariance matrix at the time of the last observation, and \bar{P}_k is the same matrix propagated forward to the time of the next observation. The state and covariance are updated with the observation at time k using the “measurement update” equations:

$$K_k = \bar{P}_k \tilde{H}_k^T \left[\tilde{H}_k \bar{P}_k \tilde{H}_k^T + R \right]^{-1} \quad (9.15)$$

$$\hat{\mathbf{x}}_k = K_k \left[\mathbf{y}_k - \tilde{H}_k \bar{\mathbf{x}}_k \right]. \quad (9.16)$$

$$P_k = \left[I - K_k \tilde{H}_k \right] \bar{P}_k \quad (9.17)$$

The state is then updated with $\hat{\mathbf{x}}$.

$$\mathbf{X}_{new}^* = \mathbf{X}^* + \hat{\mathbf{x}} \quad (9.18)$$

The newly updated state is then propagated forward to the time of the next observation and the time and measurement update is repeated. At each time update, the estimation errors represented in the covariance matrix become smaller and smaller. This can cause the Kalman gain, K_k , to become so small that the observations are effectively ignored. This is called filter saturation. To prevent this, state noise compensation can be used to inflate the covariance matrix slightly, which increases the Kalman gain and assures that the recent observations are not ignored. State noise compensation is performed by adding a covariance matrix due to process noise to the time update of the estimation error covariance matrix. This matrix can be derived by assuming that the spacecraft velocity is constant between measurement times, where Δt is the interval between measurements (Tapley et al., 2004). A variance for the process noise, $\sigma_{a,i}^2$ is assumed for each spacecraft. Here, $i = 1, 2$ represents the two spacecraft. This 6×6 matrix is added to the position and velocity portions of the estimation error covariance matrix for each

spacecraft:

$$\begin{bmatrix} \frac{\Delta t^3}{3}\sigma_{a,i}^2 & 0 & 0 & \frac{\Delta t^2}{2}\sigma_{a,i}^2 & 0 & 0 \\ 0 & \frac{\Delta t^3}{3}\sigma_{a,i}^2 & 0 & 0 & \frac{\Delta t^2}{2}\sigma_{a,i}^2 & 0 \\ 0 & 0 & \frac{\Delta t^3}{3}\sigma_{a,i}^2 & 0 & 0 & \frac{\Delta t^2}{2}\sigma_{a,i}^2 \\ \frac{\Delta t^2}{2}\sigma_{a,i}^2 & 0 & 0 & \Delta t\sigma_{a,i}^2 & 0 & 0 \\ 0 & \frac{\Delta t^2}{2}\sigma_{a,i}^2 & 0 & 0 & \Delta t\sigma_{a,i}^2 & 0 \\ 0 & 0 & \frac{\Delta t^2}{2}\sigma_{a,i}^2 & 0 & 0 & \Delta t\sigma_{a,i}^2 \end{bmatrix} \quad (9.19)$$

The values of $\sigma_{a,i}$ were tuned until they resulted in a realistic covariance matrix and low state errors. State errors were computed by differencing the estimated state, \mathbf{X}_{new}^* , with the true state at each measurement time.

The state estimates from the EKF were used to compute the SKM for both spacecraft.

Woodstock's SKM's were designed to restore the periapsis and apoapsis altitudes to 50 and 95 km, respectively, and also had 5% errors in execution. The velocity portion of the covariance matrix was increased accordingly after each maneuver, so the EKF could be used properly to estimate the true velocity after the maneuver. Snoopy's SKM's were performed four times per halo orbit period as described earlier, and Woodstock's SKM's were performed once per halo period, halfway between two of the Snoopy SKM's. A range bias was added to the measurements, and the bias was successfully estimated to within several meters.

Because Snoopy and Woodstock would need to perform communication relay duties as well as provide tracking support to user spacecraft, they would not be available to track each other all the time. Figure 9.12 shows how each antenna on the spacecraft would be used over a day. The times shown are Central Standard Time, to coincide with "Houston Time" that manned missions would be using. This schedule limits the time when Snoopy and Woodstock can track each other, however, the schedule for each day was shifted in ten minute increments (to a maximum of one hour) to synchronize the Snoopy-Woodstock tracking with the times that Woodstock was not out of sight behind the Moon. During the eight-hour working day of a

manned outpost on the Moon, Snoopy provides constant two-way communication relay services to Earth, with the exception of a one hour break at lunch to track Woodstock. The schedule would change when Snoopy is not visible from the lunar surface, with Woodstock providing the relay intermittently as it passes overhead (not shown).

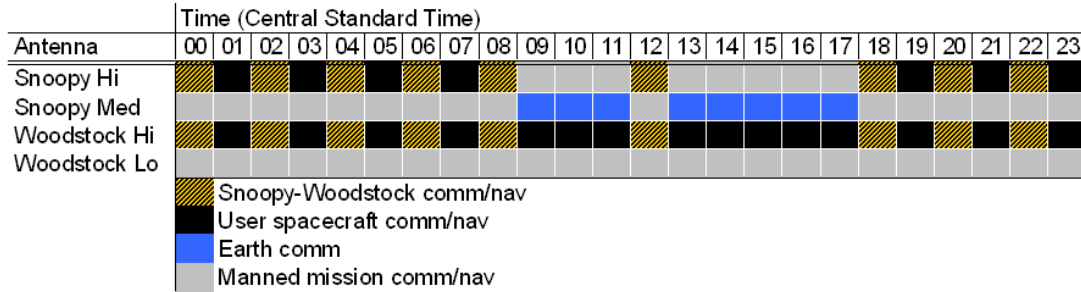


Figure 9.12: Daily schedule of comm/nav support for Snoopy and Woodstock

To make the simulation more realistic, the force model used in the EKF was different than the force model used to generate the true orbits. In the EKF, the two types of unmodeled accelerations came in the form of gravity model errors and radiation model errors.

A clone of the gravity field was created by randomly perturbing the gravity field coefficients using the covariance matrix for the LP100K model. The vector \mathbf{c}_{grav} includes all of the normalized coefficients in the gravity model and the corresponding covariance matrix is P_{grav} . A clone of the gravity model can be created by factoring P_{grav} :

$$P_{grav} = S^T S. \quad (9.20)$$

S is upper triangular and can be computed using Cholesky Decomposition. If e is a vector of normally distributed random numbers with zero mean and variance 1, a clone of the gravity model, \mathbf{c}_{clone} would be

$$\mathbf{c}_{clone} = \mathbf{c}_{grav} + S^T e. \quad (9.21)$$

Errors in the clone are described by P_{grav} . With the EKF, the reflectance for each spacecraft was estimated to much less than 1%. However, since an error in radiation modeling was desired,

it was simulated by fixing errors in the reflectance for each spacecraft and not estimating the true reflectance. The reflectance errors were designed so that they resulted in acceleration errors on the order of $1 \times 10^{-9} \text{ m/s}^2$, which is a typical magnitude for interplanetary missions.

Figures 9.13 through 9.16 show the resulting accuracy of the EKF over two halo periods starting on 5 March 2012. The RSS for the position error (computed after day 8) for Snoopy was 78 m and the velocity error was 0.4 mm/s. For Woodstock, the RSS for the position error was 6.9 m and 6 mm/s for velocity. It took about 3-6 days for Snoopy's orbit estimate to converge. Woodstock's orbit converged in about 2 days. Even with initial position and velocity errors 100 times larger, the estimates still converged in the same time frame.

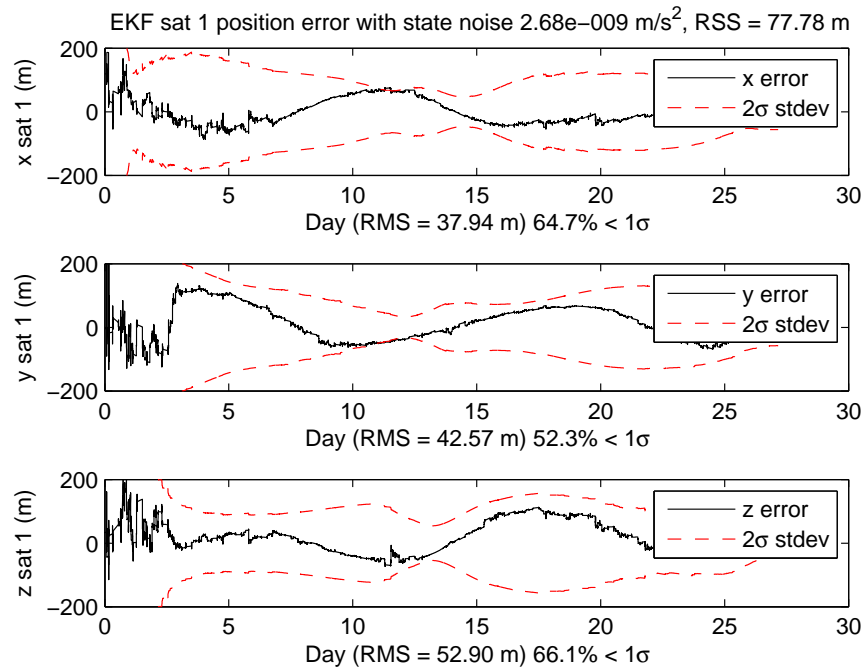


Figure 9.13: Snoopy position accuracy using the EKF.

9.6 Navigation Support

Snoopy and Woodstock could be used as mobile tracking stations after using Liaison Navigation to determine their orbit states. Snoopy and Woodstock could track other spacecraft

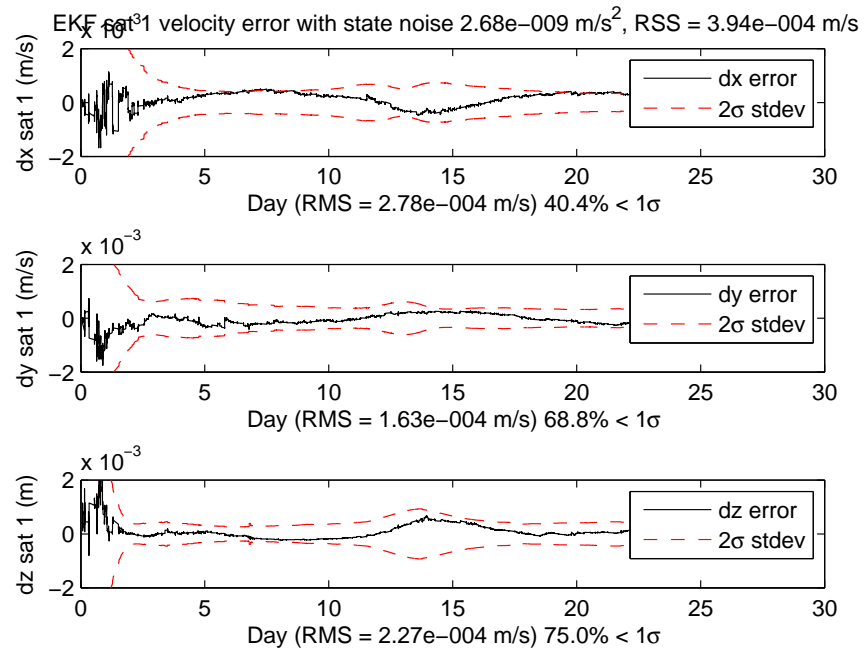


Figure 9.14: Snoopy velocity accuracy using the EKF.

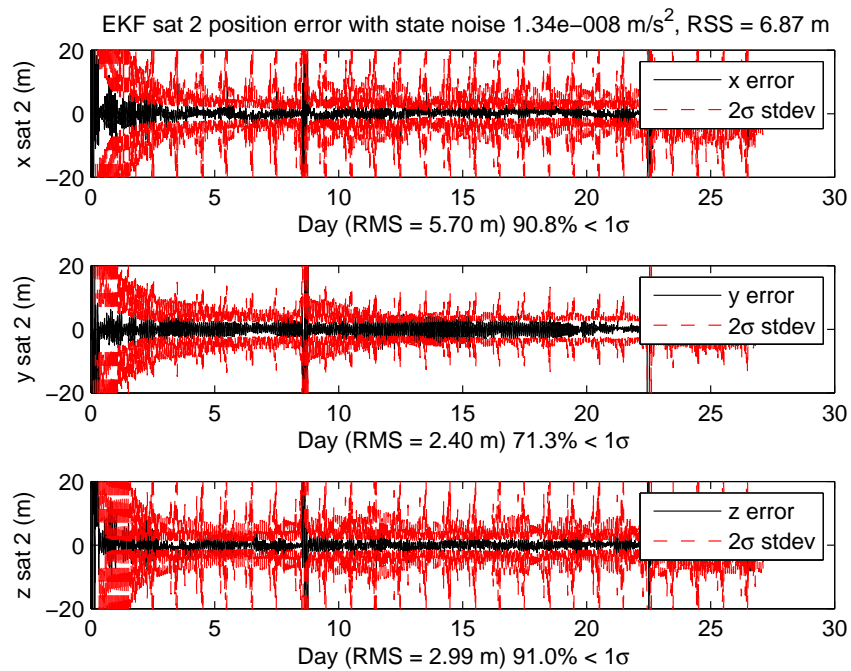


Figure 9.15: Woodstock position accuracy using the EKF.

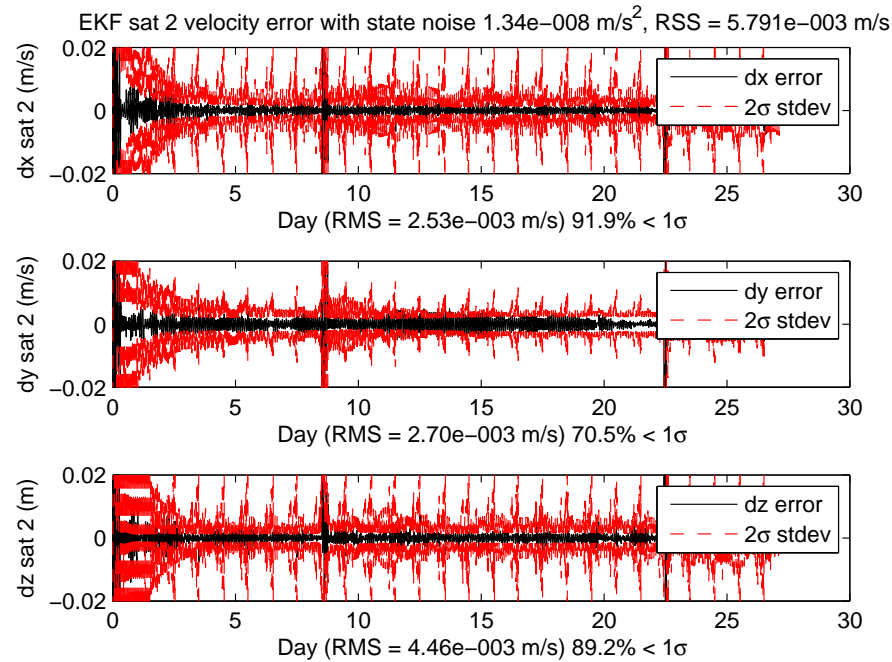


Figure 9.16: Woodstock velocity accuracy using the EKF.

in transit, in lunar orbits, or in halo orbits and send the observation data to Earth for processing. They could also broadcast navigation signals that would provide additional navigation accuracy during landings or surface explorations. The errors in orbit estimates for Snoopy and Woodstock would translate into errors in this tracking data, so some simulations were performed to see how useful the tracking data would be.

The first user spacecraft simulated was in a circular, low lunar orbit with an altitude of 100 km. Depending on the orientation of the orbit plane, Woodstock might not be visible very often from the point of view of this user spacecraft. Because of this, only Snoopy was used as a tracking station. Observations were generated using Snoopy's true orbit and the true orbit of the user spacecraft. If the user spacecraft was visible, the observations were produced every 60 seconds during the times that Snoopy was scheduled to track user spacecraft, for a 2.5-day fit span. The initial state of the user spacecraft was perturbed, and a Least-Squares Batch Processor was used to estimate the initial state of the user spacecraft. This was repeated

for runs starting on March 15, 18, 21, and 28 of 2012 using range or range-rate. The same simulations were performed with a lunar orbiter at 1000 km altitude for 3-day fit spans. This higher lunar orbiter was tracked by both Snoopy and Woodstock. The average 3D position and velocity errors over the four runs are shown in Table 9.2. It appears that in these simulations, Snoopy did very well tracking the user in the 100 km orbit, but not as well tracking the user in the 1000 km orbit, although the results are still not bad. Woodstock was more effective for tracking the 1000 km user, and would be effective tracking other spacecraft in low lunar orbit if the orbit geometry were such that Woodstock could see the user a fair amount of the time.

Table 9.2: ORBIT DETERMINATION ACCURACY USING SNOOPY AND WOODSTOCK AS TRACKING STATIONS

User altitude	Tracking s/c	obs. type	pos. error (m)	vel. error (m/s)
100 km	Snoopy	Range	8.76	0.012
100 km	Snoopy	Range rate	9.50	8.6×10^{-3}
1000 km	Snoopy	Range	84.1	0.032
1000 km	Snoopy	Range rate	25.6	9.9×10^{-3}
1000 km	Woodstock	Range	6.34	3.3×10^{-3}
1000 km	Woodstock	Range rate	10.0	4.7×10^{-3}

9.7 Conclusion

Although further research could reveal a more optimum low lunar orbit, or a descent from the LL_2 halo that results in a better value of δ , it was shown that this mission to LL_2 would provide needed communication and navigation support for future lunar missions as specified in ESAS. Snoopy and Woodstock would provide tracking support for Earth transit, orbit insertion and landing on the Moon. They could also be used for intervehicle and Moon-to-Earth communications. The constellation could evolve seamlessly by adding spacecraft when new capabilities are needed. The utilization of halo orbits would allow the constellation to be reconfigured with very little fuel in the event of the loss or addition of spacecraft. This flexibility would add considerably to the reliability and redundancy of the constellation.

In addition to satisfying the needs outlined in ESAS, the mission costs would be reduced

by using low-energy transfers and Liaison Navigation. Low-energy transfers such as BLT's would enable more mass to be placed in lunar halo orbits than conventional lunar transfers. This can all be done using proven chemical propulsion technology, and several spacecraft could be deployed using a single launch vehicle. Liaison Navigation would enable the constellation to navigate autonomously to reduce the workload for the DSN.

Chapter 10

Other Lunar Navigation Simulations

10.1 NASA's Lunar Communications

The mission in Chapter 9 was designed to provide communication and navigation services at the Moon, as well as far side gravity determination. The gravity determination requires that the orbit be very low. Several different NASA centers have published conference papers and reports on various lunar communication system concepts, which did not have the requirement for a low lunar orbit. Those papers, in addition to personal correspondence with employees at NASA Headquarters, NASA Ames Research Center, and NASA Goddard Space Flight Center revealed that lunar orbits with a higher altitude and better stability were more favorable.

To provide lunar communications services, Noreen et al. (2005) at JPL state that consideration was given to:

1. A large communication tower on Malapert Mountain near the lunar south pole.
2. Halo orbiters.
3. Lunar orbiters in “frozen orbits” that lingered over the south pole of the Moon.

The halo orbits were deemed ineffective because of the large communication link distance from the Moon to the halo orbits, and because of supposedly poor polar coverage. However, Chapter 9 and Grebow et al. (2006) show that polar coverage in halo orbits is actually quite good. Still, the large link distance is a valid disadvantage for halo orbits.

The Space Communications Architecture Working Group (SCAWG) also conducted a

trade study (Schier et al., 2005; SCAWG, 2006) to identify the ideal lunar communications orbits, and they chose the same orbit as Noreen et al. (2005). However, all of these studies operated with misconceptions about halo orbits. For example, the SCAWG report used “ideal, circular, perpendicular” halo orbits at the Moon for its trade study, but no halo orbits exist that match that description. On these “ideal, circular, perpendicular” halo orbits, it was found that five satellites were needed to provide continuous south pole coverage. Grebow et al. (2006) show clearly that only two halo orbiters are needed for continuous coverage, and three would provide fully redundant, continuous coverage. Stationkeeping costs for halo orbits were estimated to be much higher than values given by Gómez et al. (1998) and the results from Chapter 9. In addition, no studies were conducted to examine the cost and accuracy of navigation in the lunar vicinity—only lunar communications were considered.

After careful scrutiny, the only major disadvantage to using halo orbits for lunar communications is the large link distances. The frozen orbits at the Moon do have a shorter communication link to the lunar surface than do halo orbits. Frozen orbits also have no deterministic stationkeeping requirements (Ely and Lieb, 2006; Folta and Quinn, 2006; Russell and Lara, 2006). These frozen orbits are selected so that the eccentricity and argument of perilune have no secular perturbation, making it possible for the spacecraft to avoid impacting the lunar surface as well as maintaining apolune above the south pole.

Because of the advantages of lunar frozen orbits, it was decided to investigate whether three-body dynamics were strong enough to enable Liaison Navigation between frozen orbiters or between a frozen orbiter and a halo orbiter. In addition, a L_1 halo orbit-LEO orbit constellation might be of use to Earth-based autonomous navigation needs. To conduct all these simulations, plus other research by fellow students, upgrades to the orbit propagation and orbit determination software were needed. Section 10.2 describes these software changes, and Sections 10.3 to 10.5 describe the simulation results.

10.2 TurboProp

The orbit integration functions used in all the simulations mentioned in this dissertation were programmed as MEX functions. MEX functions are called by MATLAB, but they can be written in other programming languages. These MEX functions were written in C and compiled in MATLAB using the `mex` command. Because the functions were written in C, the orbit integration was much faster than a similar integration would be in MATLAB. Other researchers were starting to use these MEX orbit propagators and other MEX functions that interpolate the JPL ephemerides. It was decided that all of these functions should be combined into an integrated software package, which was called TurboProp (Hill, 2007). TurboProp was designed to be easily installed using a single MATLAB script. As other researchers began to use the software, their feedback was used to continually improve TurboProp.

At the time of this writing, the orbit propagators, or ODE solvers, in TurboProp include a fixed-step fourth-order Runge-Kutta solver and a variable-step seventh/eighth-order Runge-Kutta solver. There is also a propagator for stations or vehicles on the surface of a planet. The surface propagator is a MATLAB function that generates the coordinates of the station/vehicle in inertial space.

TurboProp contains files for the JPL planetary ephemerides DE403 (Standish et al., 1995) and DE405 (Standish, 1998), the lunar gravity models LP100K (Konopliv et al., 2001) and LP150Q (Roncoli, 2005), and the Earth gravity model GGM02C (Tapley et al., 2005). In the latest release, Earth orientation and a drag model have been added that will allow users to propagate orbits near Earth.

One important update to TurboProp is that the center of the integration, or the origin of the coordinate system, is no longer the solar system barycenter. Now, the user can select the Sun or any of the planets to be the origin of the coordinate system. For lunar halo orbits, this greatly increases the precision since Moon- or Earth-centered coordinates are much smaller in magnitude than coordinates based on the solar system barycenter. When generating quasi-halo

orbits in a multiple shooting differential corrector, it was possible to reduce the position and velocity tolerances by about three orders of magnitude due to the change from barycenter to planet-centered coordinates.

Version 3.0 of TurboProp was used for all of the Liaison Navigation simulations mentioned in this chapter, and any mathematical theory related to TurboProp can be found in Hill (2007).

10.3 Frozen Orbit Constellation

In December 2006, NASA’s Lunar Architecture Team announced that it would focus on establishing a base at the lunar south pole as a first priority, before conducting so-called “sortie” missions in other locations. This eliminates the need for global communication coverage, at least at first. Ely and Lieb (2006) show that three spacecraft in a lunar frozen orbit that lingers over the south pole can provide redundant communication coverage there. The latest analysis also included SRP, which led to an adjustment of the semimajor axes of the orbits to maintain constant phasing. The orbital elements are shown in Table 10.1.

Table 10.1: ORBITAL ELEMENTS FOR A THREE-SATELLITE LUNAR COMMUNICATIONS CONSTELLATION IN FROZEN ORBITS.

s/c no.	a (km)	e	i^{op} (deg)	Ω^{op} (deg)	ω^{op} (deg)	M^{op} (deg)
1	6541.4	0.6	56.2	0	90	0
2	6543.9758657	0.6	56.2	0	90	120
3	6537.9213419	0.6	56.2	0	90	240

Note: The superscript “op” means the frame is at the Moon with the z-axis parallel to the normal of the Earth’s apparent orbit around the Moon. Credit: (Ely and Lieb, 2006)

Although Liaison Navigation was shown to work well in the vicinity of the Lagrange points 1 and 2 (L_1 and L_2), it was not known if the gravitational asymmetry due to the Earth would enable autonomous orbit determination in lunar frozen orbits. The perturbation due to the Earth on a lunar orbiter is much stronger than the lunar perturbation on an Earth orbiter. These frozen orbits have a high altitude (about 10,000 km) above the Moon at apolune, so the Earth’s third-body perturbation would be significant.

To find whether Liaison Navigation could be used in these orbits, the orbital elements were converted to Moon-centered inertial coordinates and propagated using TurboProp to generate “truth” ephemerides. A variable time-step, Runge-Kutta, 7-8th order integrator was used. DE403 (Standish et al., 1995) is the best ephemeris for the Moon, so it was used instead of DE405. The LP100K gravity field was used instead of LP150Q, even though LP150Q is the most accurate lunar gravity field available (Roncoli, 2005), because covariance data were only available for LP100K (Konopliv et al., 2001). The gravity coefficients up to degree and order 20 were used.

Using the truth orbits, crosslink range measurements were generated every five minutes when the Moon did not block the line of sight. These crosslink range measurements were only generated for one pair of satellites at a time, in one-hour blocks. Then Gaussian noise with a standard deviation of 1 m was added to the measurements. An EKF was used to process the measurements. See Chapter 9 for details on the EKF and process noise algorithms. The gravity field used in the EKF was a 1σ clone computed using the LP100K covariance matrix. The EKF orbit propagator was forced to use erroneous reflectance values for the three spacecraft that would result in acceleration errors on the order of 1×10^{-9} m/s. Range biases were estimated for satellites 2 and 3. The orbits and EKF simulation extended over a 24-day span, but the orbit states did not converge in that time, as shown in Figure 10.1 for satellite 1. This means that the Earth’s gravitational perturbation was not sufficiently strong to enable Liaison Navigation.

Because these three spacecraft are in the same orbital plane, the out-of-plane component is not well resolved, as explained in Chapter 4. Low-energy transfers from a halo orbit could be used to place all three spacecraft in different orbital planes instead. Ω_2^{op} and Ω_3^{op} were set to 120° and 240° , respectively, so the three satellites would be in different orbital planes. The results were better after the first observations were processed, as shown for satellite 1 in Figure 10.2, but still the estimates did not converge properly over time.

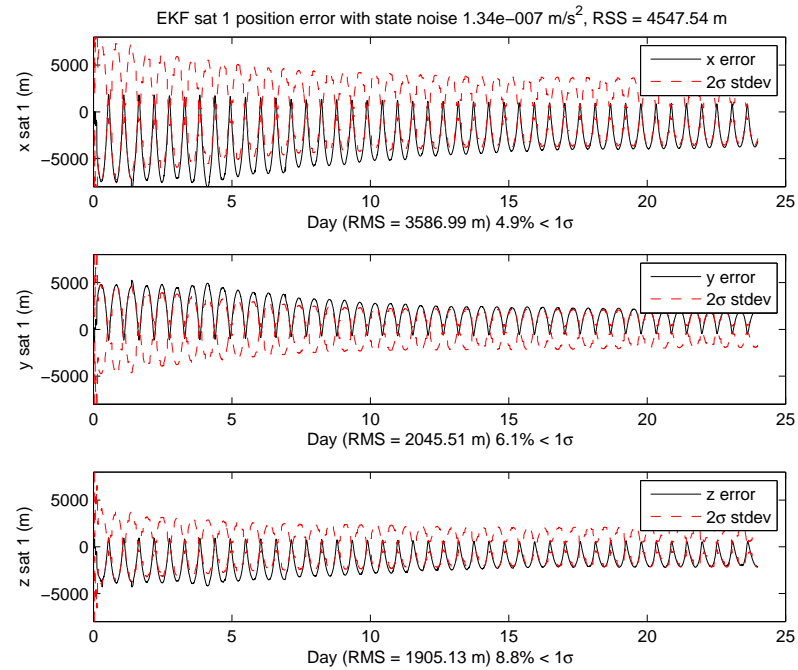


Figure 10.1: Satellite 1 position accuracy using the EKF. The three satellites are in coplanar frozen orbits.

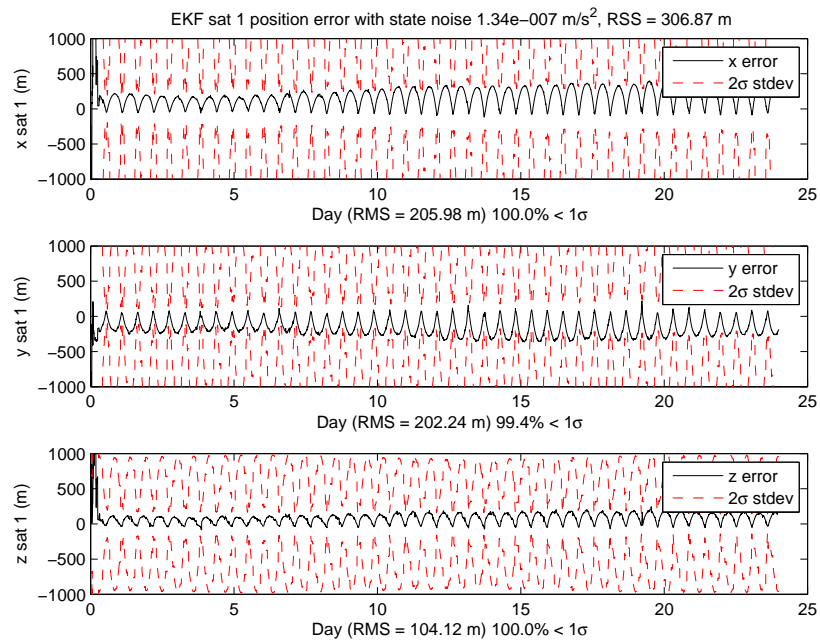


Figure 10.2: Satellite 1 position accuracy using the EKF. The three satellites are in frozen orbits in three different orbit planes.

10.4 Hybrid L_2 /Frozen Orbit Constellation

Since both L_2 halo orbits and frozen orbits have distinct advantages, a hybrid constellation consisting of a halo orbiter and a frozen orbiter could provide the benefits of both. An L_2 orbiter was placed in the same halo orbit as Snoopy in Chapter 9. A lunar orbiter was placed in a pole lingering frozen orbit, as explained in Section 10.3. The two spacecraft tracked each other and generated crosslink range measurements in a simulation similar to Section 10.3. The results for position estimation are shown in Figure 10.3 for the halo orbiter and Figure 10.4 for the lunar orbiter. The position error for the halo orbiter was 20 m RSS, and 5 m RSS for the frozen orbiter, computed after day 10. The accuracy in this simulation, even with the gravity and SRP modeling errors included, was better than the results in Chapter 9 from Snoopy and Woodstock. This is probably because of the new planet-centered integration in TurboProp that improves the effective numerical precision. Another reason for the decreased error is that the lunar orbiter does not perform maneuvers that have to be estimated by the EKF, since the frozen orbits are theoretically maneuver-free.

10.5 L_1 /LEO Constellation

A final simulation was performed to investigate the feasibility of using Liaison Navigation for application to near-Earth space. For this simulation, the Earth was the center of the coordinate system, and a spacecraft was placed in a circular low Earth orbit at 800-km altitude and 60° inclination. Another spacecraft was placed in an L_1 halo orbit with a vertical size similar to the Snoopy halo orbit used at L_2 . The JGM-3 gravity field (Tapley et al., 1996) was used for the truth orbits to degree and order 50. A $1\text{-}\sigma$ clone of the JGM-3 gravity field was provided by John Ries of the Center for Space Research at the University of Texas, and used in the EKF. Hill (2007) gives details on how to convert from Earth-centered ICRF coordinates (GCRF) to Earth-fixed coordinates (ITRF) for gravity field computations, using equations from Vallado and McClain (2001) and Vallado et al. (2006).

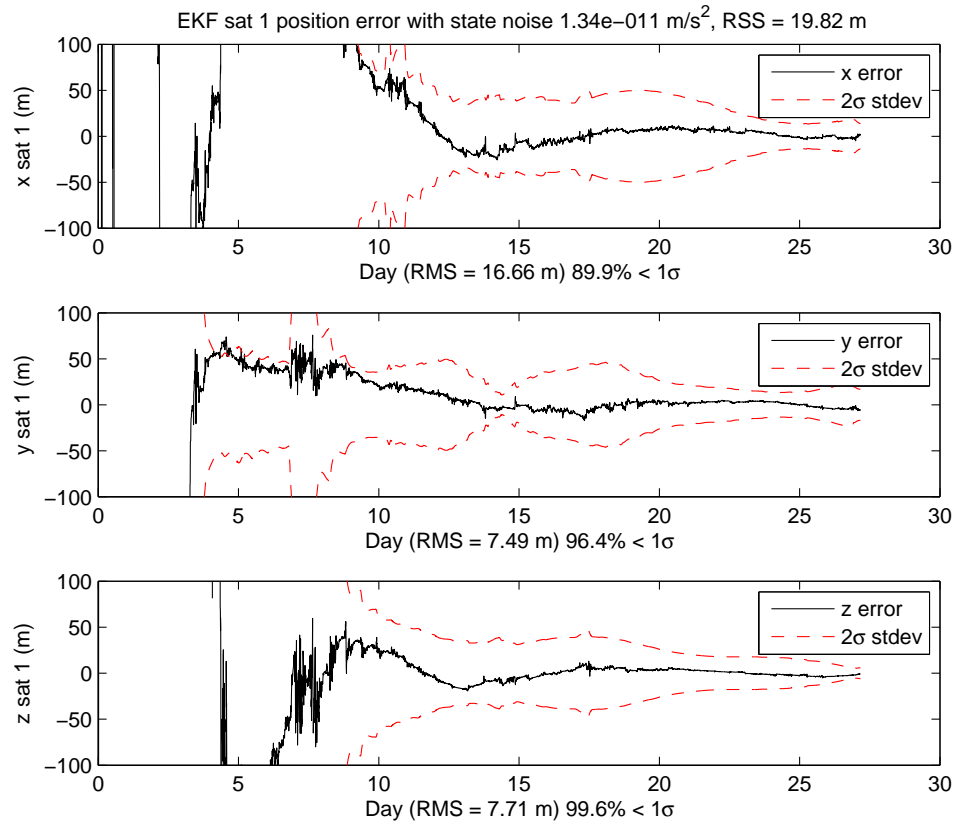


Figure 10.3: L_2 halo orbiter EKF position accuracy using crosslink range measurements to a lunar spacecraft in a frozen orbit.

Crosslink range measurements were generated every six minutes, with all other parameters set up similar to Section 10.3. The result for the L_1 halo orbiter position error is shown in Figure 10.5. The RSS position errors are about 130 m and 8 m for the halo orbiter and LEO orbiter, respectively. Even though these results are good, they aren't as precise as the L_2 -Frozen Orbit constellation described in Section 10.4. This is probably because from L_1 to Earth, the long link distance means that crosslinks are generally in the same direction. However, from L_2 to a frozen orbit, the crosslinks are more geometrically diverse as the halo orbiter goes around its orbit. The L_2 halo orbiter can track the frozen orbiter from many different directions over its two-week period.

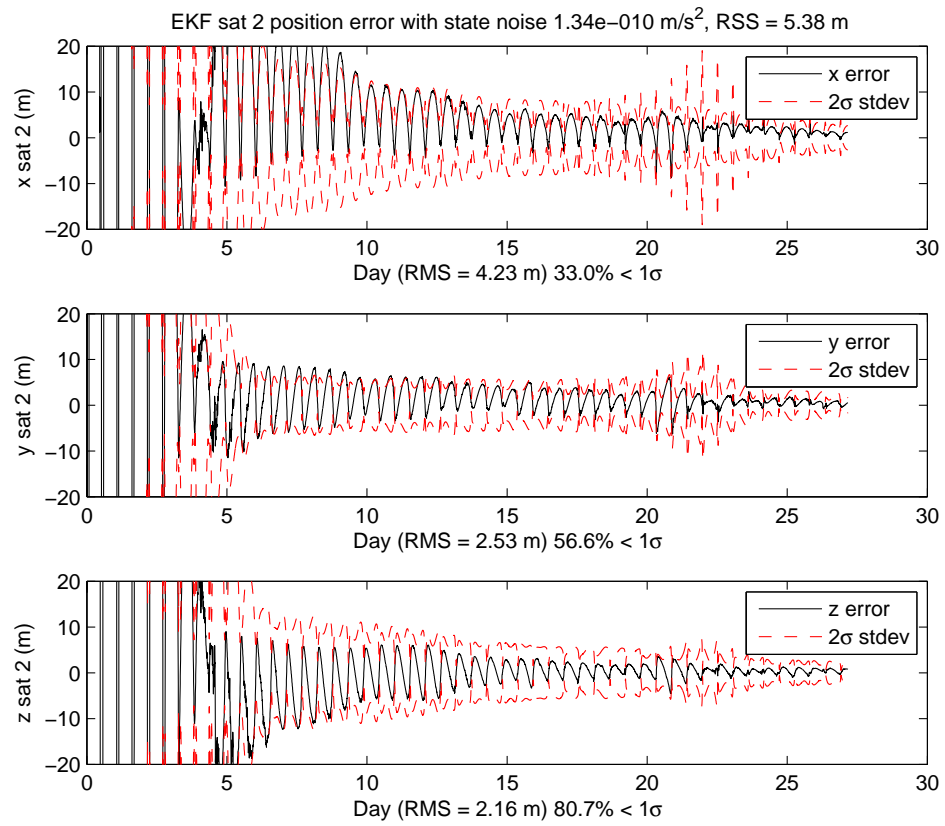


Figure 10.4: Lunar Pole-lingering frozen orbit EKF position accuracy using crosslink range measurements to a halo orbiter at L_2 .

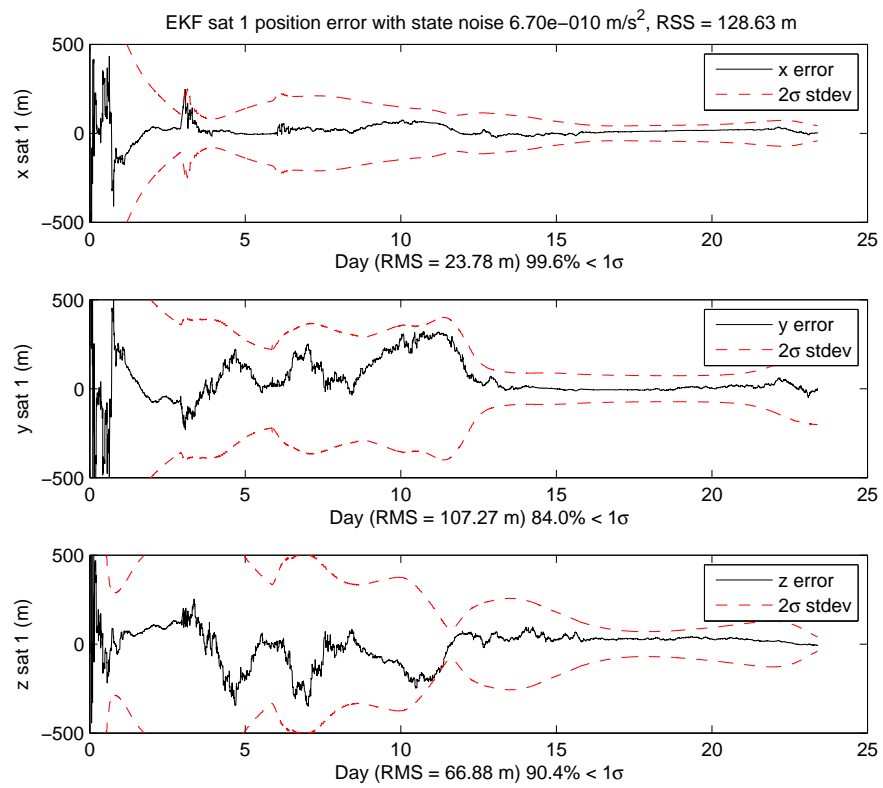


Figure 10.5: L_1 halo orbiter EKF position accuracy using crosslink range measurements to a spacecraft in LEO.

Chapter 11

Summary and Conclusions

11.1 Summary of Contributions

A new method of performing autonomous orbit determination in libration point orbits was developed that uses scalar satellite-to-satellite tracking (SST) measurements such as crosslink range or Doppler. This method has been named “Liaison Navigation.” Because of the unique dynamics and the asymmetry in the gravitational accelerations near the Lagrange points in the three-body problem, these relative tracking measurements can be used to estimate relative *and* absolute orbit states for all participating spacecraft simultaneously. This is a departure from the widely accepted notion that SST can not be used alone to truly observe the absolute states of all participating spacecraft. While that notion may be true in Earth orbits, or in the two-body problem, it has been shown in this dissertation that it is not true for unique orbits in the three-body problem.

A program of increasingly complex and realistic computer simulations was performed to validate that SST could be used alone to perform orbit determination in the three-body problem. The first simulations were performed in the Circular Restricted Three-Body Problem (CRTBP), and showed that spacecraft in halo orbits could track lunar orbiters, Earth orbiters, or other halo orbiters and use the crosslink range or Doppler measurements to estimate the position and velocity of both spacecraft. A batch processor was used to verify that the states were truly observable. It was shown that range biases could be estimated as well.

The next set of simulations added a fourth body to the model. In this case, the fourth body was the Sun, and its gravity and radiation pressure were included in the simulation. The results showed that Liaison Navigation still performed well, and that the reflectance parameters for each spacecraft could be successfully estimated. Other simulations were also performed using a full Solar System model that included the point mass effects from each of the planets. The planetary ephemerides were computed from the JPL ephemeris.

Next, additional realism was added to the simulations by including a spherical harmonic gravity model for the central body (usually the Moon) and using statistical clones of the gravity models to simulate errors. Also, the estimates from Liaison Navigation were used to compute stationkeeping maneuvers, which were executed with thrust errors. These maneuver execution errors were also successfully estimated using Liaison Navigation.

In conjunction with other researchers, a lunar mission was designed using Liaison Navigation and low-energy trajectories. The orbit determination was performed using an Extended Kalman Filter of the type that could be used in real-time onboard a spacecraft. Errors in Liaison Navigation estimates were on the order of 100 m for the halo orbiter and 10 m for the lunar orbiter, even with gravity and solar radiation modeling errors purposely included.

Finally, additional simulations were performed for several constellations in the Earth-Moon system to show that Liaison Navigation would be useful for NASA's lunar exploration or several other Earth-based applications.

11.2 Conclusions

The research presented here has shown that Liaison Navigation is feasible in a variety of modeling environments and with a high degree of realism. Using SST can be cost-effective because there is no requirement for special sensors or attitude determination accuracy. The communication antennas and hardware needed for Liaison Navigation would be used for telecommunication also.

This type of autonomous orbit determination would prove very useful for lunar libration

orbits, and could be used to provide navigation support for missions to the Moon in the near future. Liaison Navigation could also be used to support spacecraft in the libration orbits that are already commonly used at Sun-Earth L_1 and L_2 .

11.3 Future Work

The next logical step in researching Liaison Navigation would be to duplicate these results using software with an already established reputation. Considerable effort was expended in an attempt to simulate Liaison Navigation using the GPS Enhanced Onboard Navigation System (GEONS) from NASA's Goddard Spaceflight Center, but inadequacies in the lunar orbit determination capabilities of GEONS prevented that work from being completed.

The most convincing proof of Liaison Navigation's usefulness would be to obtain real SST data from a halo orbiter. This could be processed and compared to Earth-based navigation solutions. Since it is unlikely that any such data will become available in the near future, SST data between an Earth orbiter and a lunar orbiter could also be used as a validation. Since, in the coming years, there will be more spacecraft in these orbits than in libration point orbits, there is a higher probability that several could be equipped with the special clocks or hardware needed to obtain these types of measurements.

Bibliography

- Anderson, R. L., *Low Thrust Trajectory Design for Resonant Flybys and Captures Using Invariant Manifolds*, Ph.D. thesis, University of Colorado, Boulder, December 2005.
- Anderson, R. L., M. W. Lo, and G. H. Born, "Application of Local Lyapunov Exponents to Maneuver Design and Navigation in the Three-Body Problem," AAS 03-569, AAS/AIAA Astrodynamics Specialist Conference, Big Sky, Montana, Aug. 3-7, 2003.
- Beckman, M., "Orbit Determination Issues for Libration Point Orbits," Libration Point Orbits and Applications, Parador d'Aiguablava, Girona, Spain, Jun. 10-14, 2002.
- Bhaskaran, S., J. E. Riedel, and S. P. Synnott, "Demonstration of Autonomous Orbit Determination Around Small Bodies," AAS 95-387, AAS/AIAA Astrodynamics Specialist Conference, Halifax, Nova Scotia, Canada, Aug. 14-17, 1995.
- Bhaskaran, S., J. E. Riedel, S. P. Synnott, and T. C. Wang, "The Deep Space 1 Autonomous Navigation System: A Post-flight analysis," AIAA 2000-3935, AIAA/AAS Astrodynamics Specialist Conference, Denver, CO, Aug. 14-17, 2000.
- Brieß, K., W. Bärwald, E. Gill, H. Kayal, O. Montenbruck, S. Montenegro, W. Halle, W. Skrbek, H. Studemund, T. Terzibaschian, and H. Venus, "Technology Demonstration by the BIRD-mission," *Acta Astronautica*, Volume 56, 2005, pp. 57-63.
- Broucke, R. A., "Periodic Orbits in the Restricted Three-Body Problem with Earth-Moon Masses," NASA Technical Report 32-1168, 1968.
- Carpenter, J., D. Folta, M. Moreau, and D. Quinn, "Libration Point Navigation Concepts Supporting the Vision for Space Exploration," AIAA 2004-4747, AIAA/AAS Astrodynamics Specialist Conference, Providence, Rhode Island, August 16-19, 2004.
- Chory, M. A., D. Hoffman, and J. L. LeMay, "Satellite Autonomous Navigation - Status and History," IEEE Position, Location, and Navigation Symposium, Las Vegas, NV, 1986.
- Dunham, D. W. and R. W. Farquhar, "Libration-Point Missions 1978-2000," Libration Point Orbits and Applications, Parador d'Aiguablava, Girona, Spain, Jun. 10-14, 2002.
- Ely, T. A. and E. Lieb, "Constellations of Elliptical Inclined Lunar Orbits Providing Polar and Global Coverage," *Journal of the Astronautical Sciences*, Volume 54(1), 2006, pp. 53-67.
- ESAS, "NASA's Exploration Systems Architecture Study," NASA-TM-2005-214062, November 2005.
- Farquhar, R. W., "The Control and Use of Libration-Point Satellites," NASA Technical Report TR R-346, 1970.

- Farquhar, R. W. and A. A. Kamel, "Quasi-periodic Orbits About the Translunar Libration Point," *Celestial Mechanics*, Volume 7, 1973, pp. 458–473.
- Folta, D., "LUNAR Reconnaissance Observer ΔV Budget Estimate," NASA Goddard Space Flight Center, April 2, 2004.
- Folta, D. and A. Hawkins, "Results of NASA's First Autonomous Formation Flying Experiment: Earth Observing-1 (EO-1)," AIAA 2002-4743, AIAA/AAS Astrodynamics Specialist Conference Monterey, CA, Aug. 5-8, 2002.
- Folta, D. and D. Quinn, "Lunar Frozen Orbits," AIAA 2006-6749, AIAA/AAS Astrodynamics Specialist Conference and Exhibit, Keystone, CO, 21 - 24 August, 2006.
- Folta, D. and F. Vaughn, "A Survey of Earth-Moon Libration Orbits: Stationkeeping Strategies and Intra-Orbit Transfers," AIAA 2004-4741, AIAA/AAS Astrodynamics Specialist Conference, Providence, Rhode Island, August 16-19, 2004.
- Gill, E., O. Montenbruck, and K. Brieß, "GPS-based Autonomous Navigation for the BIRD Satellite," International Symposium SpaceFlight Dynamics, Biarritz, France, 2000.
- Gómez, G., K. Howell, J. Masdemont, and C. Simó, "Station-keeping Strategies for Translunar Libration Point Orbits," AAS 98-168, AAS/AIAA Space Flight Mechanics Meeting, Monterey, CA, Feb. 9-11, 1998.
- Gómez, G., C. Simó, J. Llibre, and R. Martínez, *Dynamics and Mission Design near Libration Points, Volume II: Fundamentals: The Case of Triangular Libration Points*, Monograph Series in Mathematics, World Scientific, Singapore, 2001.
- Grebow, D., M. Ozimek, K. Howell, and D. Folta, "Multi-Body Orbit Architectures for Lunar South Pole Coverage," AAS 06-179, AAS/AIAA Space Flight Mechanics Conference, Tampa, Florida, January 22-26, 2006.
- Han, D., B. Williams, G. Carlisle, K. Williams, G. Bollman, and D. Sweetman, "Genesis: Planning, Control, Analysis, and Recovery Reference Document," Volume 19: Navigation Plan, GN-61000-200-19, Jet Propulsion Laboratory, 2001.
- Hicks, K. D. and W. E. Wiesel, "Autonomous Orbit Determination System for Earth Satellites," *Journal of Guidance, Control, and Dynamics*, Volume 15(3), 1992, pp. 562–566.
- Hill, K., "TurboProp Version 3.0," Colorado Center For Astrodynamics Research, http://ccar.colorado.edu/geryon/papers/TurboProp3.0_Manual.pdf, February 12, 2007.
- Hill, K. and G. Born, "Autonomous Interplanetary Orbit Determination Using Satellite-to-Satellite Tracking," *Journal of Guidance, Control, and Dynamics*, Volume 30(3), 2007.
- Hill, K., G. H. Born, and M. W. Lo, "Linked, Autonomous, Interplanetary Satellite Orbit Navigation (LiAISON) in Lunar Halo Orbits," AAS 05-400, AAS/AIAA Astrodynamics Specialist Conference, Lake Tahoe, CA, Aug. 7-11, 2005a.
- Hill, K., M. W. Lo, and G. H. Born, "Linked, Autonomous, Interplanetary Satellite Orbit Navigation (LiAISON)," AAS 05-399, AAS/AIAA Astrodynamics Specialist Conference, Lake Tahoe, CA, Aug. 7-11, 2005b.
- Hill, K., M. W. Lo, and G. H. Born, "Liaison Navigation in the Sun-Earth-Moon Four-body Problem," AAS 06-221, AAS/AIAA Space Flight Mechanics Conference, Tampa, Florida, January 22-26, 2006a.
- Hill, K., J. Parker, G. H. Born, and N. Demandante, "A Lunar L_2 Navigation, Communication, and Gravity Mission," AIAA 2006-6662, AIAA/AAS Astrodynamics Specialist Conference, Keystone, CO, Aug. 21-24, 2006b.

- Howell, K., "Three-Dimensional, Periodic, 'Halo' Orbits," *Celestial Mechanics*, Volume 32(53), 1984.
- Howell, K., B. Barden, and M. Lo, "Application of Dynamical Systems Theory to Trajectory Design for a Libration Point Mission," *The Journal of the Astronautical Sciences*, Volume 45(2), 1997, pp. 161–178.
- Howell, K. and H. Pernicka, "Numerical Determination of Lissajous Trajectories in the Restricted Three-body Problem," *Celestial Mechanics*, Volume 41, 1988, pp. 107–124.
- Jayles, C. and M. Costes, "Ten Centimeter Orbits in Real-time On-board of a Satellite: DORIS-DIODE Current Status," *Acta Astronautica*, Volume 54, 2004, pp. 315–323.
- Konopliv, A., S. W. Asmar, E. Carranza, W. L. Sjogren, and D. Yuan, "Recent Gravity Models as a Result of the Lunar Prospector Mission," *Icarus*, Volume 150, 2001, pp. 1–18.
- Kubitschek, D. G., "Impactor Spacecraft Targeting for the Deep Impact Mission to Comet Tempel 1," AAS 03-615, AAS/AIAA Astrodynamics Specialist Conference, Big Sky, MT, Aug. 3-7, 2003.
- Liu, Y. and L. Liu, "Orbit Determination Using Satellite-to-Satellite Tracking Data," *Chinese Journal of Astronomy and Astrophysics*, Volume 1(3), 2001, pp. 281–286.
- Long, A. C., D. Leung, D. Folta, and C. Gramling, "Autonomous Navigation of High-Earth Satellites Using Celestial Objects and Doppler Measurements," AIAA 2000-3937, AIAA/AAS Astrodynamics Specialist Conference, Denver, CO, Aug. 14-17, 2000.
- Ma, C., E. Arias, T. Eubanks, A. Fey, A. Gontier, C. Jacobs, O. Sovers, B. Archinal, and P. Charlot, "The International Celestial Reference Frame as Realized by Very Long Baseline Interferometry," *Astronomical Journal*, Volume 116, 1998, pp. 516–546.
- Markley, F. L., "Autonomous Navigation Using Landmark and Intersatellite Data," AIAA 1984-1987, AIAA/AAS Astrodynamics Conference, Seattle, WA, Aug. 20-22, 1984.
- Menn, M., "Autonomous Navigation for GPS via Crosslink Ranging," IEEE Position Location, and Navigation Symposium, Las Vegas, NV, 1986.
- Merriam-Webster, *The Merriam-Webster Dictionary*, Merriam-Webster Inc., Springfield, MA, 1994.
- Moreau, M. C., P. Axelrad, J. L. Garrison, and A. Long, "GPS Receiver Architecture and Expected Performance for Autonomous Navigation in High Earth Orbits," *Navigation*, Volume 47(3), 2000, pp. 191–204.
- Murray, C. D. and S. F. Dermott, *Solar System Dynamics*, Cambridge University Press, Cambridge, UK, 1999.
- Newhall, X. X. and J. G. Williams, "Estimation of the Lunar Physical Librations," *Celestial Mechanics and Dynamical Astronomy*, Volume 66, 1997, pp. 21–30.
- Noreen, G., R. Cesarone, L. Deutsch, C. Edwards, J. Soloff, T. Ely, B. Cook, D. Morabito, H. Hemmati, S. Piazzolla, R. Hastrup, D. Abraham, M. Sue, and F. Manshadi, "Integrated Network Architecture for Sustained Human and Robotic Exploration," IEEEAC paper 1378, Aerospace, 2005 IEEE Conference, March 5-12, 2005.
- Parker, J., "Families of Low-Energy Lunar Halo Transfers," AAS 06-132, AAS/AIAA Space Flight Mechanics Conference, Tampa, Florida, January 22-26, 2006.

- Parker, J. and M. Lo, "Shoot the Moon 3D," AAS 05-383, AAS/AIAA Astrodynamics Specialist Conference, Lake Tahoe, California, August 7-11, 2005.
- Parker, J. S., *Low-Energy Ballistic Lunar Transfers*, Ph.D. thesis, University of Colorado, Boulder, May 2007.
- Psiaki, M. L., "Autonomous LEO Orbit Determination from Magnetometer and Sun Sensor Data," AIAA 1998-4308, AIAA Guidance, Navigation, and Control Conference, Boston, MA, Aug. 10-12, 1998.
- Psiaki, M. L., "Autonomous Low-Earth-Orbit Determination from Magnetometer and Sun Sensor Data," *Journal of Guidance, Control, and Dynamics*, Volume 22(2), 1999a, pp. 296–302.
- Psiaki, M. L., "Autonomous Orbit Determination for Two Spacecraft from Relative Position Measurements," *Journal of Guidance, Control, and Dynamics*, Volume 22(2), 1999b, pp. 305–312.
- Psiaki, M. L., "Tests of Magnetometer/Sun-Sensor Orbit Determination Using Flight Data," *Journal of Guidance, Control, and Dynamics*, Volume 25(3), 2002, pp. 582–590.
- Richardson, D. L., "Analytic Construction of Periodic Orbits About the Collinear Points," *Celestial Mechanics*, Volume 22, 1980, pp. 241–253.
- Richardson, D. L. and N. D. Cary, "A Uniformly Valid Solution for Motion About the Interior Libration Point of the Perturbed Elliptic-restricted Problem," AAS 75-021, AAS/AIAA Astrodynamics Specialist Conference, Nassau, Bahamas, July 28-30, 1975.
- Roncoli, R. B., "Lunar Constants and Models Document," JPL D-32296, September 23, 2005.
- Russell, R. P. and M. Lara, "Repeat Ground Track Lunar Orbits in the Full-Potential Plus Third-Body Problem," AIAA 2006-6750, AIAA/AAS Astrodynamics Specialist Conference and Exhibit, Keystone, CO, 21 - 24 August, 2006.
- SCAWG, "NASA Space Communication and Navigation Architecture Recommendations for 2005-2030," May 15, 2006.
- Scheeres, D. J., "Characterizing the Orbit Uncertainty Dynamics along an Unstable Orbit," AAS 01-302, AAS/AIAA Astrodynamics Specialist Conference, Quebec City, Quebec, July 30-August 2, 2001.
- Scheeres, D. J., D. Han, and Y. Hou, "Influence of Unstable Manifolds on Orbit Uncertainty," *Journal of Guidance, Control, and Dynamics*, Volume 24(3), 2001, pp. 573–585.
- Schier, J. S., J. J. Rush, W. D. Williams, and P. Vrotsos, "Space Communication Architecture Supporting Exploration and Science: Plans and Studies for 2010-2030," AIAA 2005-2517, AIAA 1st Space Exploration Conference, Orlando, FL, Jan. 30-Feb. 1, 2005.
- Sheikh, S. I., D. J. Pines, P. S. Ray, K. S. Wood, M. N. Lovellette, , and M. T. Wolff, "Spacecraft Navigation Using X-Ray Pulsars," *Journal of Guidance, Control, and Dynamics*, Volume 29(1), 2006, pp. 49–63.
- Standish, E. M., "JPL Planetary and Lunar Ephemerides, DE405/LE405," Jet Propulsion Laboratory Interoffice Memorandum IOM 312F-98-048, Aug. 26, 1998.
- Standish, E. M., X. X. Newhall, J. G. Williams, and W. M. Folkner, "JPL Planetary and Lunar Ephemerides, DE403/LE403," Jet Propulsion Laboratory Interoffice Memorandum IOM 314.10-127, May 22, 1995.

- Tapley, B., J. Ries, S. Bettadpur, D. Chambers, M. Cheng, F. Condi, B. Gunter, Z. Kang, P. Nagel, R. Pastor, T. Pekker, S. Poole, and F. Wang, "GGM02 - An Improved Earth Gravity Field Model from GRACE," *Journal of Geodesy*, Volume 79(8), 2005, pp. 467–478.
- Tapley, B., M. Watkins, J. Ries, G. Davis, R. Eanes, S. Poole, H. Rim, B. Schutz, C. Shum, R. Nerem, F. Lerch, J. Marshall, S. Klosko, N. Pavlis, and R. Williamson, "The Joint Gravity Model 3," *Journal of Geophysical Research*, Volume 101(B12), 1996, pp. 28,029–28,050.
- Tapley, B. D., B. E. Schutz, and G. H. Born, *Statistical Orbit Determination*, Elsevier Academic Press, Burlington, MA, 2004.
- Unwin, M. and M. Sweeting, "A Practical Demonstration of Low Cost Autonomous Orbit Determination Using GPS," ION GPS-95, 8th International Technical Meeting of the Satellite Division of the Institute of Navigation, Palm Springs, CA, 1995.
- Vallado, D. and W. McClain, *Fundamentals of Astrodynamics and Applications*, 2nd Edition, Microcosm Press, El Segundo, CA, 2001.
- Vallado, D. A., J. H. Seago, and P. K. Seidelmann, "Implementation Issues Surrounding the New IAU Reference Systems for Astrodynamics," AAS 06-134, AAS/AIAA Space Flight Mechanics Conference, Tampa, Florida, January 22-26, 2006.
- Vasile, M., "Deep Space Autonomous Orbit Determination Using CCD," AIAA 2002-4818, AIAA/AAS Astrodynamics Specialist Conference Monterey, CA, Aug. 5-8, 2002.
- Wawrzyniak, G., D. Han, G. Lewis, E. Graat, D. Baird, and D. Craig, "Genesis Orbit Determination for Earth Return and Atmospheric Entry," AAS 05-117, AAS/AIAA Space Flight Mechanics Conference, Copper Mountain, CO, Jan. 23-27, 2005.
- Williams, K., R. Wilson, M. Lo, K. Howell, and B. Barden, "Genesis Halo Orbit Station Keeping Design," International Symposium: Spaceflight Dynamics Biarritz, France, 26 June, 2000.
- Wilson, R., "Derivation of Differential Correctors Used in GENESIS Mission Design," JPL IOM 312.I-03-002.
- Yim, J. R., J. L. Crassidis, and J. L. Junkins, "Autonomous Orbit Navigation of Interplanetary Spacecraft," AIAA 2000-3936, AIAA/AAS Astrodynamics Specialist Conference, Denver, CO, Aug. 14-17, 2000.
- Yim, J. R., J. L. Crassidis, and J. L. Junkins, "Autonomous Orbit Navigation of Two Spacecraft System Using Relative Line of Sight Measurements," AAS 04-257, AAS/AIAA Astrodynamics Specialist Conference, Maui, HI, Feb. 8-12, 2004.

Appendix A

Converting from the CRTBP to ICRF

In the JPL ephemeris model, the positions and velocities of the sun and planets with respect to the solar system barycenter are in the International Celestial Reference Frame (ICRF) and are obtained from the JPL ephemeris (Standish et al., 1995; Standish, 1998). Three-body systems in the JPL ephemeris model are no longer circular and coplanar and the other planets now add gravitational perturbations. Because of these perturbations, there are no longer any truly periodic solutions. This means that perfectly periodic halo orbits found in the Circular Restricted Three-Body Problem (CRTBP) cannot occur in the ephemeris model. Instead, trajectories must be computed that are fairly close to periodic, at least for the time interval desired. These quasi-periodic orbits can be called quasi-halo orbits. A numerical method used to find a continuous quasi-halo trajectory is the multiple shooting differential corrector adapted from the work of Howell and Pernicka (1988) and Wilson. This technique can also be used to find numerical examples of the Lissajous orbits described in Chapter 3.

To initialize the multiple shooting differential corrector, an initial trajectory is required. For these “initial guess” trajectories, a halo orbit from the CRTBP can be differentially corrected numerically (Howell, 1984), or an analytical halo orbit can be obtained from Richardson (1980). These halo orbits from the CRTBP must be rotated and scaled to fit into the proper locations in the solar system model. Patch points are selected along the CRTBP halo with a certain time interval between them, and these patch points were converted to solar system coordinates, or the ICRF, in the following manner.

Let \mathbf{X}_{bary} be the state vector of a patch point in the rotating, nondimensional, barycentric coordinates of the CRTBP as described in Chapter 3.

$$\mathbf{X}_{bary} = \begin{bmatrix} x_{bary} & y_{bary} & z_{bary} & \dot{x}_{bary} & \dot{y}_{bary} & \dot{z}_{bary} \end{bmatrix}^T, \quad (\text{A.1})$$

where T denotes a matrix transpose. \mathbf{X}_{bary} is converted to $\mathbf{X}_{bary,inert}$, an inertial state centered on the barycenter, assuming that the two primary bodies are on the x axis. This is done by adding in the rotational velocity, as shown in Appendix C of Anderson (2005).

$$\mathbf{X}_{bary,inert} = \mathbf{X}_{bary} + \begin{bmatrix} 0 & 0 & 0 & -y_{bary} & x_{bary} & 0 \end{bmatrix}^T \quad (\text{A.2})$$

Next, the units of $\mathbf{X}_{bary,inert}$ are dimensionalized with the multiplication

$$\mathbf{X}_{dim,inert} = \begin{bmatrix} LU & & & & & \\ & LU & & & & \\ & & LU & & & \\ & & & \frac{LU}{TU} & & \\ & & & & \frac{LU}{TU} & \\ & & & & & \frac{LU}{TU} \end{bmatrix} \mathbf{X}_{bary,inert}. \quad (\text{A.3})$$

LU is the conversion from nondimensional length units to dimensional length units and is equal to the magnitude of the position portion of $\mathbf{X}_{P1,P2}$, where $\mathbf{X}_{P1,P2}$ is the state vector of the secondary with respect to the primary body (Parker, 2007). If the desired length units were kilometers, LU would be $\approx 384,400$ km in the Earth-Moon system, with the exact value depending on the instantaneous distance between the Earth and Moon. TU is the conversion from nondimensional time units to dimensional time units. For the Earth-Moon system, TU would be $P/(2\pi)$ where P is the sidereal period of the Moon's orbit around the Earth.

Next, a rotation must be found to rotate the position and velocity of $\mathbf{X}_{dim,inert}$ so that it aligns with the motions of the two primary bodies in the ICRF coordinate system. The different components of the vector $\mathbf{X}_{P1,P2}$ are denoted

$$\mathbf{X}_{P1,P2} = \begin{bmatrix} x_{P1,P2} & y_{P1,P2} & z_{P1,P2} & \dot{x}_{P1,P2} & \dot{y}_{P1,P2} & \dot{z}_{P1,P2} \end{bmatrix}^T. \quad (\text{A.4})$$

The angles β , ϕ , and θ are used in the rotation.

$$\begin{aligned}\beta &= \tan^{-1} \left(\frac{\dot{z}_{P1,P2}}{\sqrt{\dot{x}_{P1,P2}^2 + \dot{y}_{P1,P2}^2}} \right) \\ \phi &= \tan^{-1} \left(\frac{z_{P1,P2}}{\sqrt{x_{P1,P2}^2 + y_{P1,P2}^2}} \right) \\ \theta &= \tan^{-1} \left(\frac{y_{P1,P2}}{x_{P1,P2}} \right)\end{aligned}\tag{A.5}$$

β is the angle describing the out-of-plane velocity of the secondary with respect to the primary, where the plane is the ecliptic in ICRF coordinates. ϕ is the angle describing the out-of-plane position of the secondary and θ describes the position of the secondary within the plane.

Next, both the position and velocity of $\mathbf{X}_{dim,inert}$ are rotated by the angle $-\beta$ about the z axis. Then rotate by the angle ϕ about the y axis, and finally rotate by the angle $-\theta$ about the z axis. This combined rotation can be called γ .

$$\gamma = ROT3(-\theta)ROT2(\phi)ROT3(-\beta)\tag{A.6}$$

The rotation matrices $ROT1$, $ROT2$, and $ROT3$ rotate a 3-vector about the x, y, and z axis, respectively.

$$ROT1(\theta) = \begin{bmatrix} 1 & 0 & 0 \\ 0 & \cos(\theta) & \sin(\theta) \\ 0 & -\sin(\theta) & \cos(\theta) \end{bmatrix}\tag{A.7}$$

$$ROT2(\theta) = \begin{bmatrix} \cos(\theta) & 0 & -\sin(\theta) \\ 0 & 1 & 0 \\ \sin(\theta) & 0 & \cos(\theta) \end{bmatrix}\tag{A.8}$$

$$ROT3(\theta) = \begin{bmatrix} \cos(\theta) & \sin(\theta) & 0 \\ -\sin(\theta) & \cos(\theta) & 0 \\ 0 & 0 & 1 \end{bmatrix}\tag{A.9}$$

Combining the three rotations into one matrix gives

$$\gamma = \begin{bmatrix} \cos \theta \cos \phi & -\sin \theta \cos \beta - \cos \theta \sin \phi \sin \beta & \sin \theta \sin \beta - \cos \theta \sin \phi \cos \beta \\ \sin \theta \cos \phi & \cos \theta \cos \beta - \sin \theta \sin \phi \sin \beta & -\cos \theta \sin \beta - \sin \theta \sin \phi \cos \beta \\ \sin \phi & \cos \phi \sin \beta & \cos \phi \cos \beta \end{bmatrix}. \quad (\text{A.10})$$

The rotation of the state vector in matrix form is

$$\mathbf{X}_{ICRF} = \begin{bmatrix} \gamma & [\emptyset]_{3 \times 3} \\ [\emptyset]_{3 \times 3} & \gamma \end{bmatrix} \mathbf{X}_{dim, inert}, \quad (\text{A.11})$$

where $[\emptyset]_{3 \times 3}$ is a 3×3 matrix of zeros. \mathbf{X}_{ICRF} is the state vector of the patch point in the ICRF, centered on the three-body system barycenter. To convert the coordinates so that they are centered on the primary or secondary body instead, add the position of the barycenter with respect to the body:

$$\mathbf{X}_{ICRF, primary} = \mathbf{X}_{ICRF} - (-\mu)\mathbf{X}_{P1, P2} \quad (\text{A.12})$$

or

$$\mathbf{X}_{ICRF, secondary} = \mathbf{X}_{ICRF} - (1 - \mu)\mathbf{X}_{P1, P2}. \quad (\text{A.13})$$

$\mathbf{X}_{ICRF, primary}$ is the state vector of the patch point, centered on the primary body in ICRF coordinates. $\mathbf{X}_{ICRF, secondary}$ is centered on the secondary body. μ is the three-body mass ratio described in Chapter 3.

Typically, each patch point near L_1 or L_2 is converted from \mathbf{X}_{bary} to $\mathbf{X}_{ICRF, secondary}$, and the patch points are differentially corrected in the multiple shooting differential corrector using the secondary body as the center of integration.

To convert back from dimensional ICRF coordinates to the CRTBP nondimensional coordinates, these steps must be followed carefully in reverse order.